NUMERICAL STUDY OF ANISOTROPY AND DUCTILITY ENHANCEMENT IN SHEET METALS

NUMERICAL STUDY OF ANISOTROPY AND DUCTILITY ENHANCEMENT IN SHEET METALS

By MOHAMMADMEHDI SHAHZAMANIAN SICHANI, M.Sc.

A Thesis Submitted to the School of Graduate Studies in Partial Fulfillment of the Requirements for the Degree

Doctor of Philosophy

McMaster University DOCTOR OF PHILOSOPHY (2020)

Hamilton, Ontario, Canada

TITLE: Numerical Study of Anisotropy and Ductility Enhancement in Sheet Metals

AUTHOR: Mohammadmehdi Shahzamanian Sichani

SUPERVISOR: Professor\ Peidong Wu

Number of Pages: xxii, 175

Lay abstract

In this thesis, the finite element method (FEM) is used in analyzing the elastic–plastic behavior of sheet metals and investigating ways for enhancing their ductility. The Gurson–Tvergaard–Needleman (GTN) model is used to simulate the plastic behavior of metals on the basis of the effects of void growth and microvoids coalescence, which leads to ductile fracture. The GTN model is analyzed, implemented in finite element (FE) software ABAQUS, and extended to be suitable for anisotropic metals on the basis of Hill's quadratic anisotropic yield theory. The model application for enhancing the ductility of sheet metals under bending is investigated. Two methods, namely, superimposing hydrostatic pressure and cladding sheet metals with a soft material, are studied.

Abstract

GTN is analyzed and extended to be suitable for anisotropic matrix materials on the basis of Hill's quadratic anisotropic yield theory. An effective coefficient is defined in the extension, and it replaces Hill's constants to provide the elastic–plastic behavior of metals. In this model, three dimensional (3D) and plane stress elements are considered, containing ellipsoidal and spherical microvoids in matrix materials. The effect of each case is studied and compared with the stress–strain curve of a typical Al alloy.

Superimposed hydrostatic pressure delays the growth and coalescence of microvoids. Thus, bendability is significantly enhanced by superimposing hydrostatic pressure. The effect of hydrostatic pressure on tensile test simulation is determined and compared with that obtained under bending. This test is simulated under the plane strain state. Sheet metals have higher deformation under bending than under tension. The sensitivity of ductile fracture parameters in the GTN model to bendability is analyzed and used as the basis for exploring the bending response of sheet metals given by this model.

Cladding sheet metals slows down the development of stress triaxiality, which has a significant effect on the fracture of sheet metals. Consequently, the growth and coalescence of microvoids are delayed, and this condition leads to high bendability and increases fracture strain. A transition zone in the location of failure initiation is observed. This transition zone changes with increasing cladding thickness ratio (Γ). Fracture initiation changes from the core material close to the clad–core interface to the clad material on the outer surface of the specimen at increased Γ. The effect of mandrel span length as well as

stress–strain curves for clad materials on bendability is investigated and used as the basis for understanding changes in transition zones.

Dedication

I simply dedicate this Ph.D. dissertation to my beloved parents.

Acknowledgments

First and foremost, I would like to express my deepest gratitude and appreciation to my advisor, Dr. Peidong Wu. He never deprived me of his help and support. I would not have been able to complete this project without his support. Indeed, I am highly fortunate and grateful to have worked with him at this stage of my education.

Special appreciation is extended to Dr. David Lloyd from Aluminum Materials Consultants for his support and valuable contributions to this research.

Lastly, I would like to take this opportunity to express my gratitude to my parents for their endless supports, encouragement, and motivation.

Table of Contents

Lay abstract iii

Abstract iv

Acknowledgments vii

Table of Contents viii

LIST OF FIGURES xii

LIST OF TABLES xvii

Nomenclature xviii

ABBREVIATIONS xxii

CHAPTER 1 Introduction 1

1.1. Material modeling 1

1.2. Bending test 4

1.3. Ductility enhancement in sheet metals 6

1.4. Finite element method 9

1.5. Problem formulation and research scope 11

1.5.1. Anisotropic Gurson–Tvergaard–Needleman plasticity and damage model for finite element analysis of elastic–plastic problems 11

1.5.2. Study of the influence of superimposed hydrostatic pressure on the bendability of sheet metals 12

1.5.3. Enhanced bendability in sheet metals produced by cladding a ductile layer .. 12

1.6. Contribution of research 13

1.7. Organization of research and thesis document 13

1.8. A note to the reader 14

Chapter 2 Literature Review 15

2.1. Introduction 15

2.2. Gurson-Needleman-Tvergaard model 15

2.3. Effect of superimposed hydrostatic pressure 20

2.4. Effect of cladding on the ductility of metals 25

2.5. Summary 29

CHAPTER 3 31

Anisotropic Gurson-Tvergaard-Needleman plasticity and damage model for finite element analysis of elastic–plastic problems 31

ABSTRACT 32

3.1. Introduction and a brief review of literature 33

3.2. Stress and strain measures 35

3.3. Hill's quadratic anisotropic yield criterion 36

3.4. Elastoplastic constitutive equations 39

3.5. Integration algorithm for elastoplastic constitutive relations 40

3.5.1. 3-D case 41

3.5.2. Plane stress case 46

3.6. Stress updates 49

3.7. Linearization of moduli 50

3.7.1. Jacobian matrix in 3-D 51

3.7.2. Jacobian matrix in plane stress case 53
3.8. GTN yield criterion 54
3.8.1. Prolate ellipsoidal voids 56
3.9. Flow chart of algorithm 58
3.10. Numerical results and discussion 60
3.10.1. One-element test 60
3.10.2. Brief discussion of using specific GTN parameters in modeling 65
3.10.3. Tensile test 66
3.11. Conclusions 76
REFERENCES 82
CHAPTER 4 89
Study of influence of superimposed hydrostatic pressure on bendability of sheet metals 89
ABSTRACT 90
4.1. Introduction 90
4.2. Constitutive model 93
4.3. Problem formulation and method of solution 96
4.4. Results and discussion 97
4.4.1. Superimposed hydrostatic pressure effect in bending test 102
4.4.2. Fracture strain comparison in tensile and bending tests 109
4.4.3. Stress controlled void nucleation 114
4.4.4. GTN ductile fracture parametric study in bending test 116
4.5. Conclusion 120

REFRENCES 120
CHAPTER 5 126
Enhanced bendability in sheet metal produced by cladding a ductile layer 126
M.M. Shahzamanian, D.J. Lloyd and P.D. Wu "Enhanced bendability in sheet metal produced by cladding a ductile layer" Journal of Materials Today Communications, 23 (2020) 100952 126
ABSTRACT 127
5.1. Introduction 128
5.2. Constitutive model 131
5.3. Problem formulation and method of solution 133
5.4. Results 134
5.4.1. Effect of span length of mandrel 139
5.4.2. Effect of cladding thickness ratio ($\boldsymbol{\Gamma}$) 142
5.4.3. Effect of work hardening in clad material 151
5.5. Discussion 155
5.6. Conclusion 157
REFERENCES 158
CHAPTER 6 163
Conclusions and Recommendations for Future Work 163
6.1. Conclusions 163
6.2. Recommendations for future work 165
7. REFERENCES 167

LIST OF FIGURES

Chapter 1

Figure 1. 1. Four different modes of fracture [1] 2

Figure 1. 2. Schematic of the nucleation, growth, and coalescence of voids [2] 3

Figure 1. 3. Schematic of a three-point bending test [26] 6

Figure 1. 4. Schematic of the high-pressure testing apparatus in [42] 7

Figure 1. 5. Tensile specimens: (a) parent metal, (b) clad layer, and (c) tensile specimen of a clad material [44] 8

Figure 1. 6. FE mesh for gear tooth [52] 9

Chapter 2

Figure 2. 1. Void-matrix aggregate in which voids are distributed randomly (The macroscopic and microscopic stress tensors are shown.) 17

Figure 2. 2. Fractured surface during tensile tests under various pressures [40] 21

Figure 2. 3. Fractured surface of a tensile test under various pressures predicted using ABAQUS with a typical mesh in [94] 24

Figure 2. 4. Failure mechanism of a bending test for clad SS and Nb via roll bonding in [99] ... 26

Figure 2. 5. Schematic of fracture path progression in a clad sheet under bending [12] through (a) to (d) 27

Figure 2. 6. Mesh sensitivity on fracture pattern in a clad material under tension [100]. 29

Chapter 3

Figure 3. 1. Prolate ellipsoidal void configuration [37] 57

Figure 3. 2. Flow chart of the algorithm for the 3D case considering spherical voids 59

Figure 3. 3. Comparison results of our model and Aravas [35] 61

Figure 3. 4. Equivalent stress versus strain for different models in one 3D element..... 64

Figure 3. 5. Stress-11 versus strain-11 for different models in one 3D element..... 64

Figure 3. 6. Tensile test specimen geometry 67

Figure 3. 7. Comparison with experimental results for the isotropic case 68

Figure 3. 8. Comparison with experimental results for the anisotropic case using effective anisotropy coefficient 70

Figure 3. 9. A comparison of evolution of void volume fraction and void shape parameter with effective local plastic strain for initially spherical and ellipsoidal voids, (a) void volume fraction, and (b) void shape parameter S, in the anisotropic case using anisotropy coefficient 72

Figure 3. 10. fN sensitivity on ductile damage..... 73

Figure 3 .11 .fc sensitivity on ductile damage..... 74

Figure 3 12 .k sensitivity on ductile damage..... 75

Chapter 4

Figure 4. 1. Schematic of three-point bending test of a sheet metal under hydrostatic superimposed pressure 97

Figure 4. 2. FE configuration of three-point bending test; A typical mesh for metal sheet with 60×110 quadrilateral elements (CPE4R in ABAQUS/Explicit) 99

Figure 4. 3. Results comparison between ABAQUS/Explicit and ABAQUS/Standard 100

Figure 4. 4. Effect of mesh sensitivity on force-displacement curve at room pressure $\alpha = 0$ 102

Figure 4. 5. Effect of superimposed hydrostatic pressure on force-displacement curve 103

Figure 4. 6. Crack shapes of sheet metals under various superimposed hydrostatic pressures 104

Figure 4. 7. Predicted (a) normalized minimum cross-sectional area and (b) bending fracture strain for various values of α..... 105

Figure 4. 8. Effect of superimposed hydrostatic pressure on (a) hydrostatic pressure and (b) stress triaxiality at point A..... 107

Figure 4. 9. Predicted (a) void nucleation volume fraction, (b) void growth volume fraction and (c) total void volume fraction at point A for various values of α 108

Figure 4. 10. Effect of mesh sensitivity on (a) bending fracture strain and (b) gain in ductility..... 109

Figure 4. 11. Tensile test specimen; (a) schematic and (b) FE configuration with a typical mesh with 100×150 quadrilateral elements (CPE4R in ABAQUS/Explicit)..... 112

Figure 4. 12. Developed shear bands in tensile test specimen; (a) before fracture (b) after fracture..... 113

Figure 4. 13. Effective plastic fracture strain in bending and tensile tests..... 113

Figure 4. 14. Predicted (a) stress controlled void nucleation volume fraction, (b) void growth volume fraction and (c) total void volume fraction at point A for various values of α 115

Figure 4. 15. Effect of superimposed hydrostatic pressure on εN sensitivity 118

Figure 4. 16. Effect of superimposed hydrostatic pressure on fc sensitivity 119

Chapter 5

Figure 5. 1. The schematic of fracture path progression in a clad sheet under bending [21] through (a) to (d) 130

Figure 5. 2. Schematic of three-point bending test for a clad sheet metal 5.4. Results.. 134

Figure 5. 3. Uniaxial tension stress and strain curves of the core and cladding materials 136

Figure 5. 4. FE configuration of the three-point bending test: a typical mesh for a metal sheet with 30 × 500 quadrilateral elements (CPE4R in ABAQUS/Explicit) 138

Figure 5. 5. Effect of mesh sensitivity on the force–displacement curve $\Gamma = 0$ 139

Figure 5. 6. Effect of the mandrel span length on the bendability of sheet metals: (a) force–displacement curves and (b) bending fracture strains 141

Figure 5. 7. Effect of Γ on the force–displacement curves for three different Lm values: (a) $Lm2 = 4.5\ mm$ (b) $Lm2 = 5.0\ mm$, and (c) $Lm2 = 5.5\ mm$ 143

Figure 5. 8. Crack shapes of sheet metals for various Γ with three different cases: (a) $Lm2 = 4.5\ mm$, (b) $Lm2 = 5.0\ mm$, and (c) $Lm2 = 5.5\ mm$ 146

Figure 5. 9. Normalized minimum cross-sectional area ($Lm2 = 4.5\ mm$) 147

Figure 5. 10. Fracture bending strain; (a) $Lm2 = 4.5, bLm2 = 5.0$ and $Lm2 = 5.5$.... 148

Figure 5. 11. Effect of cladding on (a) hydrostatic pressure and (b) stress triaxiality at fracture sites ($Lm2 = 4.5\ mm$) 150

Figure 5. 12. Effect of Γ on void volume fraction ($Lm2 = 4.5\ mm$) 151

Figure 5. 13. Stress-strain curves for the matrix and cladding materials with various values of (a) "*K*" and (b) "*n*" 153

Figure 5. 14. Effects of "*K*" and "*n*" on force-displacement curves ($Lm2 = 5.5\ mm$) 154

Figure 5. 15. Effects of (a) "*K*" and (b) "*n*" on fracture bending strain ($Lm2 = 5.5\ mm$) 155

LIST OF TABLES

Chapter 3

Table 3. 1. Calibrated material parameters for the isotropic case 68

Table 3. 2. Calibrated parameters for the anisotropic case using effective anisotropy coefficient 70

Chapter 5

Table 5. 1. Matrix and cladding material constants..... 135

Nomenclature

Symbols	Definition	Units
a and b	major and minor radii of ellipsoidal voids	*mm*
$\bar{A}$	a parameter to define strain-controlled void nucleation in the GTN model	
A	cross-sectional area in bending specimen	*mm*
A and B	parameters to define stress-controlled void nucleation in the GTN model	
B, C and n	Swift law parameters	
c	foci of ellipsoidal voids	*mm*
$\boldsymbol{C}^{el}$	fourth-order elasticity tensor	*GPa*
$\boldsymbol{D}$	Jacobin matrix in Gurson model	*GPa*
$\mathbf{D}^{P}$	plastic strain rate tensor	s^{-1}
e_k	basic vectors of the Cartesian coordinate system	
$\in_N$	mean equivalent nucleating plastic strain in the GTN model	
E	Young's modulus	*GPa*
F, G, H, L, M and N	Hill's 48 constants	
f	void volume fraction in the GTN model	
f_c	critical void volume fraction in the GTN model	
f_f	void volume fraction at failure in the GTN model	
f_N	volume fraction of nucleating particles in the GTN model	
F	Force	*N*

G	shear modulus	*GPa*
H_{ijkl}	fourth-order anisotropy Hill's tensor	
H^{α}	internal state variables in the GTN model; α is the number of states	
$\boldsymbol{I}$	second-order identity tensor	
$\overline{k}$	slope of change in f in the GTN model	
K	bulk modulus	*GPa*
K and n	Power-law parameters	
L	length	*mm*
L_m	mandrel length span	*mm*
$\boldsymbol{L}$	macroscopic velocity gradient	*m/s*
n	matrix stress hardening factor	
p	imposed pressure	*MPa*
q	equivalent stress	*MPa*
q_1 and q_2	fitting parameters in the GTN model	
r	radius	*mm*
R_0, R_{45} and R_{90}	anisotropic plastic ratios	
R_p and R_m	punch and mandrel radii in the three-point bending test	*mm*
S	shape function ellipsoidal voids	
S_N	standard deviation in the GTN model	
S_{ij}	deviatoric stress tensor	*MPa*
t	time; thickness	*s; mm*

$\bar{t}$	cladding thickness	*mm*
W	elastic strain energy	*J*
i, j and k	1,2, 3	
α	superimposed pressure factor	
Γ	cladding thickness ratio	
Δ	increment	
d	punch stroke	*mm*
δ_{ij}	kronecker delta	
$\boldsymbol{\varepsilon}$	strain tensor	
ε_f^c	fracture bending strain	
$d\boldsymbol{\varepsilon}$	strain increment tensor	
ν	poison's ratio	
$\boldsymbol{\sigma}$	macroscopic Cauchy stress tensor	*MPa*
σ_e	equivalent stress	*MPa*
σ_H	hydrostatic stress	*MPa*
σ_y	yield stress	*MPa*
$\bar{\sigma}$	matrix stress	*MPa*
Φ	potential function in the GTN model	

Superscripts:

el	elastic
pl	plastic
$\cdot$	derivation
old	old value
new	new value

Subscripts:

$Applied, max$	maximum applied value
$0, 45$ and 90	0,45 and 90 degree directions
iso	isotropic
_	equivalent value
growth	void growth
min	minimum
max	maximum
nucleation	void nucleation
o	initial value
pred	predicted value

ABBREVIATIONS

EBSD	electron backscattered diffraction
FE	finite element
FEA	finite element analysis
FEM	finite element method
FLD	forming limit diagram
GTN	Gurson-Tvergaard-Needleman
LMCs	laminated metal composites
M-K	Marciniak-Kuczynski
Nb	Niobium
RSM	response surface methodology
SEM	scanning electron microscopy
SS	stainless steel
UMAT	user material subroutine
VVF	void volume fraction

CHAPTER 1 Introduction

1.1. Material modeling

Trial-and-error loops are eliminated using material models and simulation tools during the manufacturing and development of materials and relevant components. The material models illustrate the complexity of loads and make the predictions of material behavior feasible, especially in the development process.

Depicted in Figure 1.1, different fracture mechanisms, such as brittle, fully plastic, ductile, and shear, were explained by Ashby et al. [1]. Fracture mode changes under superimposed hydrostatic pressure or temperature. A fully plastic failure occurs when all other fracture mechanisms are suppressed. The material starts to neck, and strain localizes in the necked region. At constant strain, the section reduces to a point of zero area. Such a failure mode can occur under superimposed hydrostatic pressure when void growth and nucleation are suppressed.

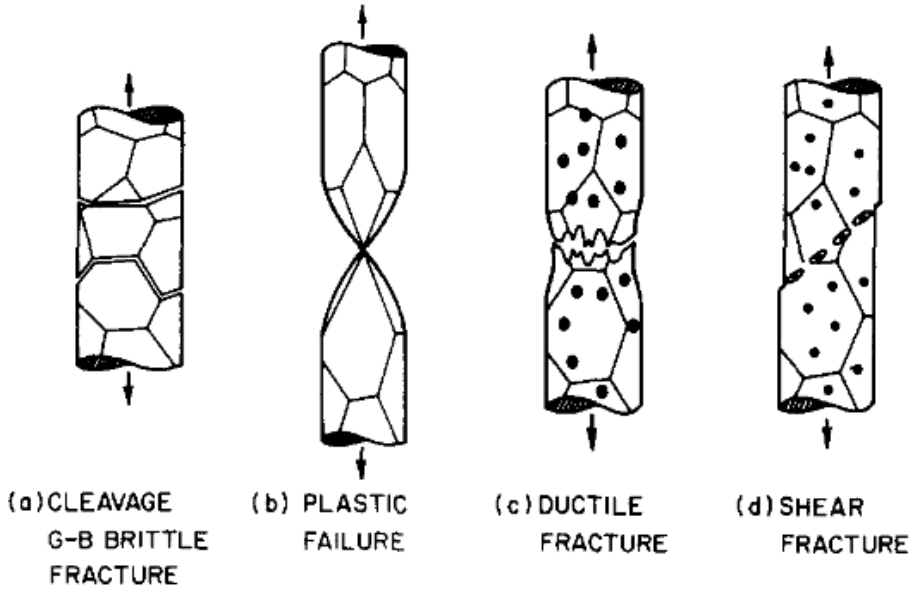

Figure 1. 1. Four different modes of fracture [1]

The nucleation, growth, and coalescence of microvoids are the most common phenomena leading to the ductile fracture of metals. Void nucleation is created by decohesion in the interface between matrix metals and second-phase particles or cracking in second-phase particles. Then, void grows with the development of localized plastic strain under tension. The ratio of the volume of voids to the total volume of a material is defined as the void volume fraction (VVF), which is denoted by f. $f = 0$ is assigned to a fully dense material without any void, whereas $f = 1$ is assigned to a material that is completely void and cannot carry any stress capacity. Coalescence occurs when two adjacent voids are extremely close to each other, voids begin to coalesce, and cracks and fractures exist. These steps are shown in Figure 1.2. Damage models can be utilized, in which the effects of

microstructural defects are considered in the definition of the relationship between material strength and every stage of a particular failure.

A proper material model should be defined for the capture of the mechanical behavior of metal deformation. Phenomenological models must reflect experimentation. Relations and material parameters are correlated with experimental observations. One of the typical phenomenological material models considering the effects of void growth and microvoid coalescence is the Gurson–Tvergaard–Needleman (GTN), which has been extensively used in industrial applications.

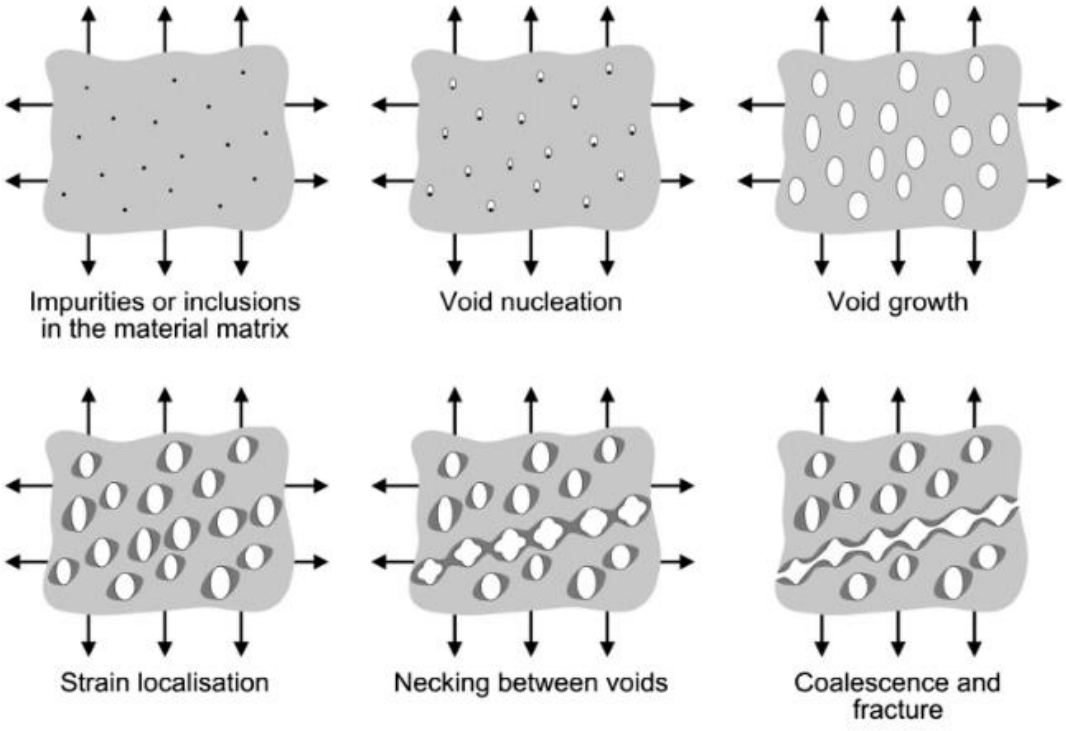

Figure 1. 2. Schematic of the nucleation, growth, and coalescence of voids [2]

Matrix materials are generally anisotropic. Anisotropy is inevitable in matrix materials during sheet production, particularly during cold rolling. The mechanical properties of metals directionally vary as a result of texture development in the plane defined by the rolling direction and the one normal to the plane of the sheet [3]. Several approximate yield criteria for anisotropic ductile materials, particularly the quadratic and nonquadratic yield criteria by Hill [4, 5], Hosford [6], and Barlat and Lian [7], can indicate the plastic responses of metals. Moreover, the Gurson model has been extended to be analytically suitable for anisotropic matrix materials on the basis of criteria, such as Hill's quadratic yield functions [8], Hosford's yield criterion [9, 10], and Barlat and Lian's nonquadratic anisotropic yield criterion [11].

1.2. Bending test

Bending is an important deformation mode in many applications, and it is a significant property in a range of applications and extensively used in the automotive industry [12, 13]. The bending properties of various materials have been studied in [14-16]. Z.S. Racz et al. [17] studied the relationship between the flexural properties and specimen aspect ratio of composite materials under a three-point bending test. A.R. Ragab and C.A. Saleh [18] evaluated the bendability of sheet metals and considered various void coalescence models. In [18], the effect of width/thickness ratio on bendability was studied. T. Feister et al. [19] studied failure predictions during the warm formation of a typical Al alloy under bending and presented the minimum radius/thickness ratio at which a sheet can be bent

over. A.A. Elsharkawy and A.A. El-Domiaty [20] determined stretch bendability limits and investigated springback limits in T-section beams. D.K. Leu [21] presented a simplified analytical approach and evaluated the bendability and springback of anisotropic sheet metals. J. Sarkar et al. [15] presented the tensile and bending properties of AA5754 Al alloys. D.J. Lloyd et al. [14] presented the bending properties of AA6111 and AA5754 Al alloys through a cantilever bending test. They also investigated the effect of prestrain on bendability. Using AA6016 sheets, L. Mattei et al. [12] investigated strain localization and damage mechanisms under bending through electron backscatter diffraction and optical microscopy. A. Davidkov et al. [23] investigated strain localization and damage mechanisms under bending in an Al–Mg alloy sheet through scanning electron microscopy (SEM) and optical microscopy. The mechanical performance of materials can be studied using a three-point bending test [24, 25], in which a sheets rests on two mandrels and a punch advances and deforms the sheet. The schematic of the three-point bending test is shown in Figure 1.3.

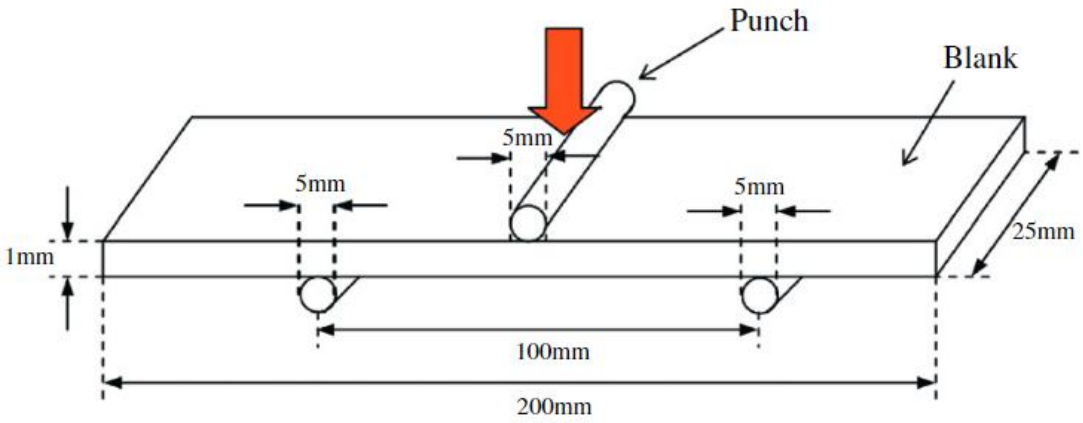

Figure 1. 3. Schematic of a three-point bending test [26]

1.3. Ductility enhancement in sheet metals

Increase in ductility is a desirable effect in sheet metal forming. Ductility enhancement can be performed in various ways, such as heat treatment [27], microstructural control [28, 29], stress-induced reverse transformation [30], superimposed hydrostatic pressure [1, 31-35], and cladding sheet metals [36-39]. Superimposed hydrostatic pressure and cladding sheet metals are performed structurally.

A superimposed hydrostatic pressure increases tensile ductility because it delays void growth and coalescence [8]. Superimposed hydrostatic pressure increases the ductility of sheet metals under tension [40] and bending [41]. In these studies, the specimens were inserted into load train assemblies in pressure vessels. Following fluid pressurization, the subsequent tension testing of the specimens was conducted at the desired level of

superimposed hydrostatic pressure. Figure 1.4 shows the schematic of a high-pressure testing apparatus used in [52]. This system consists of two cylindrical chambers, which are marked as "[1]" and "[2]" in Figure 1.4. These chambers are pressurized by the pressure pump supply shown as "[7]", and a broader gauge ("[8]") measures the pressure. A double-ended hydraulic cylinder marked as "[3]" drives a piston for loading and unloading samples. In this schematic, "[4]" refers to the pressure-compensated flow control valves that control the travel rate. "[5]" is a four-way valve that controls the direction of piston travel, and "[6]" is a pump unit that supplies the hydraulic cylinder.

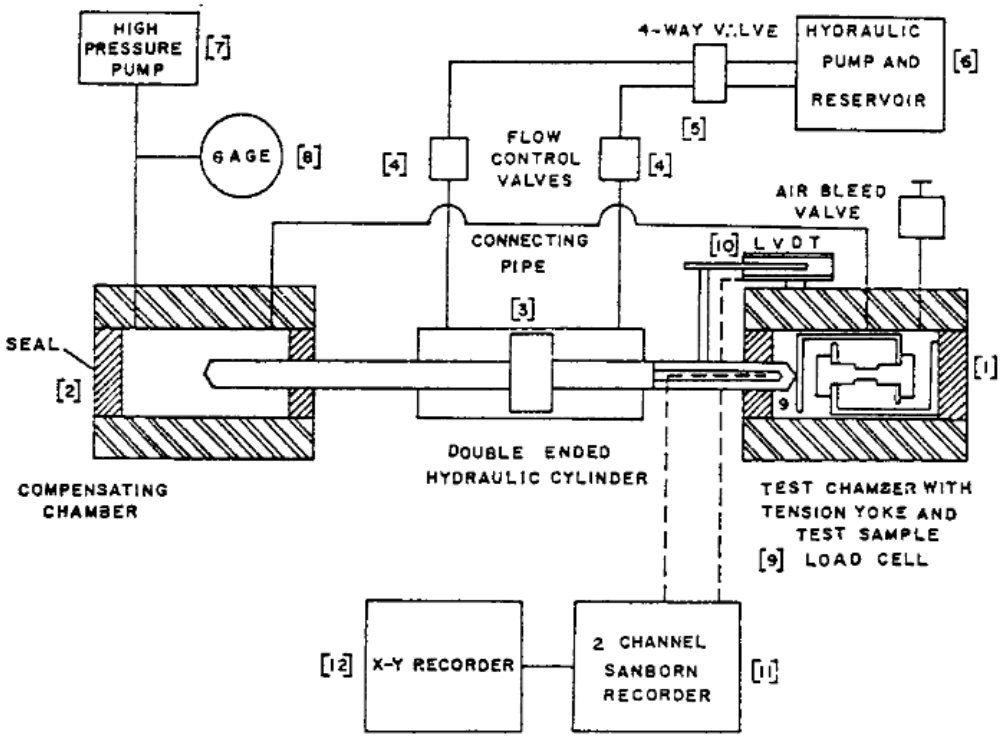

Figure 1. 4. Schematic of the high-pressure testing apparatus in [42]

Laminated metal composites (LMCs), which consist of various material layers, provide favorable composite properties unlike monolithic materials [43]. Figure 1.5 shows a clad specimen that consists of parent and clad layers [44], which are bonded. As stated in [45], LMCs can significantly improve many properties, such as fracture toughness [46], fatigue behavior [47], impact behavior [48], and formability or ductility [36-39]. Combined strength and ductility of metals can be provided in clad materials [49].

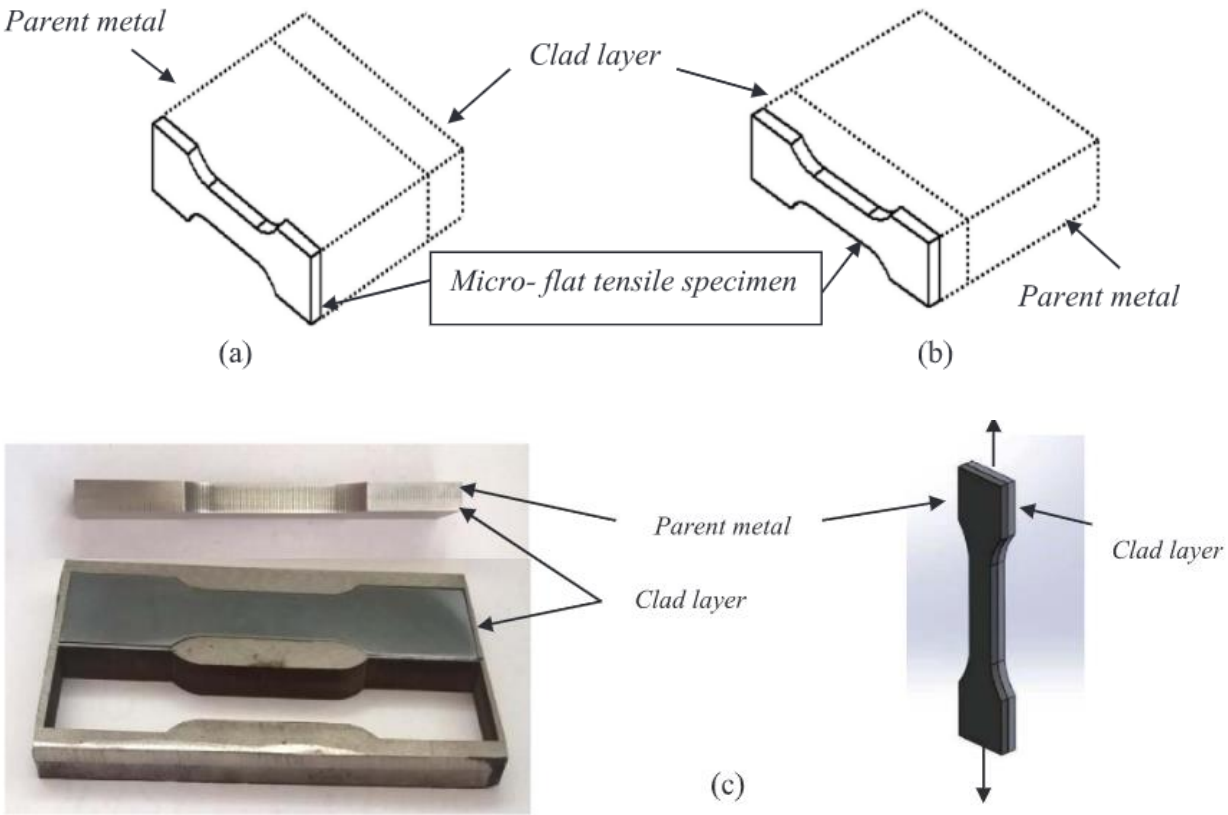

Figure 1. 5. Tensile specimens: (a) parent metal, (b) clad layer, and (c) tensile specimen of a clad material [44]

1.4. Finite element method

The finite element method (FEM) is a numerical method that approximately solves complex problems, such as partial, differential, and integral equations. This method is suitable for problems in which exact solutions cannot be obtained easily [50]. It was first introduced in the 1950s [51] and applied more to physical concepts than mathematical insights initially [52]. The concepts of FEM are dividing structures into several elements, analyzing each of the elements individually, and reconnecting the elements by nodes that hold the elements together [52]. Figure 1.6 demonstrates a typical structure that is divided into several elements [52]. The nodes that hold the elements together are also shown.

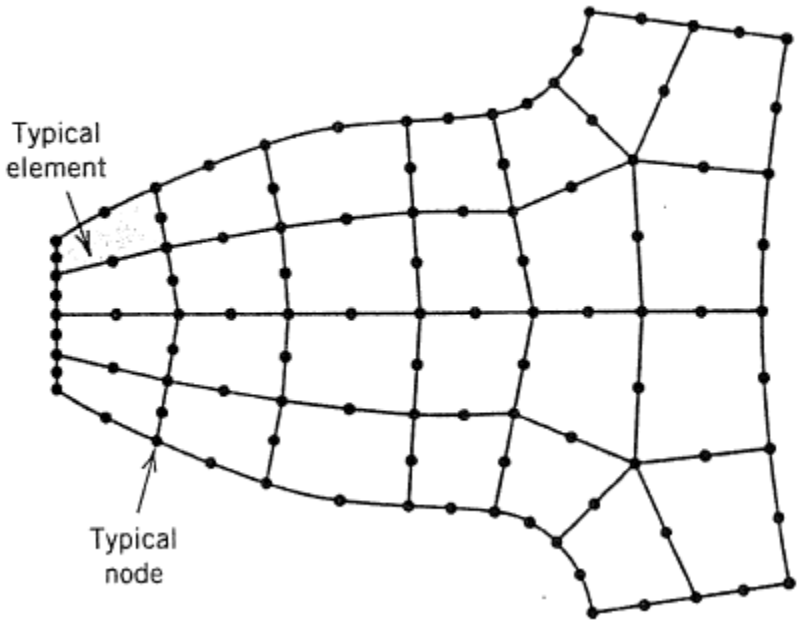

Figure 1. 6. FE mesh for gear tooth [52]

Owing to the developments in computer equipment since the 1950s and the invention of the CAD system, all problems can be simulated through FEM. Several finite element (FE) commercial packages, such as ANSYS, ABAQUS, SAS, NASTRAN, and LS-DYNA, are available. Each software has its own capabilities. ABAQUS is used in this work.

The FEM subdivides a continuum system into simpler FEs. This approach analyzes the element properties mathematically and assembles the results of every element in calculating the approximate behavior of an entire system. FEM can be used to predict metal-cutting performance, such as the wear of tools and the plastic deformation of machined workpieces. W. Cha and N. Kim [53] used FEM to quantify the microcracks on the bending surface of roll-formed products. Z.W. Liu et al. [54] used FE software LS-DYNA to study the influence of heat treatment conditions on the bending properties of a typical Al alloy. C. Soyarslan [55] used FE software ABAQUS to investigate ductile fracture in bending for dual-phase steels. J. H. Kim et al. [56] studied the draw–bend failure of advanced high strength steels through FEM. Y. Shi et al. [13] used ABAQUS to analyze the surface roughening in AA6111 Al alloy under bending. J. Kim et al. [26] implemented a constitutive law to describe the anisotropic and asymmetric mechanical behavior of a typical Mg alloy sheet in ABAQUS. L. Jin et al. [57] performed an in situ investigation on the microstructural evolution and plasticity of Mg alloys under bending and compared the results with those obtained using FEM. V. L. Tagarielli [58] analytically studied the collapse response of sandwich beams under bending and compared the results with those obtained using FEM. P. Hou et al. [24] studied the influence of punch radius on elastic modulus in a three-point bending test using FEM.

1.5. Problem formulation and research scope

This thesis compiles the results presented in three peer-reviewed journals. They are structured as follows:

1.5.1. Anisotropic Gurson–Tvergaard–Needleman plasticity and damage model for finite element analysis of elastic–plastic problems

Although in [59-61], the GTN model was extended for anisotropic materials using the algorithm presented by N. Aravas [62] on the basis of Hill's quadratic anisotropic yield criterion, and the exact algorithm for isotropic matrix material was applied. N. Aravas [62] presented a lucid algorithm for the GTN model, but it works solely for isotropic metals. In [59-61], the effective stress for isotropic materials was replaced with the effective stress for anisotropic materials, and this approach cannot be accepted. In the current study, the algorithm presented in [62] is analyzed in detail and extended to be suitable for anisotropic materials in ABAQUS-Standard FE code, and changes in the algorithm are made when necessary. The algorithm is prepared for 3D and plane stress elements and implemented for ellipsoidal- and spherical-shaped voids. The results of each case in tensile tests are obtained and compared with those in experiments.

1.5.2. Study of the influence of superimposed hydrostatic pressure on the bendability of sheet metals

As mentioned previously, the ductility of metals is desired to enhance, and one of the methods is to superimpose hydrostatic pressure. Hydrostatic pressure delays the void growth and nucleation and significantly increases fracture strain. This phenomenon is numerically studied in ABAQUS by using the GTN model, and the effect of hydrostatic pressure on sheet metals under a three-point bending test is analyzed. The reasons for increased bendability by hydrostatic pressure are elucidated. The results of a bending test under various hydrostatic pressures are compared with those under tension. A sheet metal has more deformation under bending than under tension. Overall, this study aims to understand what causes the increase in bendability by superimposed hydrostatic pressure.

1.5.3. Enhanced bendability in sheet metals produced by cladding a ductile layer

Cladding sheet metals is another method for enhancing ductility. Cladding a sheet metal with a soft material increases ductility because the development of stress triaxiality is inhibited. This condition causes considerable increases in bendability and fracture strain. The numerical study of this phenomenon is performed in ABAQUS using the GTN model under a three-point bending test. The reasons for increased bendability by cladding are elaborated. The results for different mandrel span lengths and cladding thickness ratios (Γ) are presented. The changes in the fracture initiation transition zone are numerically

analyzed. The effect of hardening on clad materials is investigated, and the result indicates that bendability increases with the rate of hardening in clad materials. This study aims to determine what causes the increase in bendability by cladding sheet metals.

1.6. Contribution of research

This work:

[1]. Implementation of the GTN model suitable for anisotropic metals and presentation of the correct algorithm

[2]. Implementation of the GTN model considering ellipsoidal microvoids in a matrix material and analysis of its effects on the uniaxial stress–strain response of the material

[3]. Numerical study of the effect of superimposed hydrostatic pressure on bendability

[4]. Numerical study of the effect of cladding on bendability

1.7. Organization of research and thesis document

This thesis is based on three journal articles that constitute the result section of the thesis along with other supplementary chapters that provide a survey of related literature and context, conclusions, and recommendations. The information provided in this study is presented in six chapters:

Chapter 1 presents an introduction to the GTN model and the effects of superimposed hydrostatic pressure and cladding on the bendability of sheet metals.

Chapter 2 consists of a review of the studies conducted on the GTN model and the effects of superimposed hydrostatic pressure and cladding on the bendability of sheet metals.

Chapter 3 is about the first journal article entitled "Anisotropic Gurson-Tvergaard-Needleman Plasticity and Damage Model for Finite Element Analysis of Elastic-Plastic Problems." It presents an implementation and description of an anisotropic GTN model for sheet metals.

Chapter 4 focuses on the second journal article entitled "Study of influence of superimposed hydrostatic pressure on the bendability of sheet metals." It presents the effect of hydrostatic pressure on the bendability of sheet metals.

Chapter 5 concentrates on the third journal article entitled "Enhanced bendability in sheet metals produced by cladding a ductile layer." It presents the effect of cladding on the bendability of sheet metals.

Chapter 6 provides conclusions and recommendations for future work.

1.8. A note to the reader

As a result of the editorial requirements for publishing a series of separate journal articles, some overlap of materials contained in this thesis occurs. In particular, the sections of each journal article pertaining to numerical modeling are repeated. The literature review section of each article also contains similar materials. However, each of these review sections is targeted and does contain specific references related to the work presented in each paper.

Chapter 2 Literature Review

2.1. Introduction

This thesis section provides a comprehensive review of the relevant studies on the GTN model and its applications for increasing the ductility and bendability of metals. The literature reviewed in each journal article contained in this thesis is relatively brief to fit the publication requirement. A detailed review is presented in this chapter to provide insights and context to the work performed in this thesis. The chapter begins with a discussion of the GTN model, followed by a review of its application for increasing the ductility and bendability of metals by superimposing hydrostatic pressure and cladding sheet metals.

2.2. Gurson-Needleman-Tvergaard model

Gurson [63] presented a widely constitutive law for the plastic response of porous metals in 1977. In this model, the effect of hydrostatic pressure and the effect of void growth on flow stress are considered. The yield criterion is approximated using the upper bound approach. A unit cube containing a spherical void is considered a representative volume element (Figure 2.1). The matrix material is homogeneous, incompressible, and rigid–

plastic and follows the von Mises criterion. A velocity field is applied to the unit cell conforming to the macroscopic stress state of the material. Upper bounds to the macroscopic stress fields required for yield are obtained using a distribution of macroscopic flow fields and by working through a dissipation integral. Then, the yield locus is formed by the locus in the stress space of upper bounds to the macroscopic stress fields. The flow rule results for this yield locus are shown. Gurson developed the approximate functional forms for yield loci. The obtained approximate yield is as follows:

$$\Phi(\boldsymbol{\sigma}, \bar{\sigma}, f) = \frac{\sigma_e^2}{\bar{\sigma}^2} + 2f cosh\left(\frac{3q_2\sigma_H}{2\bar{\sigma}}\right) - [1.0 + f^2] = 0 \quad (1)$$

where $\boldsymbol{\sigma}$ is the macroscopic Cauchy stress tensor; σ_e, σ_H, and $\bar{\sigma}$ are the equivalent, hydrostatic, and matrix stresses, respectively; and f is the void volume fraction.

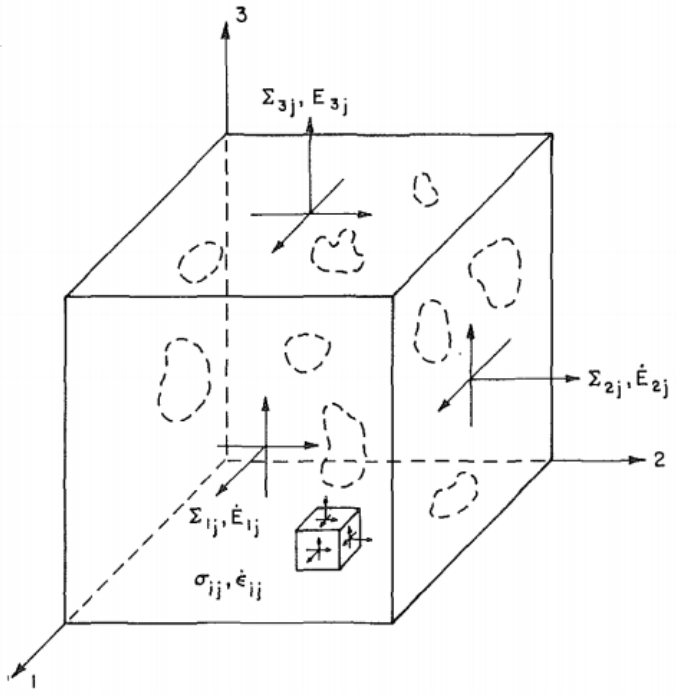

Figure 2. 1. Void-matrix aggregate in which voids are distributed randomly (The macroscopic and microscopic stress tensors are shown.)

Researchers have found the Gurson model attractive and used this model in analyzing various applications. The model can be used to predict the analytical forming limit diagram (FLD). One of the well-accepted approaches for the analytical prediction of FLD for sheet materials is the so-called Marciniak–Kuczynski (M–K) method [64]. A slight reduction in sheet thickness in the form of a band in a certain region of the sheet specimen as a pre-existing imperfection is considered in this method. Gurson's original model for isotropic matrix materials has been extended analytically for anisotropic matrix materials on the basis of several criteria, such as Hill's quadratic yield functions [8], Hosford's yield criterion [9, 10], and Barlat and Lian's nonquadratic anisotropic yield criterion [11]. Son

and Kim [65] used the extension of the Gurson model based on Barlat 89 to predict the analytical FLD through the M–K method.

In 1982, Viggo Tvergaard [66] analyzed the macroscopic properties of a porous ductile medium by using the approximate yield function suggested by Gurson and showed that the Gurson model does not prove a good agreement to analyze bifurcation into a localized mode under several loading conditions. Therefore, V. Tvergaard [66] modified the model and presented the following approximate yield function:

$$\Phi(\boldsymbol{\sigma}, \bar{\sigma}, f) = \frac{\sigma_e^2}{\bar{\sigma}^2} + 2f^* q_1 cosh\left(\frac{3q_2\sigma_H}{2\bar{\sigma}}\right) - [1.0 + (q_2 f^*)^2] = 0 \quad (2)$$

Here, when $q_1 = q_2 = 1.0$, Equation (2) turns into the approximate yield function suggested by Gurson (Equation [1]). From [66], the results for values $q_1 = 1.0$ and $q_2 = 1.5$ are in good agreement and can be used to analyze the bifurcation mode of porous metals. The Gurson model was modified by V. Tvergaard and A. Needleman [67]. They introduced additional damage parameters and considered void coalescence and ductile fracture. In this modified model, referred to as the GTN model, the damage-induced plastic instability (or necking) process is governed by the growth of existing voids, the nucleation of new voids during deformation, and the microcrack coalescence in the neck region. The approximate yield function for the GTN model is as follows:

$$\Phi(\boldsymbol{\sigma}, \bar{\sigma}, f) = \frac{\sigma_e^2}{\bar{\sigma}^2} + 2f^* q_1 cosh\left(\frac{3q_2\sigma_H}{2\bar{\sigma}}\right) - [1.0 + (q_2 f^*)^2] = 0 \quad (3)$$

and $$f^* = \begin{cases} f & for\ f \le f_c \\ f_c + \frac{f_u^* - f_c}{f_f - f_c}(f - f_c) & for\ f > f_c \end{cases}$$

where f_c is the critical void volume fraction when coalescence occurs, and f_f is the void volume fraction at failure. Lastly, the parameter $f_u^* = \frac{1}{q_1}$ is defined. The growth of existing voids and the nucleation of new voids are considered in the evolution of void volume fraction $\left(\dot{f} = \dot{f}_{growth} + \dot{f}_{nucleation}\right)$. The growth of existing voids is a function of a plastic strain rate, and the growth of voids because of the nucleation of new voids is based on a normal distribution, as suggested by Chu and Needleman [68].

A. Needleman and V. Tvergaard [69] used the GTN model and analyzed the ductile fracture in axisymmetric and plane strain notched tensile specimens. From [69], failure occurs at the center of the notched section of axisymmetric specimens; on the contrary, failure occurs on the surface in plane strain specimens with sharp notches, and this condition is in good agreement with experiments. W. Cha and N. Kim [53] identified GTN parameters using load-displacement curves obtained from a tensile test through the response surface method. The obtained parameters were used in ABAQUS for the simulation of the bending test. Void volume fraction (f) on the outer surface of a specimen was observed and compared with the microcrack size observed using SEM. The result indicated that GTN can be used to quantify the microcrack size observed in SEM. The GTN model has an extensive use in the analysis of different plastic deformation processes [59-61, 70-80]. T.N. Zaman [81] used the GTN model in the M–K method to predict analytical FLD and studied the effect of strain path changes on predicted FLD.

Aravas [62] presented a numerical implementation of the isotropic GTN model into ABAQUS/Standard FE code in 1987, in which 3D and plane stress cases were considered. In this algorithm, the spherical-shaped voids considered in the original GTN model [67] are used. The backward Euler method, which is unconditionally stable and suitable for finite element analysis (FEA), is used. This method is also the most accurate member of the generalized trapezoidal family for strain increments that are several times the size of the yield surface in strain space. The algorithm was integrated implicitly, and the tangent moduli were obtained by consistent linearization of the elastoplastic constitutive equations. The results for the tensile test obtained using the algorithm presented by Aravas have been tested with the numerically obtained exact solution, and the results are compared [62].
Numerical implementations and subsequent studies of the combination of the earlier GTN model with some of new yield criteria are presented in [8-11, 71-80, 82-87]. Furthermore, the GTN model has been extended and transformed from an isotropic matrix material to an anisotropic matrix in [59-61] on the basis of the algorithm presented by N. Aravas [62]. Hill's quadratic anisotropic yield criterion was used in these studies for the definition of equivalent stress. On the contrary, the exact algorithm for isotropic materials is applied in the new anisotropic implementation of the GTN model.

2.3. Effect of superimposed hydrostatic pressure

The effect of superimposed hydrostatic pressure on void formation in a tensile test was characterized using quantitative metallography, and the fracture mechanism was analyzed

through fractography in [40]. A significant increase in the ductility of metals occurred with the suppression of microvoid development, and the flow stress change was negligible. From [40], externally applied pressure excludes the void-sheet mechanism, which is letting shear decohesion to be the dominant failure mechanism because it is minimally sensitive to hydrostatic pressure. In this way, the cup–cone mode of fracture under atmospheric pressure changes to a slanted structure under high superimposed hydrostatic pressure, as shown in Figure 2.2.

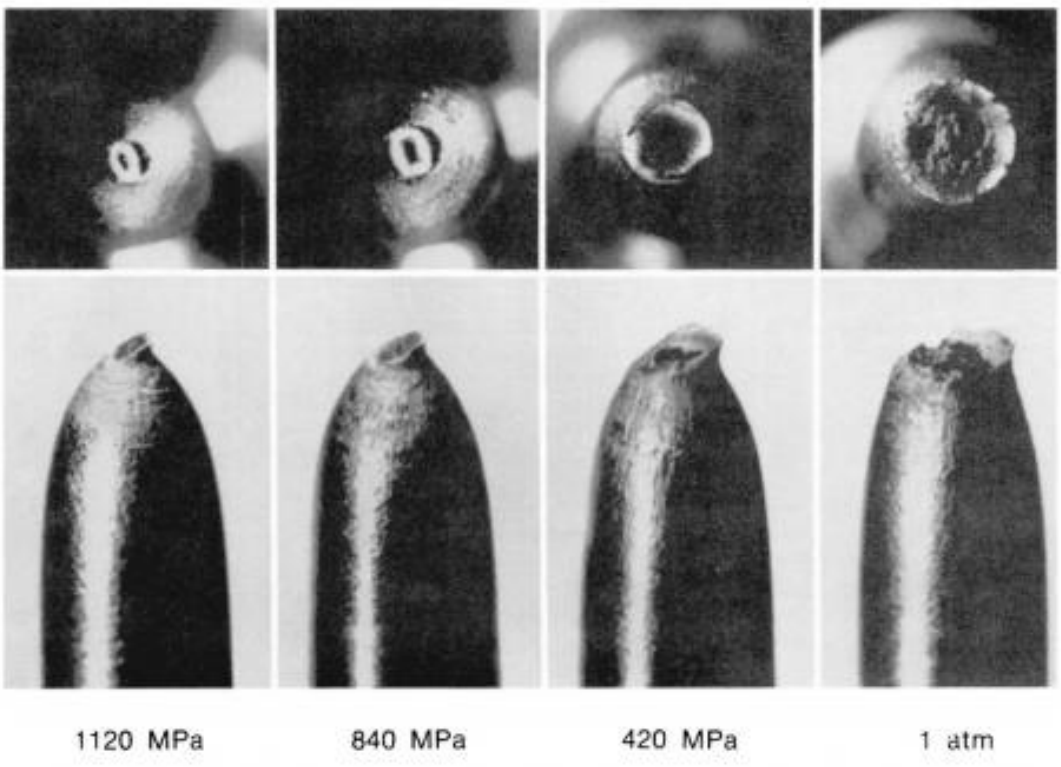

Figure 2. 2. Fractured surface during tensile tests under various pressures [40]

The effect of superimposed hydrostatic pressure on the bending fracture strain of low-carbon steel containing globular sulfides was studied by Kao et al. [41]. Superimposed hydrostatic pressure considerably increased fracture strain and enhanced bendability. The experimental results presented in [41] showed that the fracture was due to the nucleation, growth, and coalescence of voids; superimposed hydrostatic pressure delayed or completely eliminated the nucleation, growth, and coalescence of voids, which resulted in increased fracture strain and bendability. Weinrich and French [88] investigated the effect of superimposed hydrostatic pressure on the fracture mechanisms of sheet tensile specimens. They found that the mode of fracture at room pressure was smooth and planar (P-type) and changed to a chisel edge without any void sheet (C-type) at increased hydrostatic pressure. Brownrigg et al. [33] showed that hydrostatic pressure insignificantly affected the neck development in 1045 steel under tension, flow stress increased slightly, and superimposed hydrostatic pressure considerably affected fracture and delayed void growth and nucleation. French et al. [32] demonstrated that the fracture strain for free machining brass was sensitive to the effect of hydrostatic pressure below 300 MPa but was minimally sensitive above this value. In [32], the resultant triaxial stress component became tensile at the late stage of deformation, and a highly developed neck existed in the specimen. Voids were developed in a narrow region near the neck center. Fracture occurred with further deformation, and this condition was the reason for the minimally sensitive fracture strain at high pressure. Korbel at al. [34] performed experiments to show the effect of superimposed hydrostatic pressure on the formation of localized shear bands in a naturally aged A–Zn–Mg alloy. The onset of localized shear was independent of the

superimposed hydrostatic pressure, and localized shear was created because of structural softening. On the contrary, fracture strain increased with hydrostatic pressure because it delayed the void growth and nucleation. French et al. [35] showed that the relative area of void coalescence in Cu under tension decreased with an increase in hydrostatic pressure, whereas the relative area of shear bands increased. Superimposed hydrostatic pressure is generally accepted to increase ductility because it delays or completely eliminates void growth and nucleation, as determined in [42, 89, 90].

In [91, 92], the effect of superimposed hydrostatic pressure on the formability of sheet metals was studied by constructing FLD on the basis of the M–K approach, and the authors found that pressure delayed the initiation of necking and that formability increased. The transition of fracture surface in a tensile round bar from a cup–cone mode under atmospheric pressure to a slanted structure under high pressure was numerically reproduced through the GTN model. Peng et al. [93] investigated the effect of superimposed hydrostatic pressure on fracture in round bars. They showed that superimposed pressure had no evident effect on necking strain because void growth was insignificant prior to necking. The numerical results showed that the fracture strain increased due to the fact that superimposed pressure delays or eliminates the void nucleation and growth completely. The fracture surface changed from a cup–cone mode under atmospheric pressure to a slant smooth surface under high pressure. Superimposed pressure not only increased the fracture strain but also extended the failure process. The effect of superimposed pressure on fracture in sheet metals under tension was studied in [94]; the author found that hydrostatic pressure increased the ductility of sheet metals, and

the numerical results showed the transition of fracture surface from P-type mode at atmospheric pressure to C-type mode under high pressure occurred. The fractured surface of specimens predicted using ABAQUS in [94] is shown in Figure 2.3.

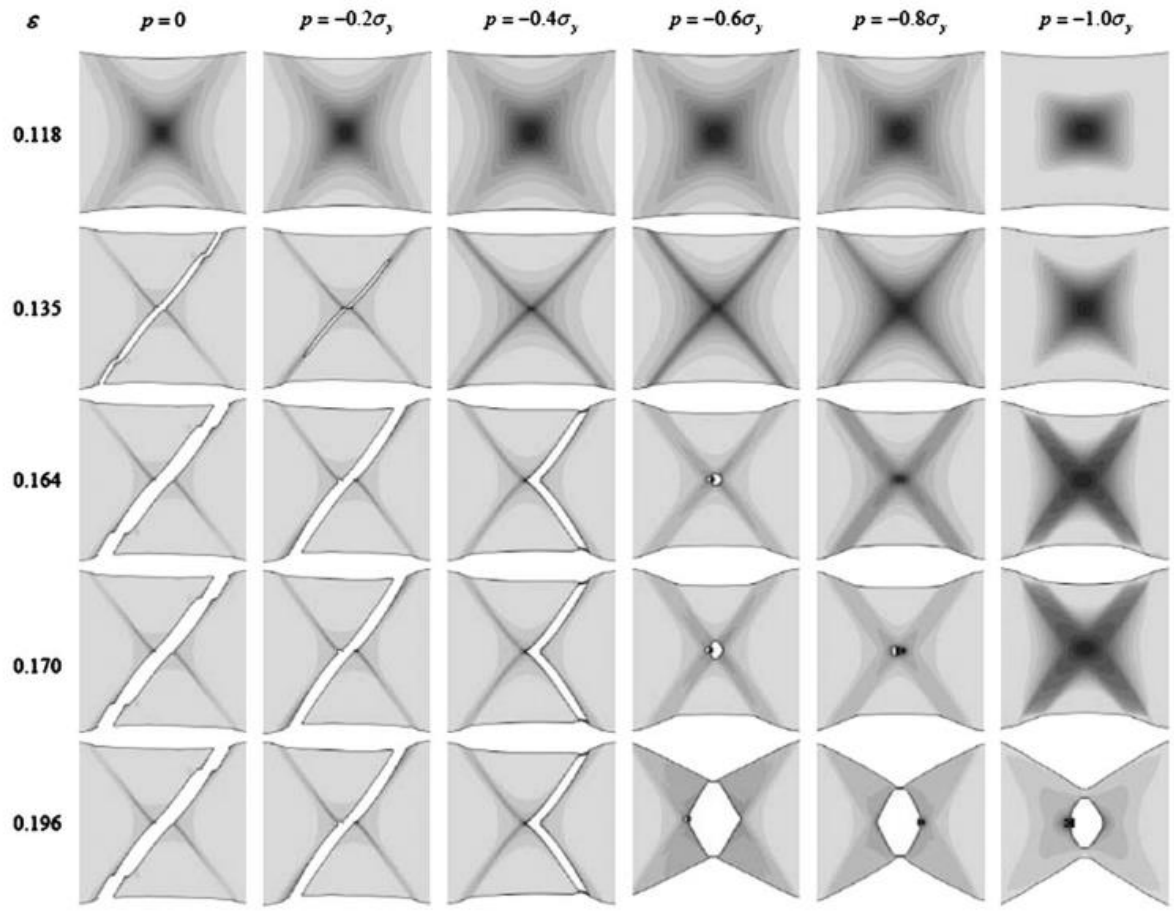

Figure 2. 3. Fractured surface of a tensile test under various pressures predicted using ABAQUS with a typical mesh in [94]

In [95], the effect of superimposed hydrostatic pressure on bendability was numerically investigated, and hydrostatic pressure was observed to increase fracture strain. The effect of superimposed double-sided pressure on the formability of a biaxially stretched AA6111-

T4 sheet metal was numerically studied in [96] via the GTN model; the author found that double-sided pressure increased formability, void nucleation was invariable, and only void growth changed and decreased with an increase in pressure.

2.4. Effect of cladding on the ductility of metals

Hu et al. [97] studied the necking behavior of cladding sheets with a rate-sensitive layer cladding on a rate-insensitive core material. A nonlinear long-wavelength analysis was developed and used in predicting the onset of necking. This mode of analysis is similar to that presented by Hutchinson and Neale in 1977 [98]. However, it has been verified by FEM. In [97], necking strain increases with the strain-rate sensitivity of the clad layer at a fixed volume fraction of cladding, and the necking localization is retarded after volume fraction of the cladding layer is increased.

Stainless steel (SS) was clad with Niobium (Nb) in [99] by roll bonding, and a micron thick layer at the interface was generated during annealing. This layer led to a brittle failure along the interface between SS core and Nb cladding (Figure 2.4). Hot rolling can provide a shear bond strength as reported in [44], for a low-carbon steel/austenitic SS clad composite. However, roll bonding is costly, and the “Fusion Technology” technique introduced by Novelis Inc. clad sheet metals with a high-strength and oxide-free zone at the clad–core interface [37]. Tensile and bending tests for a clad material consisting of ×609 core and soft AA3003 clad materials were performed in [12], and the results were used in confirming the high strength of the clad–core interface. A failure occurred away

from the clad–core interface. This finding showed that the two materials were bonded perfectly without any delamination.

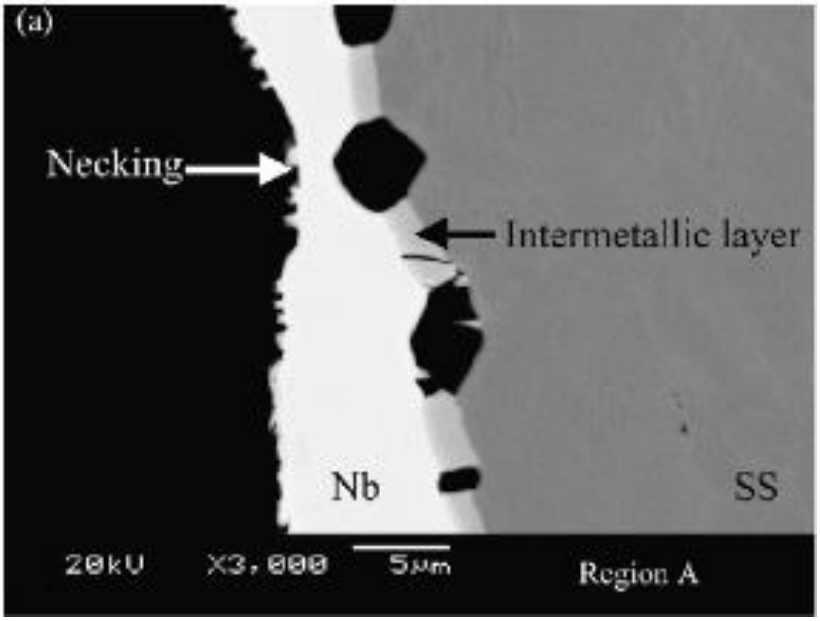

Figure 2. 4. Failure mechanism of a bending test for clad SS and Nb via roll bonding in [99]

Fracture under bending was initiated on the outer surface of a specimen, which was a free and unconstrained surface due to the strain localization in severe bands developed at grain boundaries [12]. Superimposed hydrostatic pressure delays the void growth and coalescence of microvoids and increases bendability [31, 41, 95]. However, bendability can be improved by cladding a material on the outer surface with a ductile clad layer [12]. The Fusion Technology technique was used in [12], and the author found that failure initiated in a region close to the core–clad interface and then propagated toward the surface of the bent sample; eventually, cladding failed, and the crack grew. This phenomenon

proved that a perfect bonding is provided in a clad sheet metal using the Fusion Technology technique. Figure 2.5 shows the mechanism of fracture progression in a clad sheet metal under bending.

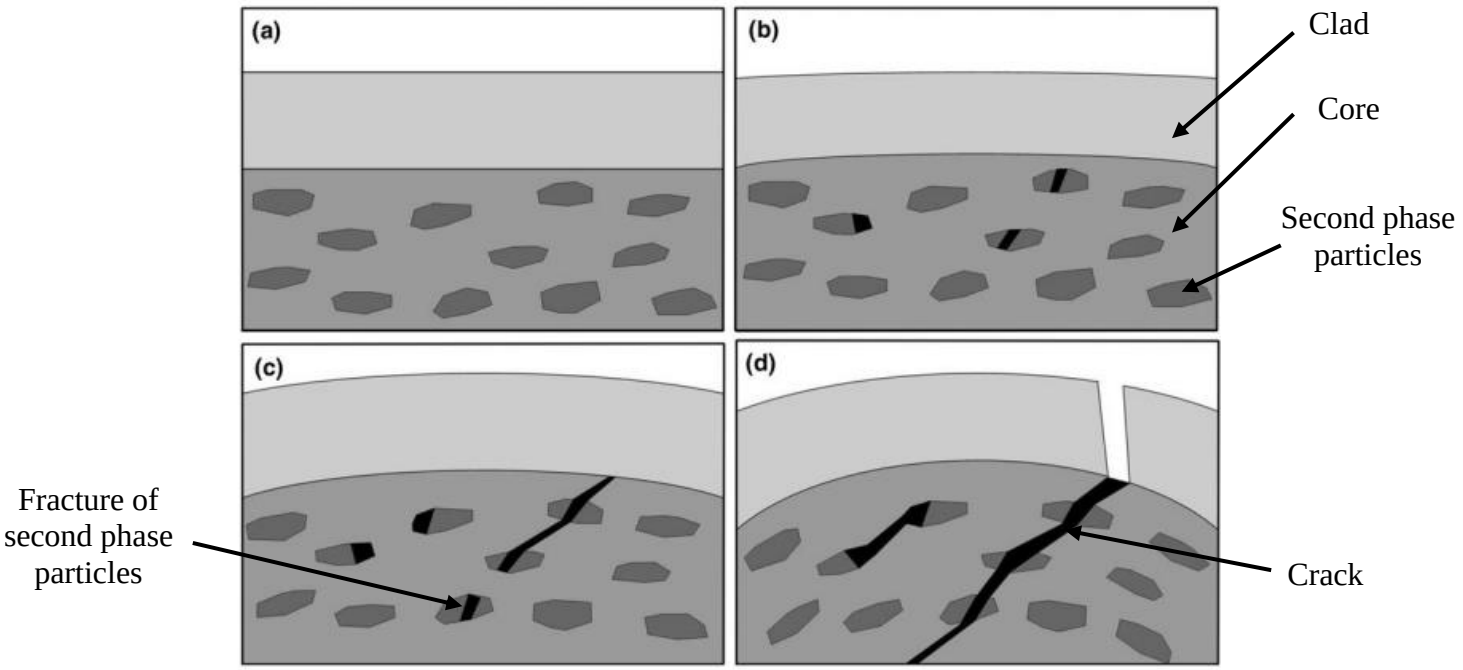

Figure 2. 5. Schematic of fracture path progression in a clad sheet under bending [12] through (a) to (d)

Chen et al. [100, 101] investigated the effect of cladding a ductile layer in ring and sheet metals under plane strain tension on necking and fracture strains through FEM. Cladding a ductile ring increases necking and fracture strains. Cladding enhanced the hardening, and necking strain increased following the rule of mixture. As necking strain increased, cladding delayed the void nucleation and growth, which resulted in significant ductility. The topological arrangement of cladding in the ring was investigated. Although the

topological arrangement of the cladding ring exhibited an evident effect on fracture strain, the necking strain was unaffected following the rule of mixture. The authors of [100, 101] explained that cladding delayed the growth of stress triaxiality. Stress triaxiality presented a significant effect on void growth and coalescence. Therefore, cladding helped delay the fracture initiation in sheet metals. Mesh sensitivity was inevitable in predicting the fracture pattern on clad tensile samples. A fracture pattern with two different meshes for various Γ is shown in Figure 2.6. Mesh has a significant effect on the prediction of fracture pattern.

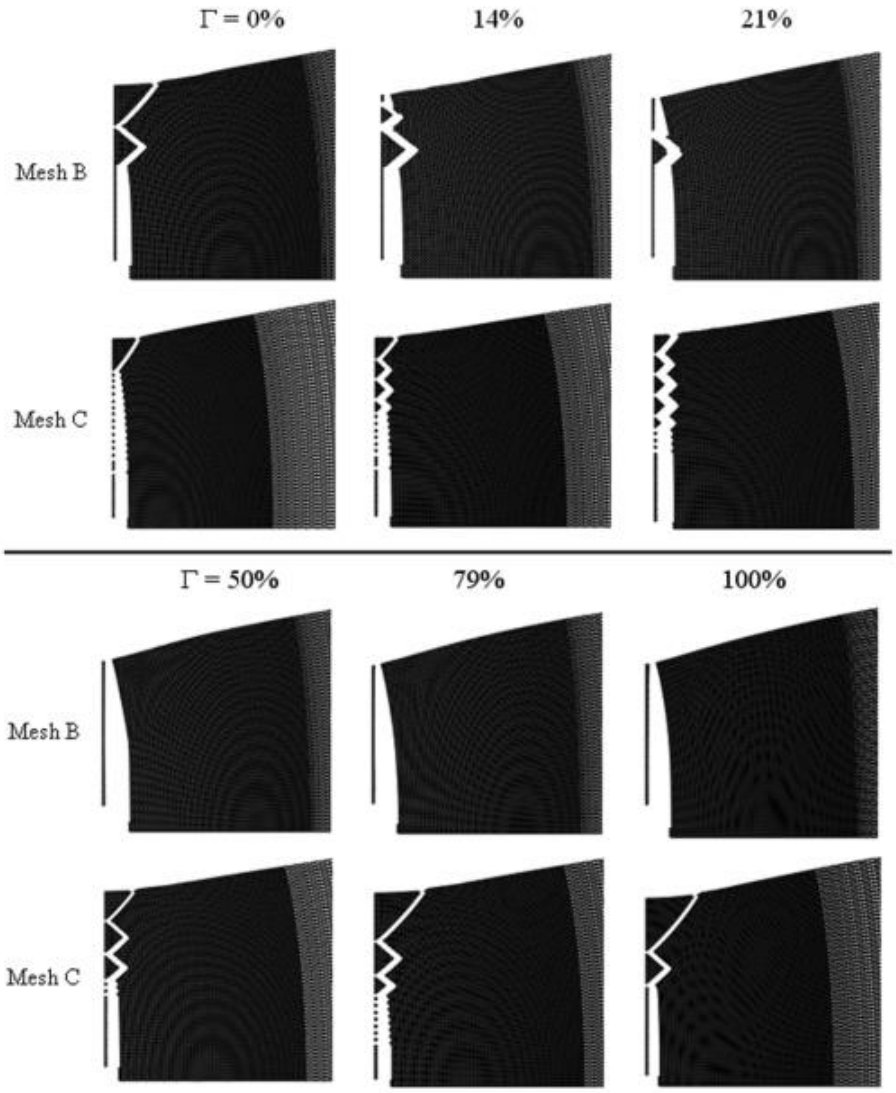

Figure 2. 6. Mesh sensitivity on fracture pattern in a clad material under tension [100]

2.5. Summary

GTN [67] is a pressure-dependent model, and the effect of void growth on the plastic flow stress of metals is considered. Coalescence occurs when the void volume fraction reaches

a critical value. The GTN model has been extended and presented in this form after a couple of extensions and modifications. It is used in analyzing various applications, such as the prediction of analytical FLD in the M–K method. Furthermore, GTN is used in FEM and established on FE ABAQUS software by using an algorithm via the backward Euler method [62]. Diverse analyses in the elastic–plastic response of metals have been performed using the GTN model.

Superimposed hydrostatic pressure delays the void growth and coalescence in metals and helps delay fracture initiation [40]. Several experiments in this regard have been performed through tensile tests. Hydrostatic pressure changes the fracture mode in tensile tests, excludes the void-sheet mechanism, and leads to shear decohesion. Fracture strain increases, given that shear decohesion is insensitive to hydrostatic pressure. Numerical studies of the effect of superimposed hydrostatic pressure on the ductility of metals under tension have been performed using the GTN model [91, 92]. Articles have explained that hydrostatic pressure delays void growth and coalescence and fracture strain increases.

Cladding sheet metals with a highly ductile material enhances the ductility. Tensile tests of clad sheet metals produced using a Fusion Technology technique were performed in [37], and fracture occurred away from the clad–core interface. The Fusion Technology effectively bonded the two materials. Numerical studies of the effect of cladding on the ductility of sheet metals were performed in [100, 101]. These articles numerically demonstrated that cladding sheet metals delays the development of stress triaxiality and helps increase fracture strain.

CHAPTER 3

Anisotropic Gurson-Tvergaard-Needleman plasticity and damage model for finite element analysis of elastic–plastic problems

Complete citation:

M.M. Shahzamanian, "Anisotropic Gurson-Tvergaard-Needleman plasticity and damage model for finite element analysis of elastic-plastic problems" International Journal of Numerical Methods in Engineering, 115 (2018) 1527-1551.

Copyrights:

Relative contributions:

M.M. Shahzamanian: Performed all the simulations, interpretation and analysis of the data, wrote the draft of the manuscript including all figures and text and is responsible for the final draft submittal to the journal.

ABSTRACT

Implementation and analysis of the anisotropic version of the Gurson–Tvergaard–Needleman (GTN) isotropic damage criterion are performed on the basis of Hill's quadratic anisotropic yield theory with the definition of an effective anisotropic coefficient to represent the elastic–plastic behavior of ductile metals. This study aims to analyze the extension of the GTN model suitable for anisotropic porous metals and to investigate the GTN model extension and its effects on the stress–strain curves of metals. An anisotropic damage model is implemented using the user material subroutine in ABAQUS/standard finite element (FE) code. The implementation is verified and applied to simulate a uniaxial tensile test on a commercially produced aluminum sheet material for three-dimensional and plane stress test cases. Spherical and ellipsoidal micro voids are considered in the matrix material, and their effects on the uniaxial stress–strain response of the material are analyzed. Hill's quadratic anisotropic yield theory predicts substantially large damage evolution and a low stress–strain curve compared with those predicted by the isotropic model. An approximate model for anisotropic materials is proposed to avoid increased damage evolution. In this approximate model, Hill's anisotropic constants are replaced with an effective anisotropy coefficient. All model-generated stress–strain predictions are compared with the experimental stress–strain curve of AA6016-T4 alloy.

Keyword: GTN model, Hill's quadratic anisotropic yield criterion, finite element method, ductile metals.

3.1. Introduction and a brief review of literature

Computational simulations with the use of the finite element method are commonly conducted to elucidate the plastic deformation and damage behavior of materials. The elastoplastic behavior of many metallic materials involves void nucleation, growth, and coalescence of micro-voids. Gurson–Tvergaard–Needleman (GTN) is a pressure-dependent plasticity and damage model that was proposed for isotropic materials [1-4] that are commonly used to investigate void-induced damage at large plastic strains in the literature. In the original Gurson model [1], plastic flow was analyzed using spherical micro-voids with a single-void fraction parameter, and the matrix material was assumed to obey the von Mises yield criterion. This model was consequently modified by Tvergaard [2,3] and by Needleman and Tvergaard [4,5] by introducing additional damage parameters. In this modified model, which is currently referred to as the GTN model, the damage-induced plastic instability (or necking) process is governed by the growth of existing voids, nucleation of new voids during deformation, and micro-crack coalescence in the neck region. The GTN model is widely used in analyzing many different plastic deformation processes [6-20]. Matrix material has been frequently identified in recent years as anisotropic, and micro-voids of non-spherical shapes in different orientations exist within the anisotropic matrix. Several approximate yield criteria, such as quadratic and non-quadratic yield criteria by Hill [21, 22], Hosford [23], and Barlat and Lian [24], for anisotropic ductile materials are available in literature. Numerical implementations and subsequent studies of the combination of earlier GTN model with some of the newer yield

criteria can be found in references [10-19, 25-34]. Furthermore, the GTN model has been extended and transformed from an isotropic matrix material to an anisotropic matrix [6, 8, 9] based on the algorithm presented by N. Aravas [35]. Hill's quadratic anisotropic yield criterion is used in these studies to define equivalent stress, whereas the exact algorithm for an isotropic material is applied in the new anisotropic implementations of the GTN model. In 1987, Aravas [35] presented a distinct numerical implementation of the isotropic GTN model into ABAQUS-Standard finite element (FE) code, where both three-dimensional and plane stress cases were considered. The algorithm was integrated implicitly, and the tangent moduli were obtained by consistent linearization of elastoplastic constitutive equations.

In this study, the extension of isotropic GTN algorithm presented by Aravas [35] to anisotropic metals based on Hill's quadratic anisotropy theory is analyzed. The extension of isotropic GTN model cannot predict the stress–strain curve accurately because of substantial damage growth when individual Hill's constants are considered. Therefore, an approximate model that replaces individual Hill's constants with effective anisotropic coefficient is proposed to predict the stress–strain curve of metals. The effects of individual Hill's constants are removed, but the substantial damage growth is neglected without changing the equivalent stress in anisotropic model. Spherical and ellipsoidal micro-voids for 3D and plane stress cases are considered, and model implementation of each case is illustrated. Swift law is used to describe the stress–strain curve of matrix material. The anisotropic GTN model is implemented to ABAQUS-Standard FE code, and various

analyses of uniaxial stress–strain response with different material property parameters are compared with previous experimental data for an AA6016 aluminum sheet.

3.2. Stress and strain measures

For clarity, several equations from [35, 36] are reproduced in this section to explain how ABAQUS deals with plasticity responses. The macroscopic Cauchy stress tensor and its Jaumann rate are used in ABAQUS to formulate the constitutive equations as follows.

$$\boldsymbol{\sigma} = \sigma_{ij} e_i e_j \tag{1}$$

$$\dot{\boldsymbol{\sigma}} = \dot{\sigma}_{ij} e_i e_j \tag{2}$$

where, e_k are the basic vectors of the Cartesian coordinate system. Also, the macroscopic velocity gradient to measure an objective strain is [36]:

$$\boldsymbol{L} = V_{i,j} e_i e_j \tag{3}$$

where, $V_{i,j}$ is the velocity components. The strain rate is derived based on the following equation [36]:

$$\dot{\boldsymbol{\varepsilon}} = \frac{1}{2}\left(V_{i,j} + V_{j,i}\right) \tag{4}$$

in which the elastic and plastic components of strain rates are decomposed as follows [35, 36]:

$$\dot{\boldsymbol{\varepsilon}} = \dot{\boldsymbol{\varepsilon}}^{el} + \dot{\boldsymbol{\varepsilon}}^{pl} \tag{5}$$

Thus, the strain increments are described as [35, 36]:

$$d\boldsymbol{\varepsilon} = d\boldsymbol{\varepsilon}^{el} + d\boldsymbol{\varepsilon}^{pl} \tag{6}$$

The stress tensor can be written in terms of elastic strain energy potential $W = W(\boldsymbol{\varepsilon}^{\boldsymbol{el}})$ as:

$$\boldsymbol{\sigma} = \frac{\partial W}{\partial \boldsymbol{\varepsilon}^{el}} \tag{7}$$

Also, for linear elasticity [35, 36]:

$$\boldsymbol{\sigma} = \boldsymbol{C}^{el} : \boldsymbol{\varepsilon}^{el} \tag{8}$$

where $\boldsymbol{C}^{el}$ is the fourth order elasticity tensor given as [35, 36]:

$$C_{ijkl}^{el} = 2G\delta_{ik}\,\delta_{jl} + \left(K - \frac{2}{3}G\right)\delta_{ij}\,\delta_{kl} \tag{9}$$

where δ_{ij} is kronecker delta and the symbols *K* and *G* represent isotropic bulk and shear moduli, respectively.

In this paper, the double dot is used to indicate the following product and boldface symbol denote tensor.

$$\boldsymbol{A} : \boldsymbol{B} = A_{ij}B_{ij}$$

3.3. Hill's quadratic anisotropic yield criterion

Equivalent stress (q) for Hill's quadratic anisotropic yield criterion for matrix material is expressed as:

$$q = \sqrt{\frac{3}{2}S_{ij}H_{ijkl}S_{kl}} \tag{10}$$

where S_{ij} and S_{kl} are the deviatoric stress tensors and H_{ijkl} (H with subscript) is the forth order anisotropy Hill's tensor that has the following form:

$$H_{ijkl} = \begin{bmatrix} H_{1111} & 0 & 0 & 0 & 0 & 0 \\ 0 & H_{2222} & 0 & 0 & 0 & 0 \\ 0 & 0 & H_{3333} & 0 & 0 & 0 \\ 0 & 0 & 0 & H_{2323} & 0 & 0 \\ 0 & 0 & 0 & 0 & H_{3131} & 0 \\ 0 & 0 & 0 & 0 & 0 & H_{1212} \end{bmatrix} \tag{11}$$

So, Equation (10) can be rewritten as:

$$q = \sqrt{\frac{3}{2} S_{ij} H_{ijij} S_{ij}} \tag{12}$$

Equivalent stress in Equation (12) can be written in the expanded form as:

$$q^2 = \frac{3}{2}(H_{1111}S_{11}^2 + H_{2222}S_{22}^2 + H_{3333}S_{33}^2 + 2H_{2323}S_{23}^2 + 2H_{3131}S_{31}^2 + 2H_{1212}S_{12}^2) \tag{13}$$

It is to be noted that equivalent stress in Equation (13) is in terms of deviatoric stress components. It can also be expressed in terms of stresses as:

$$q^2 = F(\sigma_{22} - \sigma_{33})^2 + G(\sigma_{33} - \sigma_{11})^2 + H(\sigma_{11} - \sigma_{22})^2 + 2L\sigma_{23}^2 + 2M\sigma_{31}^2 + 2N\sigma_{12}^2 \tag{14}$$

where F, G, H, L, M and N are anisotropy constants that can be correlated to $H_{1111}, H_{2222}, H_{3333}, H_{2323}, H_{3131}$ and H_{1212}. Generally, for sheet materials, constants F, G, H, L, M and N can be obtained by three experimental planar tensile tests along 0^o, 45^o and 90^o orientations with respect to sheet rolling direction in the following form:

$$F = \frac{R_0}{R_{90}(1+R_0)} \tag{15-a}$$

$$G = \frac{1}{1+R_0} \tag{15-b}$$

$$H = \frac{R_0}{1+R_0} \tag{15-c}$$

$$M = N = L = \frac{(R_{90}+R_0)(1+2R_{45})}{2R_{90}(1+R_0)} \tag{15-d}$$

where, R_0, R_{45} and R_{90} are the plastic anisotropic parameters along $0^o, 45^o$ and 90^o directions. It is to be noted that $G + H = 1$. The relationship between F, G, H, L, M and N and $H_{1111}, H_{2222}, H_{3333}, H_{2323}, H_{3131}$ and H_{1212} can be expressed as:

$$H_{1111} = \frac{2}{3}(2G + 2H - F) \tag{16-a}$$

$$H_{2222} = \frac{2}{3}(2F + 2H - G) \tag{16-b}$$

$$H_{3333} = \frac{2}{3}(2F + 2G - H) \tag{16-c}$$

$$H_{2323} = \frac{2}{3}L \tag{16-d}$$

$$H_{3131} = \frac{2}{3}M \tag{16-e}$$

$$H_{1212} = \frac{2}{3}N \tag{16-f}$$

The relationship between Hill's anisotropy constants and R_0, R_{45}, R_{90} can be found by substituting Equations (15) into (16).

3.4. Elastoplastic constitutive equations

A yield function that involves the hydrostatic pressure $\left(p = -\frac{1}{3}\boldsymbol{\sigma}:\boldsymbol{I};\ \boldsymbol{I} \text{ is the second order identity tensor}\right)$, equivalent stress q and internal state variables H^{α} (H with superscript) is expressed in the following general form:

$$\Phi(p, q, H^{\alpha}) = 0 \tag{17}$$

where H^{α} are a set of internal state variables, $\alpha = 1,2, \ldots\ldots, n$. Based on associative flow rule, we have:

$$d\boldsymbol{\varepsilon}^{pl} = d\lambda \frac{\partial g}{\partial \boldsymbol{\sigma}} = d\lambda \left(-\frac{1}{3}\frac{\partial g}{\partial p}\boldsymbol{I} + \frac{\partial g}{\partial q}\boldsymbol{N}\right) \tag{18}$$

where $d\lambda$ is a positive scalar parameter and $g(p, q, H^{\alpha})$ is the flow potential. Also,

$$\boldsymbol{N} = \frac{\partial q}{\partial \boldsymbol{\sigma}} = \frac{3}{2q}\acute{\boldsymbol{S}} \tag{19}$$

where, $\acute{S}_{ij} = H_{ijij}S_{ij}$ when there is no sum on i and j.

By defining $\Delta\varepsilon_P = -\Delta\lambda \frac{\partial g}{\partial p}$ and $\Delta\varepsilon_q = \Delta\lambda \frac{\partial g}{\partial q}$, Equation (18) leads to:

$$\Delta\boldsymbol{\varepsilon}^{pl} = \frac{1}{3}\Delta\varepsilon_p\boldsymbol{I} + \Delta\varepsilon_q\boldsymbol{N} \tag{20}$$

Further, on eliminating $\Delta\lambda$ in Equation (18), one obtains:

$$\Delta\varepsilon_p \frac{\partial g}{\partial q} + \Delta\varepsilon_q \frac{\partial g}{\partial p} = 0 \tag{21}$$

The stress tensor can be written in the following form:

$$\boldsymbol{\sigma} = -p\boldsymbol{I} + \frac{2}{3}q\acute{\boldsymbol{N}} \tag{22}$$

where, $\acute{N}_{ij} = \frac{N_{ij}}{H_{ijij}}$ when there is no sum on i and j.

Lastly, a homogeneous function of $\bar{h}^{\alpha}$can be defined to describe the evolution of the state variables with continuing plastic strain increment as follows:

$$\Delta H^{\alpha} = \bar{h}^{\alpha}\left(\Delta\bar{\varepsilon}^{pl}, \boldsymbol{\sigma}, H^{\beta}\right) \tag{23}$$

3.5. Integration algorithm for elastoplastic constitutive relations

In FE analysis, the increment rate is calculated with the knowledge of the known values at the integration points at the start of each increment to integrate the constitutive laws. In this analysis, Euler's implicit integration procedure is used for numerical integration where ${}^{t+\Delta t}f$ is the value of f at $t + \Delta t$ which can be approximated as:

$${}^{t+\Delta t}f = {}^{t}f + {}^{t+\Delta t}\dot{f}\Delta t \tag{24}$$

where $${}^{t+\Delta t}\dot{f}\Delta t = \Delta f$$

In Equation (24), ${}^{t}f$ is the value of f at t. In this paper, only the superscript t is used and if a symbol does not have a superscript, it means that it corresponds to the value at $t + \Delta t$. In this section, the tensors are presented with indices to clarify the content.

3.5.1. 3-D case

Stress state at the end of time increment based on known value for total strain can be written as:

$$\sigma_{ij} = C^{el}_{ijkl}\varepsilon^{el}_{kl} = C^{el}_{ijkl}\left({}^{t}\varepsilon^{el}_{kl} + \Delta\varepsilon_{kl} - \Delta\varepsilon^{pl}_{kl}\right) \tag{25}$$

Elastic predictor stress tensor is given by:

$$\sigma^{el}_{ij} = C^{el}_{ijkl}\left({}^{t}\varepsilon^{el}_{kl} + \Delta\varepsilon_{kl}\right) \tag{26}$$

Therefore, $$\sigma_{ij} = \sigma^{el}_{ij} - C^{el}_{ijkl}\Delta\varepsilon^{pl}_{kl} \tag{27}$$

On substituting Equation (20) into (27), one obtains:

$$\sigma_{ij} = \sigma^{el}_{ij} - K\Delta\varepsilon_p\delta_{ij} - 2G\Delta\varepsilon_q N_{ij} \tag{28-a}$$

$$\sigma_{ij} = \sigma^{el}_{ij} - K\Delta\varepsilon_p\delta_{ij} - \frac{3G\Delta\varepsilon_q}{q}\acute{S}_{ij} \tag{28-b}$$

Deviatoric stress based on Equations (28) can be written as:

$$S_{ij} = S^{el}_{ij} - \frac{3G\Delta\varepsilon_q}{q}\left(\acute{S}_{ij} - \frac{\acute{S}_{kk}}{3}\delta_{ij}\right) \tag{29}$$

Equation (29) leads to the following equation:

$$S_{ij} = \bar{S}^{el}_{ij} + \frac{G\Delta\varepsilon_q}{q}\hat{S}_{ij} \tag{30}$$

where, $\bar{S}^{el}_{ij} = \lambda_{ij}S^{el}_{ij}$ and $\hat{S}_{ij} = \lambda_{ij}\acute{S}_{ij}\delta_{ij}$ when there is no sum on i and j and $\lambda_{ij} = \frac{1}{1+\frac{3G\Delta\varepsilon_q H_{ijij}}{q}}$.

The deviatoric stress tensor using Equation (30) can be expressed as:

$$S_{ij} = \bar{S}_{ij}^{el} + \frac{G\Delta\varepsilon_q}{q}\left(\frac{H_{kkkk}\bar{S}_{kk}^{el}}{1-\frac{G\Delta\varepsilon_q}{q}(H_{kkkk}\lambda_{kk})}\right)\acute{\lambda}_{ij} \tag{31}$$

where, $\acute{\lambda}_{ij} = \lambda_{ij}\delta_{ij}$ when there is no sum on i and j.

On expanding Equation (31), the deviatoric stresses are:

$$S_{11} = \lambda_{11}S_{11}^{el} + \frac{G\Delta\varepsilon_q}{q}\lambda_{11}\left(\frac{H_{1111}\lambda_{11}S_{11}^{el} + H_{2222}\lambda_{22}S_{22}^{el} + H_{3333}\lambda_{33}S_{33}^{el}}{1-\frac{G\Delta\varepsilon_q}{q}(H_{1111}\lambda_{11} + H_{2222}\lambda_{22} + H_{3333}\lambda_{33})}\right)$$

$$S_{22} = \lambda_{22}S_{22}^{el} + \frac{G\Delta\varepsilon_q}{q}\lambda_{22}\left(\frac{H_{1111}\lambda_{11}S_{11}^{el} + H_{2222}\lambda_{22}S_{22}^{el} + H_{3333}\lambda_{33}S_{33}^{el}}{1-\frac{G\Delta\varepsilon_q}{q}(H_{1111}\lambda_{11} + H_{2222}\lambda_{22} + H_{3333}\lambda_{33})}\right)$$

$$S_{33} = \lambda_{33}S_{33}^{el} + \frac{G\Delta\varepsilon_q}{q}\lambda_{33}\left(\frac{H_{1111}\lambda_{11}S_{11}^{el} + H_{2222}\lambda_{22}S_{22}^{el} + H_{3333}\lambda_{33}S_{33}^{el}}{1-\frac{G\Delta\varepsilon_q}{q}(H_{1111}\lambda_{11} + H_{2222}\lambda_{22} + H_{3333}\lambda_{33})}\right)$$

$$S_{12} = \lambda_{12}S_{12}^{el}$$

$$S_{13} = \lambda_{13}S_{13}^{el}$$

$$S_{23} = \lambda_{23}S_{23}^{el}$$

New values for deviatoric stresses based on deviatoric elastic predictor stresses can be found from Equations (31), and consequently the values of N_{ij} can be obtained from Equation (19). However, in contrast to the isotropic case, λ_{ij} components are different from each other in the anisotropic case, and the relationship $q - q^{el}$ cannot be obtained

directly. As a result, the scalar relationship of $q - q^{el}$ in the anisotropic case can be obtained by assuming a scalar value of $\bar{\lambda}$. All λ_{ij} components are considered equal to $\bar{\lambda}$ ($\lambda_{ij} = \bar{\lambda}$). In fact, $\bar{\lambda}$ is the effective value for all λ_{ij} components.

As a result, $\bar{\lambda}$ is considered for all λ_{ij} components to relate the deviatoric total and deviatoric elastic predictor stresses in Equation (32) to obtain the scalar value of $q - q^{el}$ relationship.

$$S_{ij} = \bar{\lambda}\, S_{ij}^{el} \tag{32-a}$$

$$\bar{\lambda} = \frac{1}{1+\frac{3G\Delta\varepsilon_q \bar{H}}{q}} \tag{32-b}$$

In order to obtain effective anisotropy coefficient $(\bar{H})$ for H_{ij} components, Equation (33) is used to relate deviatoric total and deviatoric elastic predictor stresses. The expression for $\bar{H}$ can be written as:

$$\bar{H} = \left(\frac{\sqrt{\frac{3}{2} S_{ij}^{el} H_{ijij} S_{ij}^{el}}}{\sqrt{\frac{3}{2} S_{ij}^{el} S_{ij}^{el}}} \right)^2 = \left(\frac{q^{el}}{q_{iso}^{el}} \right)^2 \tag{33-a}$$

where $$\sqrt{\frac{3}{2} S_{ij}^{el} H_{ijij} S_{ij}^{el}} = \sqrt{\frac{3}{2} S_{ij}^{el} \bar{H}_{ijij} S_{ij}^{el}} = q^{el} \tag{33-b}$$

and $$\boldsymbol{\bar{H}} = \begin{bmatrix} \bar{H} & 0 & 0 & 0 & 0 & 0 \\ 0 & \bar{H} & 0 & 0 & 0 & 0 \\ 0 & 0 & \bar{H} & 0 & 0 & 0 \\ 0 & 0 & 0 & \bar{H} & 0 & 0 \\ 0 & 0 & 0 & 0 & \bar{H} & 0 \\ 0 & 0 & 0 & 0 & 0 & \bar{H} \end{bmatrix}$$

The expression for q_{iso}^{el} is:

$$q_{iso}^{el} = \sqrt{\frac{3}{2} S_{ij}^{el} S_{ij}^{el}} \tag{33-c}$$

where $H_{ij} = 1.0$ for an isotropic material.

The difference between q and q^{el} can be obtained by considering the effective values of $\bar{H}$ and $\bar{\lambda}$ as follows:

$$q - q^{el} = \sqrt{\frac{3}{2} S_{ij} H_{ijij} S_{ij}} - \sqrt{\frac{3}{2} S_{ij}^{el} H_{ijij} S_{ij}^{el}} \tag{34-a}$$

or $$q - q^{el} = \sqrt{\frac{3}{2} S_{ij} H_{ijij} S_{ij}} - \sqrt{\frac{3}{2} S_{ij}^{el} \bar{H}_{ijij} S_{ij}^{el}} \tag{34-b}$$

or $$q - q^{el} = \sqrt{\frac{3}{2} S_{ij} H_{ijij} S_{ij}} - \frac{1}{\bar{\lambda}} \sqrt{\frac{3}{2} S_{ij} \bar{H}_{ijij} S_{ij}} \tag{34-c}$$

where $$q = \sqrt{\frac{3}{2} S_{ij} \bar{H}_{ijij} S_{ij}} = \sqrt{\frac{3}{2} S_{ij} H_{ijij} S_{ij}}$$

or $$q - q^{el} = \left(1 - \frac{1}{\bar{\lambda}}\right) q = \left(1 - 1 - \frac{3G\Delta\varepsilon_q \bar{H}}{q}\right) q \tag{34-d}$$

Equation (34) thus yields: $$q = q^{el} - 3G\Delta\varepsilon_q \bar{H} \tag{35}$$

Since $\bar{H} = 1$ for an isotropic material, one obtains,

$$q = q^{el} - 3G\Delta\varepsilon_q$$

Again, $\bar{\lambda}$ and $\bar{H}$ are calculated and considered for all λ_{ij} and H_{ijij} components, respectively, to provide the same value for q^{el} when H_{ijij} components are considered. The only reason why we consider $\bar{H}$ for all H_{ijij} components is because of the need to

determine the relationship between the scalar values of q and q^{el}. In reality, identifying the mentioned relationship if H_{ijij} components are considered for q^{el} is quite impossible.

The relationship between p and p^{el} is now expressed as:

$$p = p^{el} + K\Delta\varepsilon_p \tag{36}$$

Therefore, the problem of integration of elastoplastic equations reduces to the solution of the following set of non-linear equations:

$$\Delta\varepsilon_p \frac{\partial g}{\partial q} + \Delta\varepsilon_q \frac{\partial g}{\partial p} = 0 \tag{21}$$

$$\Phi\left(p, q, H^{\beta}\right) = 0 \tag{17}$$

$$p = p^{el} + K\Delta\varepsilon_p \tag{36}$$

$$q = q^{el} - 3G\Delta\varepsilon_q \overline{H} \tag{35}$$

$$\Delta H^{\alpha} = h^{\alpha}\left(\Delta\varepsilon_p, \Delta\varepsilon_q, p, q, H^{\beta}\right) \tag{37}$$

The above set of equations is solved using Newton-Raphson method which is based on Taylor-series expansions. The application of Taylor-series-method to F_i is:

$$F_i + \frac{\partial F_i}{\partial \Delta\varepsilon_p} d\Delta\varepsilon_p + \frac{\partial F_i}{\partial \Delta\varepsilon_q} d\Delta\varepsilon_q + \frac{\partial F_i}{\partial H^{\alpha}} dH^{\alpha} = 0 \tag{38}$$

where $$F_1 = \Delta\varepsilon_p \frac{\partial g}{\partial q} + \Delta\varepsilon_q \frac{\partial g}{\partial p} \text{ and } F_2 = \Phi$$

By considering $d\Delta\varepsilon_p = c_p$, $d\Delta\varepsilon_q = c_q$, and the above expressions for F_1 and F_2, Equation (38) yields:

$$A_{11}c_p + A_{12}c_q = b_1 \tag{39-a}$$

$$A_{21}c_p + A_{22}c_q = b_2 \tag{39-b}$$

where constants A_{ij} and b_i are presented in Appendix I. The incremental strains c_p and c_q are obtained by solving Equations (39) and then updating the values of $\Delta\varepsilon_p$ and $\Delta\varepsilon_q$ as follows:

$$\Delta\varepsilon_p \longleftarrow \Delta\varepsilon_p + c_p \tag{40-a}$$

$$\Delta\varepsilon_q \longleftarrow \Delta\varepsilon_q + c_Q \tag{40-b}$$

3.5.2. Plane stress case

For the case of plane stress, as mentioned in [35], the out-of-plane strain components are not defined kinematically. Consequently, some modifications for this case are required. The elasticity equations are written as:

$$p = -K\left({}^{t}\varepsilon_{kk}^{el} + \Delta\varepsilon_{kk}^{el} \right) \tag{41}$$

In Equation (41), superscript (t) defines the current time. As previously mentioned, the superscript $t + \Delta t$ has been dropped in the revised manuscript. Thus, all quantities without superscript belong to $t + \Delta t$. Also,

$$S_{ij} = 2G\left({}^{t}e_{ij}^{el} + \Delta e_{ij}^{el} \right) \tag{42}$$

where e_{ij}^{el} and Δe_{ij}^{el} are deviatoric parts of ε_{ij}^{el} and $\Delta\varepsilon_{ij}^{el}$, respectively. Now, following [35], a rectangular co-ordinate system with in-plane stresses in x_1, x_2 plane are considered. Also,

strain increments, $\Delta\varepsilon_{11}$, $\Delta\varepsilon_{22}$ and $\Delta\varepsilon_{12}$ are known, and $\Delta\varepsilon_3$ is the normal component of strain increment. Therefore, out-of-plane strain component is expressed as:

$$\boldsymbol{\Delta\varepsilon} = \boldsymbol{\Delta\bar{\varepsilon}} + \Delta\varepsilon_3\boldsymbol{a} \tag{43}$$

where $$\boldsymbol{\Delta\bar{\varepsilon}} = \Delta\varepsilon_{11}\boldsymbol{e_1e_1} + \Delta\varepsilon_{22}\boldsymbol{e_2e_2} + \Delta\varepsilon_{12}(\boldsymbol{e_1e_2} + \boldsymbol{e_2e_1})$$

and $$\boldsymbol{a} = \boldsymbol{e_3e_3}$$

here, $e_i, i = 1, 2, \text{and } 3$ are unit vectors along the co-ordinate axes. The hydrostatic pressure p and deviatoric stress tensor S_{ij} are expressed as:

$$p = p^{el} - K\left(\Delta\varepsilon_3 - \Delta\varepsilon_p\right) \tag{44}$$

$$\boldsymbol{S} = \boldsymbol{S^{el}} + 2G\left(\Delta\varepsilon_3\acute{\boldsymbol{a}} - \frac{3}{2}\frac{\Delta\varepsilon_q}{q}\left(\acute{\boldsymbol{S}} - \frac{\acute{\boldsymbol{S}}}{3}\boldsymbol{I}\right)\right) \tag{45}$$

where, $\acute{\boldsymbol{a}}$ is the deviatoric part of $\boldsymbol{a}$. Lastly, q can be expressed as:

$$q = -3G\Delta\varepsilon_q\bar{H} + \sqrt{{q^{el}}^2 + 4H_{3333}G^2{\Delta\varepsilon_3}^2 + 6GH_{3333}S_{33}^{el}\Delta\varepsilon_3} \tag{46}$$

Since stress in normal direction is zero, unknown $\Delta\varepsilon_3$ can be determined from the following constraint:

$$\sigma_{33} = S_{33} - p = 0 \tag{47}$$

where S_{33} is given by:

$$S_{33} = S_{33}^{el} + \frac{4}{3}G\Delta\varepsilon_3 - \frac{3G\Delta\varepsilon_q\bar{H}}{q}S_{33} \tag{48}$$

By substituting Equation (47) into Equation (48), one obtains:

$$\left(q + 3G\Delta\varepsilon_q\bar{H}\right)p - \left(S_{33}^{el} + \frac{4}{3}G\Delta\varepsilon_3\right)q = 0 \tag{49}$$

Therefore, derivative of q with respect to $\Delta\varepsilon_3$ can be written as:

$$\frac{\partial q}{\partial \Delta\varepsilon_3} = \frac{3GH_{3333}S_{33}^{el} + 4G^2H_{3333}\Delta\varepsilon_3}{q + 3G\Delta\varepsilon_q\bar{H}} \tag{50}$$

Summarizing the backward Euler method as applied to elastoplastic equations, anisotropic materials included, one has the following set of the equations:

$$\Delta\varepsilon_p\frac{\partial g}{\partial q} + \Delta\varepsilon_q\frac{\partial g}{\partial p} = 0 \tag{21}$$

$$\Phi(p, q, H^\alpha) = 0 \tag{17}$$

$$\left(q + 3G\Delta\varepsilon_q\bar{H}\right)p - \left(S_{33}^{el} + \frac{4}{3}G\Delta\varepsilon_3\right)q = 0 \tag{49}$$

$$p = p^{el} - K\left(\Delta\varepsilon_3 - \Delta\varepsilon_p\right) \tag{44}$$

$$q = -3G\Delta\varepsilon_q\bar{H} + \sqrt{{q^{el}}^2 + 6GH_{3333}S_{33}^{el}\Delta\varepsilon_3 + 4G^2H_{3333}{\Delta\varepsilon_3}^2} \tag{46}$$

$$\Delta H^\alpha = h^\alpha\left(\Delta\varepsilon_p, \Delta\varepsilon_q, p, q, H^\beta\right) \tag{37}$$

The application of Taylor-series-method to F_i for plane stress case is:

$$F_i + \frac{\partial F_i}{\partial \Delta\varepsilon_p}d\Delta\varepsilon_p + \frac{\partial F_i}{\partial \Delta\varepsilon_q}d\Delta\varepsilon_q + \frac{\partial F_i}{\partial \Delta\varepsilon_3}d\Delta\varepsilon_3 + \frac{\partial F_i}{\partial H^\alpha}dH^\alpha = 0 \tag{51}$$

Expressing, $d\Delta\varepsilon_p = c_p$, $d\Delta\varepsilon_q = c_q$, $d\Delta\varepsilon_3 = c_3$, $F_1 = \Delta\varepsilon_p\frac{\partial g}{\partial q} + \Delta\varepsilon_q\frac{\partial g}{\partial p}$, $F_2 = \Phi$ and $F_3 = \left(q + 3G\Delta\varepsilon_q\bar{H}\right)p - \left(S_{33}^{el} + \frac{4}{3}G\Delta\varepsilon_3\right)q$, following set of equations is obtained:

$$A_{11}c_p + A_{12}c_q + A_{13}c_3 = b_1 \tag{52}$$

$$A_{21}c_p + A_{22}c_q + A_{23}c_3 = b_2 \tag{53}$$

$$A_{31}c_p + A_{32}c_q + A_{33}c_3 = b_3 \tag{54}$$

where, constants $A_{11}, A_{12}, A_{21}, A_{22}, b_1$ and b_2 are defined in Appendix I, and $A_{13}, A_{23}, A_{31}, A_{32}$ and b_3 in Appendix II. The quantities c_p, c_q and c_3 are obtained by solving Equations (52), (53) and (54), and then the values of $\Delta\varepsilon_p$, $\Delta\varepsilon_q$ and $\Delta\varepsilon_3$ are updated as follows:

$$\Delta\varepsilon_p \longleftarrow \Delta\varepsilon_p + c_p \tag{55-a}$$

$$\Delta\varepsilon_q \longleftarrow \Delta\varepsilon_q + c_q \tag{55-b}$$

$$\Delta\varepsilon_3 \longleftarrow \Delta\varepsilon_3 + c_3 \tag{55-c}$$

3.6. Stress updates

After updating $\Delta\varepsilon_p$, $\Delta\varepsilon_q$, p and q, new stress values from Equation (22) are:

$$\boldsymbol{\sigma} = -p\boldsymbol{I} + \frac{2}{3}q\acute{\boldsymbol{N}} \tag{22}$$

and

$$\boldsymbol{\sigma^{el}} = -p^{el}\boldsymbol{I} + \frac{2}{3}q^{el}\bar{\boldsymbol{N}}^{\boldsymbol{el}} \tag{56}$$

where $\bar{N}_{ij}^{el} = \frac{N_{ij}^{el}}{H_{ijij}}$ and $N_{ij}^{el} = \frac{3}{2q^{el}}\bar{S}_{ij}^{el}$ when there is no sum on i and j.

Equations (22) and (56) yield:

$$\boldsymbol{\sigma} = \boldsymbol{\sigma^{el}} - (p - p^{el})\boldsymbol{I} - \frac{2}{3}q^{el}\bar{\boldsymbol{N}}^{\boldsymbol{el}} + \frac{2}{3}q\acute{\boldsymbol{N}} \tag{57}$$

with $$p - p^{el} = -K\left(\Delta\varepsilon_3 - \Delta\varepsilon_p\right)$$

and $$q = -3G\Delta\varepsilon_q\bar{H} + \sqrt{{q^{el}}^2 + 6GH_{3333}S_{33}^{el}\Delta\varepsilon_3 + 4G^2{H_{3333}\Delta\varepsilon_3}^2}$$

In the general 3-D implementation, $\Delta\varepsilon_3$ is automatically zero and one obtains:

$$p = K\Delta\varepsilon_p + p^{el}$$

$$q = -3G\Delta\varepsilon_q\bar{H} + q^{el}$$

Also, it should be mentioned that in the isotropic case, when $H_{ij} = 1$, $N_{ij} = N_{ij}^{el}$. However, in the case of anisotropy, $N_{ij} \neq N_{ij}^{el}$ and this will affect the values of new stresses.

3.7. Linearization of moduli

Equilibrium equations in an implicit FE code are defined at the end of each increment. The linearized moduli (D), or so-called Jacobian matrix, defines the variation in stress at $t + \Delta t$ caused by variation of the total strain at $t + \Delta t$ as:

$$\boldsymbol{D} = \left(\frac{\partial\boldsymbol{\sigma}}{\partial\boldsymbol{\varepsilon}}\right)_{t+\Delta t} \tag{58}$$

The Jacobian matrix for both three-dimensional and plane stress cases are derived below.

3.7.1. Jacobian matrix in 3-D

Starting with elasticity Equation (28-a), one obtains:

$$\boldsymbol{\sigma} = \boldsymbol{C}^{el}\colon\left(\boldsymbol{\varepsilon} - {}^{t}\boldsymbol{\varepsilon}^{pl} - \frac{1}{3}\Delta\varepsilon_p\boldsymbol{I} - \Delta\varepsilon_q\boldsymbol{N}\right) \tag{59}$$

and

$$\partial\boldsymbol{\sigma} = \boldsymbol{C}^{el}\colon\left(\partial\boldsymbol{\varepsilon} - \frac{1}{3}\partial\Delta\varepsilon_p\boldsymbol{I} - \partial\Delta\varepsilon_q\boldsymbol{N} - \Delta\varepsilon_q\frac{\partial\boldsymbol{N}}{\partial\boldsymbol{\sigma}}\colon\partial\boldsymbol{\sigma}\right) \tag{60}$$

where,

$$\frac{\partial\boldsymbol{N}}{\partial\boldsymbol{\sigma}} = \frac{1}{q}\left(\frac{3}{2}\boldsymbol{H} - \frac{\widehat{\boldsymbol{H}}}{2} - \boldsymbol{N}\boldsymbol{N}\right) \tag{61}$$

where, $\widehat{H}_{ijkl} = \begin{bmatrix} H_{1111} & 0 & 0 & 0 & 0 & 0 \\ 0 & H_{2222} & 0 & 0 & 0 & 0 \\ 0 & 0 & H_{3333} & 0 & 0 & 0 \\ 0 & 0 & 0 & & 0 & 0 \\ 0 & 0 & 0 & & 0 & 0 \\ 0 & 0 & 0 & & 0 & 0 \end{bmatrix}$.

By using Equation (21), the variations $\partial\Delta\varepsilon_p$ and $\partial\Delta\varepsilon_q$ in terms of $\partial\sigma$ can be expressed as follows:

$$\partial\left(\Delta\varepsilon_p\frac{\partial g}{\partial q}\right) + \partial\left(\Delta\varepsilon_q\frac{\partial g}{\partial p}\right) = 0 \tag{62-a}$$

$$\partial\Delta\varepsilon_p\frac{\partial g}{\partial q} + \Delta\varepsilon_p\left(\left(\frac{\partial^2 g}{\partial q\partial p}\frac{\partial p}{\partial\boldsymbol{\sigma}} + \frac{\partial^2 g}{\partial q^2}\frac{\partial q}{\partial\boldsymbol{\sigma}}\right)\colon\partial\boldsymbol{\sigma} + \sum_{\alpha=1}^{n}\left\{\frac{\partial^2 g}{\partial q\partial H^\alpha}\partial H^\alpha\right\}\right) + \partial\Delta\varepsilon_q\frac{\partial g}{\partial p} +$$

$$\Delta\varepsilon_q\left(\left(\frac{\partial^2 g}{\partial p^2}\frac{\partial p}{\partial\boldsymbol{\sigma}} + \frac{\partial^2 g}{\partial q\partial p}\frac{\partial q}{\partial\boldsymbol{\sigma}}\right)\colon\partial\boldsymbol{\sigma} + \sum_{\alpha=1}^{n}\left\{\frac{\partial^2 g}{\partial p\partial H^\alpha}\partial H^\alpha\right\}\right) = 0 \tag{62-b}$$

Also, from Equation (17), we have:

$$\left(\frac{\partial \Phi}{\partial p}\frac{\partial p}{\partial \boldsymbol{\sigma}} + \frac{\partial \Phi}{\partial q}\frac{\partial q}{\partial \boldsymbol{\sigma}}\right) : \partial \boldsymbol{\sigma} + \sum_{\alpha=1}^{n}\left\{\frac{\partial \Phi}{\partial H^{\alpha}}\partial H^{\alpha}\right\} = 0 \tag{63}$$

where, $\frac{\partial p}{\partial \boldsymbol{\sigma}} = -\frac{1}{3}\boldsymbol{I}$ and $\frac{\partial q}{\partial \boldsymbol{\sigma}} = \boldsymbol{N}$.

The resulting equations, as shown in Appendix III, are:

$$A_{11}\partial \Delta \varepsilon_p + A_{12}\partial \Delta \varepsilon_q = (B_{11}\boldsymbol{I} + B_{12}\boldsymbol{N}) : \partial \boldsymbol{\sigma} \tag{64}$$

$$A_{21}\partial \Delta \varepsilon_p + A_{22}\partial \Delta \varepsilon_q = (B_{21}I + B_{22}\boldsymbol{N}) : \partial \boldsymbol{\sigma} \tag{65}$$

Equations (64) and (65) are solved for $\partial \Delta \varepsilon_p$ and $\partial \Delta \varepsilon_q$ as follows:

$$(66)\partial \Delta \varepsilon_p = \left(m_{pi}I + m_{pn}N\right) : \partial \boldsymbol{\sigma}$$

$$(67)\partial \Delta \varepsilon_q = \left(m_{qi}I + m_{qn}N\right) : \partial \boldsymbol{\sigma}$$

where
$$\begin{bmatrix} m_{pi} & m_{pn} \\ m_{qi} & m_{qn} \end{bmatrix} = \begin{bmatrix} A_{11} & A_{12} \\ A_{21} & A_{22} \end{bmatrix}^{-1} \begin{bmatrix} B_{11} & B_{12} \\ B_{21} & B_{22} \end{bmatrix} \tag{68}$$

Substituting Equations (66) and (67) into (60), one obtains:

$$(69)(\boldsymbol{J} + \boldsymbol{C}^{el} : M) : \partial \boldsymbol{\sigma} = \boldsymbol{C}^{el} : \partial \boldsymbol{\varepsilon}$$

where,

$$\boldsymbol{M} = \frac{1}{3}m_{pi}\boldsymbol{II} + \frac{1}{3}m_{pn}\boldsymbol{IN} + m_{qi}\boldsymbol{NI} + m_{qn}\boldsymbol{NN} + \Delta \varepsilon_Q \frac{\partial \boldsymbol{N}}{\partial \boldsymbol{\sigma}} \tag{70}$$

By using Equation (70), the material matrix is found to be:

$$\boldsymbol{D} = \left(\frac{\partial \boldsymbol{\sigma}}{\partial \boldsymbol{\varepsilon}}\right)_{t+\Delta t} = (\boldsymbol{J} + \boldsymbol{C}^{el} : M)^{-1} : \boldsymbol{C}^{el}$$

(71)

which can be written as:

$$\boldsymbol{D} = \left(M + \boldsymbol{C}^{el^{-1}}\right)^{-1} \tag{72}$$

3.7.2. Jacobian matrix in plane stress case

Stress in the normal direction can be assumed to be zero ($\partial\sigma_{33} = 0$). Therefore, for the calculation of consistent material tangent for plane stress, we have:

$$\partial\sigma_{33} = D_{3311}\partial\varepsilon_{11} + D_{3322}\partial\varepsilon_{22} + 2D_{3312}\partial\varepsilon_{12} + D_{3333}\partial\varepsilon_{33} = 0 \tag{73}$$

which leads to:

$$\partial\varepsilon_{33} = \Omega_{31}\partial\varepsilon_{11} + \Omega_{32}\partial\varepsilon_{22} + 2\Omega_{33}\partial\varepsilon_{12} \tag{74}$$

where

$$\Omega_{31} = -\frac{D_{3311}}{D_{3333}}$$

$$\Omega_{32} = -\frac{D_{3322}}{D_{3333}}$$

$$\Omega_{33} = -2\frac{D_{3312}}{D_{3333}}$$

Therefore, Jacobian matrix for plane stress case becomes:

$$\begin{Bmatrix}\partial\sigma_{11}\\ \partial\sigma_{22}\\ \partial\sigma_{12}\end{Bmatrix} = \begin{bmatrix} D_{1111} + \Omega_{31}D_{1133} & D_{1122} + \Omega_{32}D_{1133} & D_{1112} + \Omega_{33}D_{1133} \\ D_{2211} + \Omega_{31}D_{2233} & D_{2222} + \Omega_{32}D_{2233} & D_{2212} + \Omega_{33}D_{2233} \\ D_{1211} + \Omega_{31}D_{1233} & D_{1222} + \Omega_{32}D_{1233} & D_{1212} + \Omega_{33}D_{1233} \end{bmatrix} \begin{Bmatrix}\partial\varepsilon_{11}\\ \partial\varepsilon_{22}\\ \partial\varepsilon_{12}\end{Bmatrix} \tag{75}$$

3.8. GTN yield criterion

The GTN yield function for symmetric spherical voids is expressed as [6]:

$$\Phi = \left(\frac{q}{\bar{\sigma}_M}\right)^2 + 2q_1 f^* cosh\left(-\frac{3q_2 p}{2\bar{\sigma}_M}\right) - \left(1 + q_3 f^{*2}\right) = 0 \tag{76}$$

where q and p are equivalent stress and hydrostatic pressure respectively and q_1, q_2 and $q_3 (= {q_1}^2)$ are fit parameters and $\bar{\sigma}_M$ is the effective stress in matrix material. The relationship between f^* and void volume fraction f is given by [6]:

$$f^* = \begin{cases} f & f \leq f_c \\ f_c + \overline{k}(f - f_c) & f > f_c \end{cases} \tag{77}$$

where $\overline{k} = \frac{{f^*}_u - f_c}{f_F - f_c}$ and ${f^*}_u = \frac{1}{q_1}$. The latter is the ultimate value of f^* at ductile rupture. The parameter f_F represents the void volume fraction at final fracture, and f_c is the critical void volume fraction at the start of micro-void coalescence when the load carrying capability of the material drops sharply. In this model, two internal state variables H^1 and H^2 are related to plastic strain of the matrix material ($\bar{\varepsilon}^{pl}$) and void volume fraction (f) respectively, as noted below [35].

$$H^1 \equiv \bar{\varepsilon}^{pl} \tag{78}$$

$$H^2 \equiv f \tag{79}$$

As a result, yield function (Φ) is dependent on actual macroscopic stress states and internal scalar state variables as follows [35, 36]:

$$\Phi(\boldsymbol{\sigma}, H^{\alpha}) = \begin{cases} < 0 & V\,\dot{\Phi} < 0 \quad Linear\ elastic\ behaviour \\ = 0 & Linear\ elastic - strain\ hardening\ plastic\ behaviour \end{cases} \tag{80}$$

To evaluate the internal state variables, the plastic strain rate in the matrix $\dot{\bar{\varepsilon}}^{pl}$ can be expressed in the following form [35]:

$$(1-f)\bar{\sigma}_M \dot{\bar{\varepsilon}}^{pl} = \boldsymbol{\sigma}: \dot{\boldsymbol{\varepsilon}}^{pl} \longrightarrow \dot{\bar{\varepsilon}}^{pl} = \frac{\boldsymbol{\sigma}:\dot{\boldsymbol{\varepsilon}}^{pl}}{(1-f)\bar{\sigma}_M} \tag{81}$$

Both void growth and void nucleation are assumed to contribute towards void volume fraction as follows [6]:

$$\dot{f} = \dot{f}_{growth} + \dot{f}_{nucleation} \tag{82}$$

where

$$\dot{f}_{growth} = (1-f)\dot{\boldsymbol{\varepsilon}}^{pl}: \boldsymbol{I} \tag{83}$$

and

$$\dot{f}_{nucleation} = A\dot{\bar{\varepsilon}}^{pl} \tag{84}$$

where

$$A = \frac{f_N}{S_N\sqrt{2\pi}} exp\left\{-\frac{1}{2}\left[\frac{\bar{\varepsilon}^{pl} - \in_N}{S_N}\right]^2\right\} \tag{85}$$

and f_N is the volume fraction of nucleating particles. In Equation (85), a mean equivalent plastic strain $\in_N$ exists and the nucleation strain is assumed to be distributed normally about $\in_N$ with standard deviation S_N. By substituting Equation (20) into Equation (81), one obtains:

$$\Delta\bar{\varepsilon}^{pl} = \frac{\boldsymbol{\sigma}:\left(\frac{1}{3}\Delta\varepsilon_p \boldsymbol{I} + \Delta\varepsilon_q \boldsymbol{N}\right)}{(1-f)\bar{\sigma}_M\left(\bar{\varepsilon}^{pl}, \dot{\bar{\varepsilon}}^{pl}, T\right)} \tag{86}$$

By substituting Equation (19) into Equation (86), we have:

$$\Delta H^1 \equiv \Delta\bar{\varepsilon}^{pl} = \frac{\left(-p\Delta\varepsilon_p + q\Delta\varepsilon_q - \frac{3p}{2q}(H_{iiii}S_{ii})\Delta\varepsilon_q\right)}{(1-f)\bar{\sigma}_M\left(\bar{\varepsilon}^{pl}, \dot{\bar{\varepsilon}}^{pl}, T\right)} \tag{87}$$

By using Equations (19), (20), (82), (83), (84) and (85), we have:

$$\Delta H^2 \equiv \Delta f = (1-f)\Delta\boldsymbol{\varepsilon}^{pl}:\boldsymbol{I} + \left(\frac{f_N}{S_N\sqrt{2\pi}} exp\left\{-\frac{1}{2}\left[\frac{\bar{\varepsilon}^{pl}-\epsilon_N}{S_N}\right]^2\right\}\right)\Delta\bar{\varepsilon}^{pl} \tag{88-a}$$

or $\Delta H^2 \equiv \Delta f = (1-f)\left(\Delta\varepsilon_p + (H_{1111}S_{11} + H_{2222}S_{22} + H_{3333}S_{33})\frac{3\,\Delta\varepsilon_q}{2q}\right) +$

$$\left(\frac{f_N}{S_N\sqrt{2\pi}} exp\left\{-\frac{1}{2}\left[\frac{\bar{\varepsilon}^{pl}-\epsilon_N}{S_N}\right]^2\right\}\right)\Delta\bar{\varepsilon}^{pl} \tag{88-b}$$

3.8.1. Prolate ellipsoidal voids

The configuration of a single axisymmetric prolate ellipsoidal void with a major semi-axis (along the Oz direction) is shown in Figure 3.1. A prolate ellipsoidal void with major and minor radii of a_1 and b_1 is embedded in a matrix with major and minor raii of a_2 and b_2. The foci of these ellipsoidal voids are located at $z = \pm c$ and $e_1 = \frac{c}{a_1}$ and $e_2 = \frac{c}{a_2}$ are the eccentricities of inner and outer ellipsoids [37].

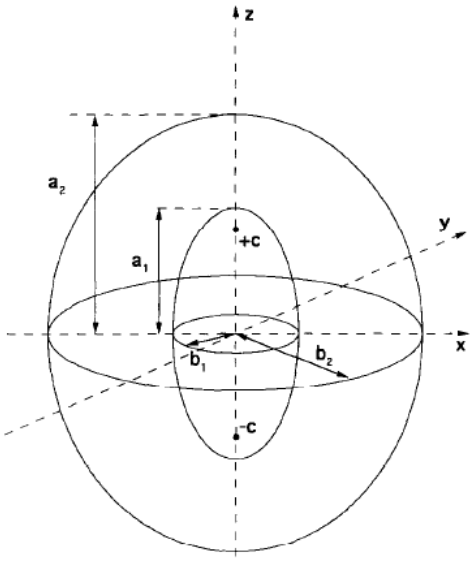

Figure 3. 1. Prolate ellipsoidal void configuration [37]

Yield function presented in Equation (76) only considers a spherical void. In the case of ellipsoidal voids, the yield function was revised to the following [38]:

$$\Phi = \left(\frac{q}{\bar{\sigma}_M}\right)^2 + 2q_1 f^* \cosh\left(-k\frac{p}{\bar{\sigma}_M}\right) - \left(1 + q_3 f^{*2}\right) = 0 \tag{89}$$

where

$$k = \left[\frac{1}{\sqrt{3}} + \left(\sqrt{3} - 2\right)\frac{ln\left(\frac{e_1}{e_2}\right)}{ln(f^*)}\right]^{-1} \tag{90}$$

$$e_1 = \sqrt{1 - e^{-2S}} \tag{91}$$

$$e_2 = \sqrt[3]{f^*(1 - e_2^2)(1 - e_1^2)}e_1 \tag{92}$$

when $S = ln\frac{a_1}{b_1}$ is the shape function and e_2 is obtained by solving the above cubic Equation (92). The rate of change of shape function ($\dot{S}$) can be expressed as [38]:

$$\dot{S} = 3\left(\frac{1-3K_1}{f^*} + 3K_2 - 1\right)\dot{\varepsilon}_m \tag{93}$$

where $$\dot{\varepsilon}_m = \frac{\dot{f^*}}{3(1-f^*)} \tag{94}$$

$$K_1 = \frac{1}{2e_1^2} - \frac{1-e_1^2}{2e_1^3} tanh^{-1} e_1 \tag{95}$$

$$K_2 = \frac{1}{2e_2^2} - \frac{1-e_2^2}{2e_2^3} tanh^{-1} e_2 \tag{96}$$

Lastly, the increment of shape function becomes:

$$dS = \frac{1}{(1-f^*)}\left(\frac{1-3K_1}{f^*} + 3K_2 - 1\right) \times df^* \tag{97}$$

It should be noted that $\frac{\partial \Phi}{\partial p}$, $\frac{\partial^2 \Phi}{\partial p^2}$, $\frac{\partial^2 \Phi}{\partial p \partial \bar{\varepsilon}^{pl}}$, $\frac{\partial^2 \Phi}{\partial p \partial f}$, $\frac{\partial \Phi}{\partial \bar{\varepsilon}^{pl}}$ and $\frac{\partial \Phi}{\partial f}$ must be recalculated for ellipsoidal voids in order to obtain the constants in Appendices I, II and III. This is shown in Appendix IV.

3.9. Flow chart of algorithm

The flow chart of the algorithm considering the GTN model for the 3D case that takes into account spherical voids is presented in Figure 3.2.

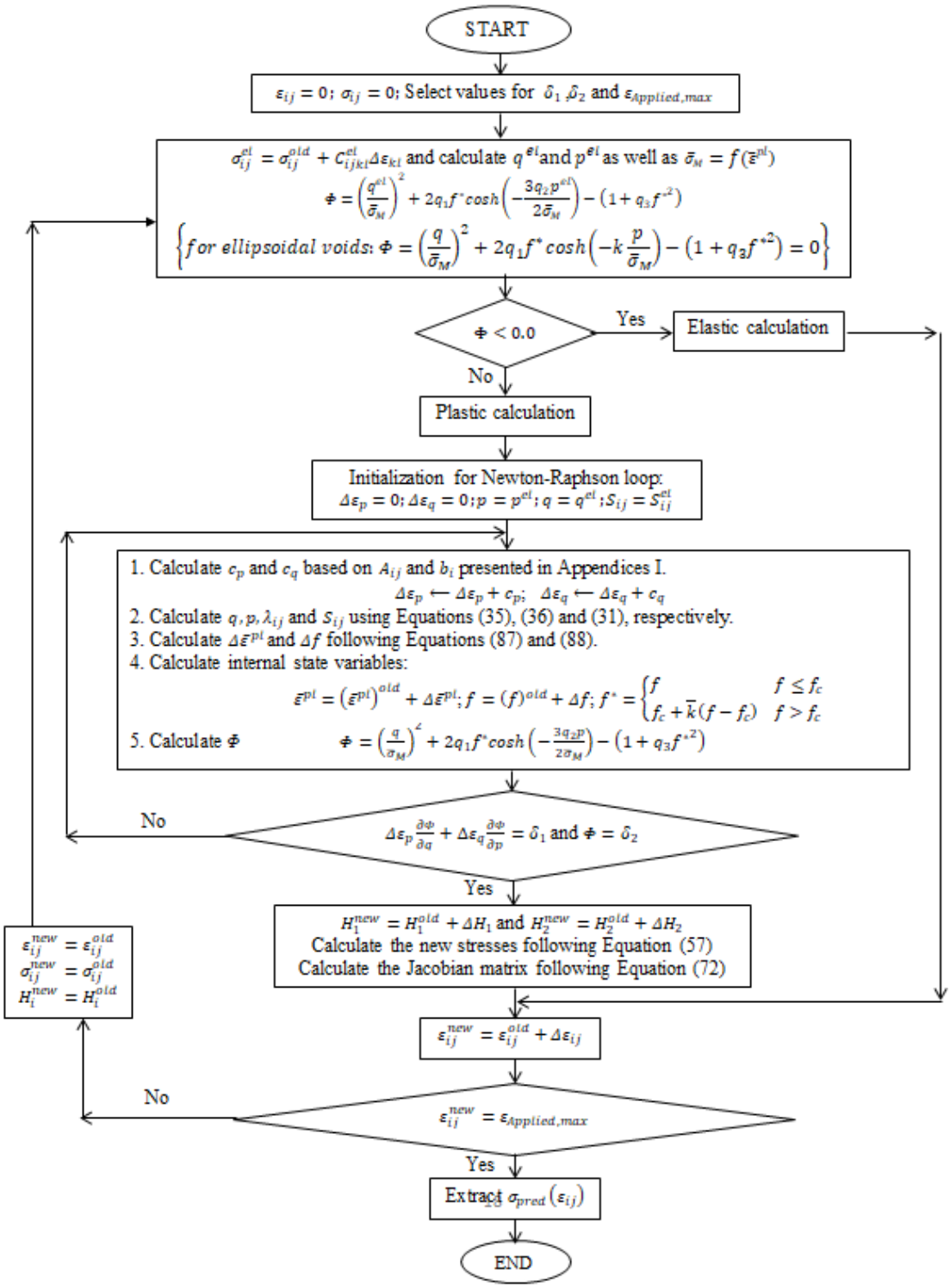

Figure 3. 2. Flow chart of the algorithm for the 3D case considering spherical voids

3.10. Numerical results and discussion

The GTN yield criterion based on Hill's quadratic anisotropic theory, as developed in the previous sections, is implemented using the UMAT subroutine of ABAQUS FE computational code to model the plastic and damage behavior of anisotropic ductile metals. In this section, the result for the isotropic case has been verified using a one-element FE model (Figure 3.3) and compared with the result presented in [35]. Subsequently, the results of different test models are presented for a 3D one-element model to understand the nature of each model. Afterward, a uniaxial tensile test configuration with a large number of elements is used to present the stress–strain curves for the isotropic and anisotropic models with an effective anisotropic coefficient. Finally, the effect of microvoid shape is scrutinized and a ductile fracture parametric study is performed.

3.10.1. One-element test

For verification of UMAT implementation, first, the Hill's quadratic anisotropic model in the GTN criterion is switched off by choosing a value of unity for the Hill's coefficients. Then, the results are compared with those presented in reference [35]. These results are shown in Figure 3.3 where a close agreement can be observed. A plane stress element is used for this case with the following constitutive law for the matrix material.

$$\frac{\bar{\sigma}_M}{\sigma_y} = \left(\frac{\bar{\sigma}_M}{\sigma_y} + \frac{3G}{\sigma_y}\bar{\varepsilon}^{pl}\right)^N \tag{98}$$

where σ_y and G are the tensile yield stress and shear modulus respectively. Also, to be consistent with the data utilized by Aravas [35], $N = 0.1$, $\sigma_y/E = 1/300$, $\nu = 0.3$, $q_1 = 1.5$, $q_2 = 1.0$, $q_3 = 2.25$ are selected for the matrix material elastic-plastic properties. Further, $f_N = 0.04$, $\varepsilon_N = 0.3$, $S_N = 0.1$ and $f_o = 0$ are assumed to describe the plastic strain-controlled nucleation.

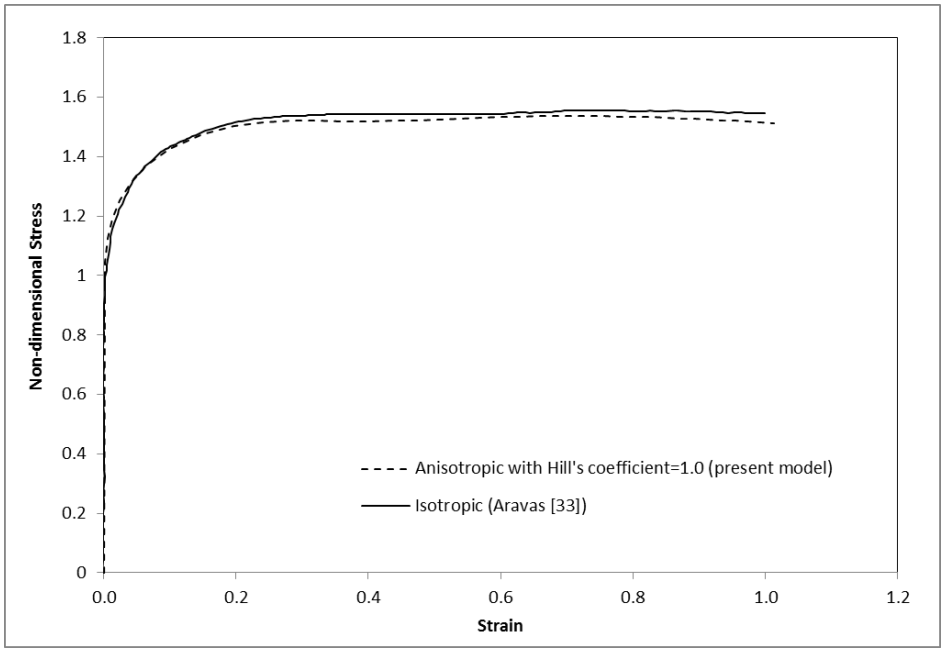

Figure 3. 3. Comparison results of our model and Aravas [35]

The equivalent stress versus strain curves and stress-11 versus strain-11 curves in a 3D element are shown in Figures 3.4–3.5 for different cases such as Von Mises, Hill's, and Gurson models with three cases of isotropic, anisotropic, and anisotropic with anisotropy coefficient to show the behavior of each case. Displacement in 1 direction is applied on only one surface of the 3D element which is perpendicular to 1 direction, and the opposite

surface is constrained. The data used in Figure 3.3 are considered when $\sigma_y = 250\ MPa$ and $H_{1111} = H_{2222} = 0.941, H_{3333} = 0.51, H_{2323} = H_{1313} = H_{1212} = 0.941$ for anisotropic cases. As shown in Figures 3.4 and 3.5, the equivalent stresses in cases of Von Mises and Hills criteria are the same when stress-11 is different. Damage growth is zero in Von Mises and Hill's criteria, and the equivalent stress–strain curves rise similar to the stress–strain curve of matrix material following Equation (98). Stress-11 and equivalent stress are the same in Von Mises material, but stress-11 is higher than the equivalent stress in Hill's criterion. The reason is that the Hill's constants are not equal to one in equivalent stress following Equation (12).

Figures 3.4 and 3.5 show that the stresses in isotropic Gurson model are lower than those in Von Mises criterion as damage grows and drops the stresses. However, the stresses in anisotropic Gurson case are much lower than those in isotropic Gurson case. Damage growth in the anisotropic case is high due to the additional term $(H_{1111}S_{11} + H_{2222}S_{22} + H_{3333}S_{33}) \times \frac{3\,\Delta\varepsilon_q}{2q} \times (1-f)$ for Δf in Equation (88). Using effective anisotropy coefficient instead of all Hill's quadratic anisotropy constants yields

$$H_{1111}S_{11} + H_{2222}S_{22} + H_{3333}S_{33} = \bar{H}(S_{11} + S_{22} + S_{33}) = 0 \tag{99}$$

Consequently, void volume fraction increment, as presented in Equation (88), will be reduced and becomes similar to that in the isotropic materials as follows:

$$\Delta f = (1-f)\Delta\varepsilon_p + \left(\frac{f_N}{S_N\sqrt{2\pi}} exp\left\{-\frac{1}{2}\left[\frac{\bar{\varepsilon}^{pl} - \epsilon_N}{S_N}\right]^2\right\}\right)\Delta\bar{\varepsilon}^{pl} \tag{100}$$

The results of the anisotropic case with effective anisotropy coefficient as replacement of individual Hill's constants $\left(H_{ijij} = \bar{H}\right)$ are shown in Figures 3.4 and 3.5. The equivalent stresses in isotropic and anisotropic Gurson models using effective anisotropy coefficient are similar, but stress-11 in the two models differs because the Hill's constant in the latter is not equal to one.

High values of stresses for matrix material must be considered with different Swift law parameters to predict the experimental stress–strain curve in anisotropic Gurson case. Using effective anisotropy coefficient instead of Hill's constants can improve stress–strain prediction with same Swift law parameters as those in the isotropic case. Effective stress is used following Hill's quadratic criteria based on Equations (33) and (34) when effective anisotropy coefficients are used. The damage-free stress–strain curve of matrix material for this case is realistic in metals, especially for aluminum alloys.

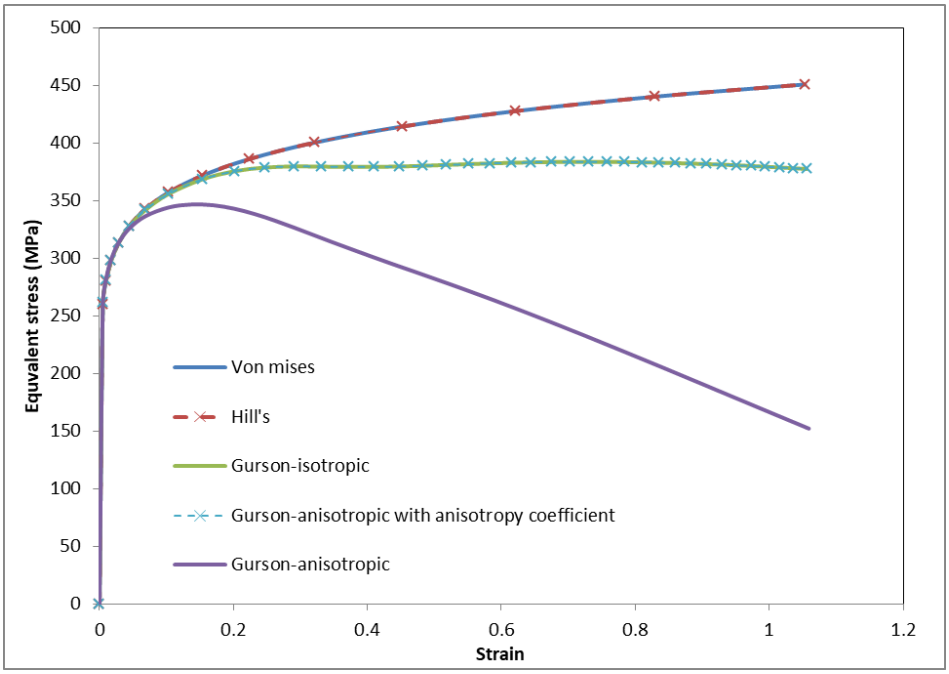

Figure 3. 4. Equivalent stress versus strain for different models in one 3D element

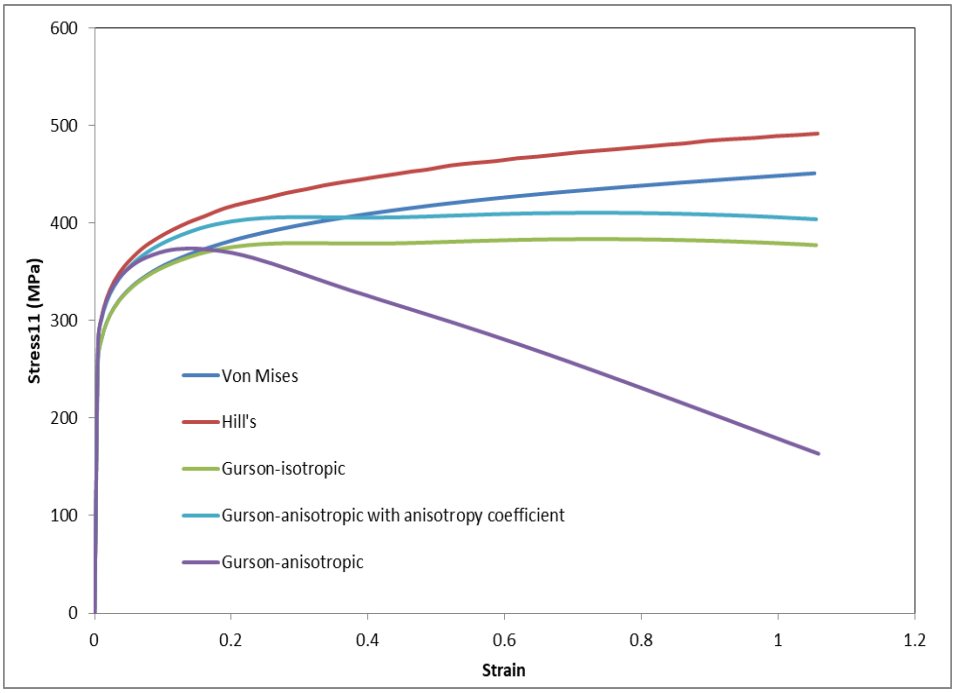

Figure 3. 5. Stress-11 versus strain-11 for different models in one 3D element

3.10.2. Brief discussion of using specific GTN parameters in modeling

Parametric studies of ductile damage using the GTN model for various metals [13, 39, 40] show that each parameter has a significant effect on the predicted results. However, the GTN model parameters of $q_1, q_2, q_3, f_0, f_c, \bar{k}, f_N, S_N$ and ε_N, as well as the hardening parameters that provide a damage-free stress–strain curve for the matrix material are obtained through curve fitting in [6, 7, 9, 41, 42]. In [10, 43-46], experimental models at micro-scale are used to identify the GTN model parameters. In [10], 5A06 aluminum alloy is screened by X-ray radiography to characterize damage. In [43], experiments with macroscopic and microscopic observations are used to characterize the aluminum alloy AL5182H19 quantitatively and to calibrate constitutive and damage models. However, void nucleation in the GTN model is defined by three parameters, namely, $f_N, S_N,$ and ε_N, and [11, 47] suggested to consider S_N and ε_N as constant and to only present a value for f_N. Furthermore, response surface methodology (RSM) is used in [8, 11, 15] to predict four parameters for aluminum alloys, namely, $f_0, f_c, \bar{k},$ and f_N. Global sets of information, such as force-displacement or force-necking curves, are used to identify the parameters in the GTN model by minimizing the least-squares function via a gradient base method in [48]. The global load-displacement is also used in [49] to determine the fracture parameters in the GTN. Meanwhile, a micromechanical modeling for ductile damage is used in [50] to determine the relevant parameters.

However, different values of f_N for AL6016 alloy are present in the literature, for example, $f_N = 0.036$ in [7] and $f_N = 0.075$ in [51] for AL6016 and $f_N = 0.05$ in [15] and $f_N = 0.095$ in [52] for AL6016-T4. In [52], the hardening parameters for AL6016 alloy are initially identified, such as in the RSM method, and void nucleation is considered for ductile damage only. Parameters related to ductile damage (S_N, f_N, ε_N and f_c) are identified through optimization. However, [52] stated that finding such a parameter set is extremely difficult, and nucleation parameters might be free for optimization. More importantly, it is stated in [52] that the void volume fraction evolution presented by Chu and Needleman model may not be suitable for AL6016 alloy. As a result, $f_N = 0.0$ is considered for AL6016 alloy in this study first. Then, a ductile damage parametric study is performed to elucidate the sensitivity of the parameters on the results. This study aims to describe the extended Gurson model by using Hill's criterion for anisotropic metals. The GTN model is not considered in the algorithm presented in [35], and only the Gurson model for isotropic material is discussed.

3.10.3. Tensile test

Tensile test simulation results are reported here for comparison with experimental results of Brunet et al. [7] for AA6016 aluminum sheet. Sample geometry in ABAQUS is shown in Figure 3.6. The 8-node solid element C3D8 is considered and displacements on both sides of the specimen are applied. Plastic anisotropy ratios of $R_0 = R_{45} = R_{90} = 0.7$ are considered based on the experimental results presented in [7] and Swift law in the form

$\sigma = B(C + \bar{\varepsilon}^{pl})^n$. Young's modulus and Poisson's ratio of 70 GPa and 0.33 respectively, typical of aluminum sheet, are assumed. In the following subsections, the results of proposed model for different test cases are presented and the parameters $f_0, S_N, \varepsilon_N, f_N, f_c, k, B, C$ and n are calibrated based on the ability of the model to reproduce the experimental results. The load–displacement curve of uniaxial tensile test in ABAQUS is calculated to present the engineering stress–strain curve, which is compared with experimental stress–strain curve.

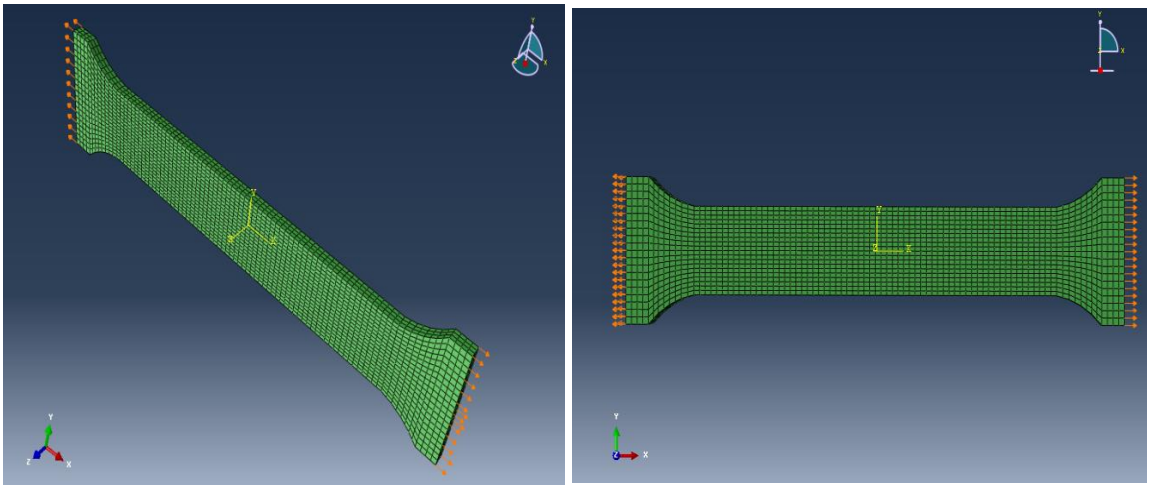

(a) Isometric view (b) In-plane view

Figure 3. 6. Tensile test specimen geometry

3.10.3.1. Isotropic case

The result of the isotropic case, $H_{ijij} = 1.0$, are first obtained using calibrated parameters shown in Table 3.1. The results, in Figure 3.7, show good agreement with the experiments.

Table 3. 1. Calibrated material parameters for the isotropic case

f_0	S_N	ε_N	f_N	f_c	$\bar{k}$	B	C	n
0.001	0.01	0.3	0.0	0.0013	45	780 MPa	0.0380445	0.525

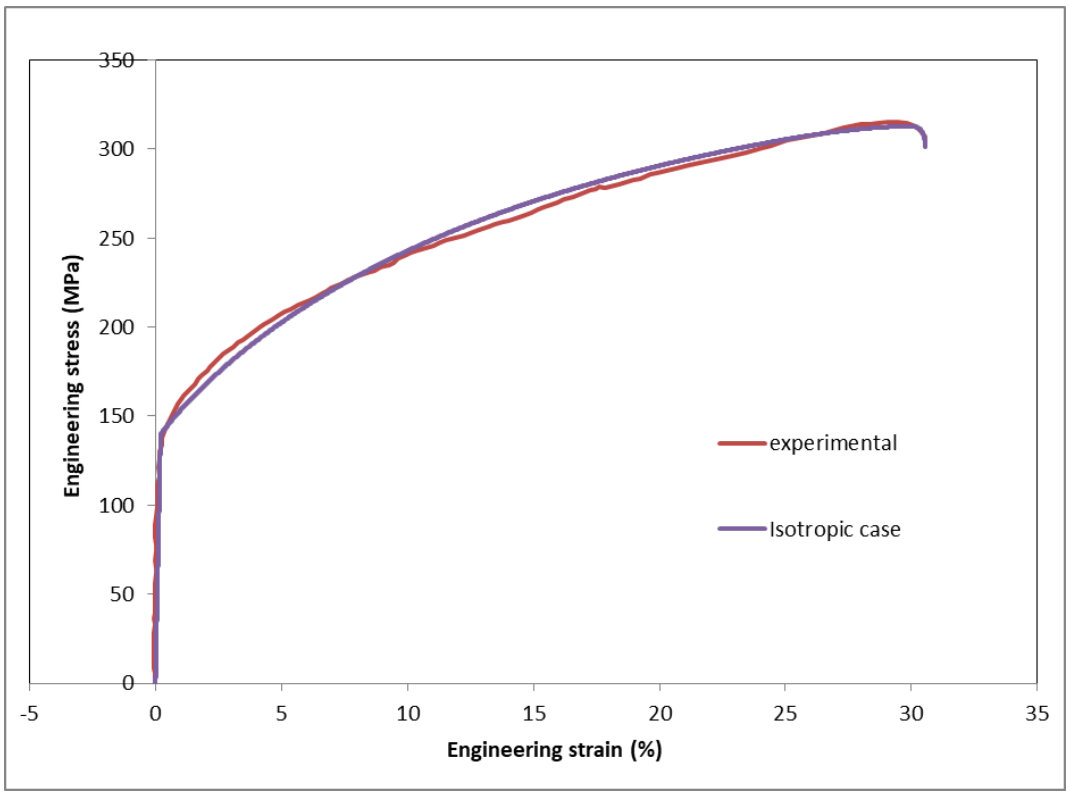

Figure 3. 7. Comparison with experimental results for the isotropic case

3.10.3.2. Anisotropic case using effective anisotropy coefficient

As shown in subsection 3.10.1, damage growth in the anisotropic case is high due to the additional term $(H_{1111}S_{11} + H_{2222}S_{22} + H_{3333}S_{33}) \times \frac{3\,\Delta\varepsilon_q}{2q} \times (1-f)$ for Δf in Equation (88). Void volume fraction increment as presented in Equation (88) will be reduced and becomes similar to that in the isotropic materials using effective anisotropy coefficient instead of all Hill's quadratic anisotropy constants following Equation (100).

As mentioned earlier, load–displacement curve is calculated to predict the engineering stress–strain curve in metals. Load is calculated on the basis of generated stress in the direction where displacement is applied. Figure 3.5 shows that the generated stress in anisotropic cases is higher than that in isotropic cases. Therefore, a higher stress in matrix material must be considered in anisotropic case using effective anisotropy coefficient than that considered in isotropic case. The result of the anisotropic case with effective anisotropy coefficient as replacement of individual Hill's constants $\left(H_{ijij} = \bar{H}\right)$ is shown in Figure 3.8. The calibrated parameters are shown in Table 3.2.

The effective stress in anisotropic case with effective anisotropy coefficient is used following Hill's quadratic criteria based on Equations (33) and (34) when effective anisotropy coefficients are considered. The damage-free stress–strain curve of matrix material for this case is realistic in metals, especially for aluminum alloys. Very high values for matrix material must be considered if anisotropic GTN model with effective anisotropy coefficients is utilized.

Table 3. 2. Calibrated parameters for the anisotropic case using effective anisotropy coefficient

f_0	S_N	ε_N	f_N	f_c	$\bar{k}$	B	C	n
0.001	0.01	0.3	0.0	0.0013	26	740 MPa	0.062450	0.6

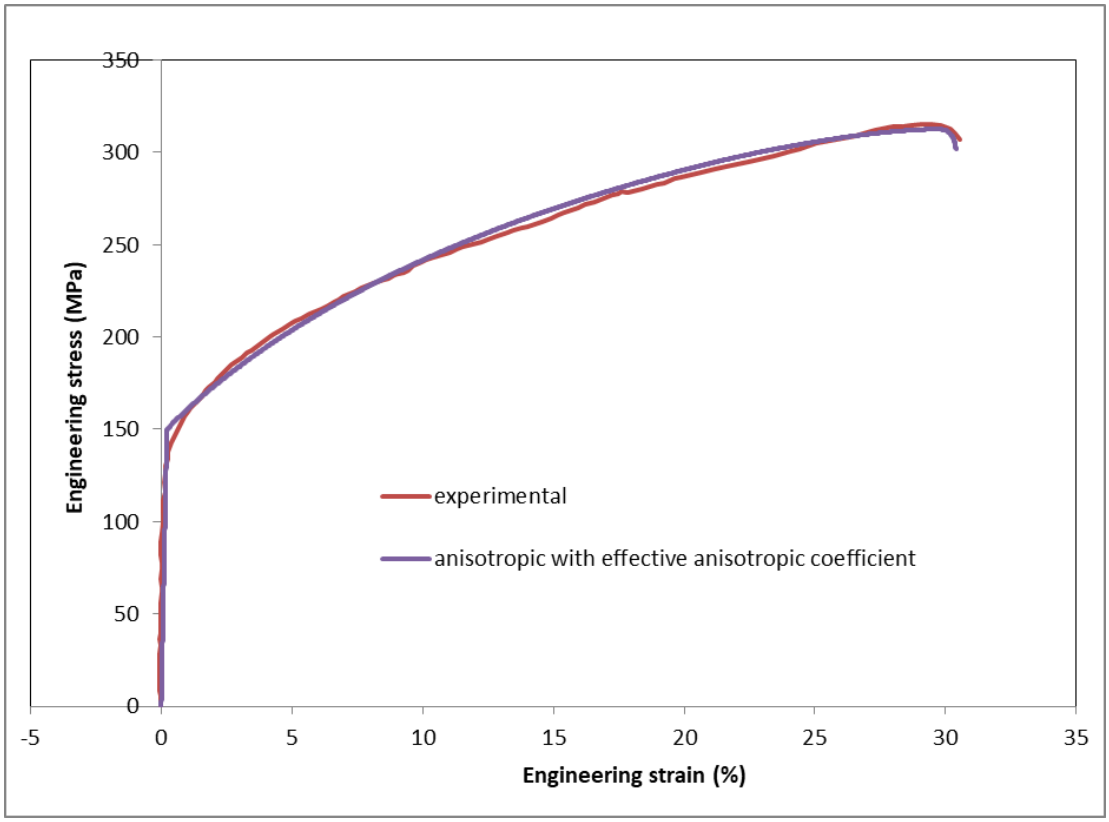

Figure 3. 8. Comparison with experimental results for the anisotropic case using effective anisotropy coefficient

3.10.3.3. Spherical voids versus ellipsoidal voids

In this section, the effect of evolution of void volume fraction and void shape parameter (S) in ellipsoidal voids with effective local plastic strain is investigated. As mentioned earlier for Equations (90–92), parameter k will vary with S. This parameter is considered instead of q_2, which is a constant for spherical voids. Figure 3.9(a) shows void volume fraction versus effective local plastic strain for spherical and ellipsoidal voids at a point where necking occurs in the uniaxial tensile test for the anisotropic case using effective anisotropy coefficient. Void shape parameter S versus effective local plastic strain in ellipsoidal voids is also shown in Figure 3.9(b) in which the initial S value is assumed to be 1.6. The exact initial value for S must be obtained experimentally, but this paper only aims to describe the implementation and extension of GTN model for various cases. Clearly, void volume fraction and S variation vary considerably with effective local plastic strain when $f = f_c$, following Equation (77). Overall, f reaches f_c with lower value of local plastic strain in ellipsoidal voids than that in spherical voids, and necking occurs early. S value decreases with the increase in plastic strain, and a reduction in S value indicates that ellipsoidal voids have a tendency to become spherical as reported in [38].

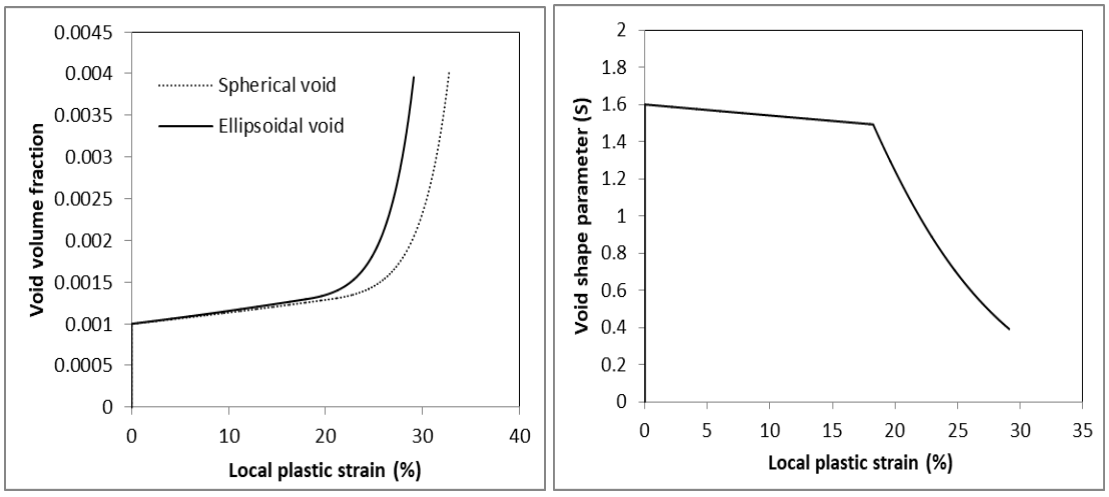

(a) (b)

Figure 3. 9. A comparison of evolution of void volume fraction and void shape parameter with effective local plastic strain for initially spherical and ellipsoidal voids, (a) void volume fraction, and (b) void shape parameter (S), in the anisotropic case using anisotropy coefficient

3.10.3.4. Ductile fracture parametric study

As mentioned earlier, it is suggested in literature to consider S_N and ε_N as constant and only to deal with f_N. Furthermore, four parameters, such as $f_0, f_c, \bar{k},$ and f_N, defined the ductile damage of the material. Moreover, the exact value of f_N for Al6016 alloy is not available in literature, and zero value has been considered to present the result in this study, as mentioned in section 10.2. The anisotropic model does not provide good results. Therefore, an anisotropic model with an effective anisotropic coefficient was proposed. Hill's criterion, as an effective stress, is used for the anisotropic model with an effective anisotropic coefficient to define the anisotropy of the material.

In this section, we analyzed the sensitivity of the results with f_N, f_c, and $\bar{k}$ in the case of anisotropic when the effective anisotropic coefficient is used. In these results, $f_0 = 0.001$ and its sensitivity is not investigated because a low value initial void volume fraction is a reasonable consideration. Figure 3.10 presents the stress–strain curves for two different cases with varying f_N values when other parameters are constant. Ductile damage clearly occurs early with the increase in f_N. f_c must be recalibrated to match the simulation results with experimental data. However, in Figure 3.10, f_c is considered constant to show the effect of f_N. Figure 3.11 presents the results with varying f_c values when other parameters are constant. Figure 3.11 shows that ductile damage occurs early with the decrease in f_c.

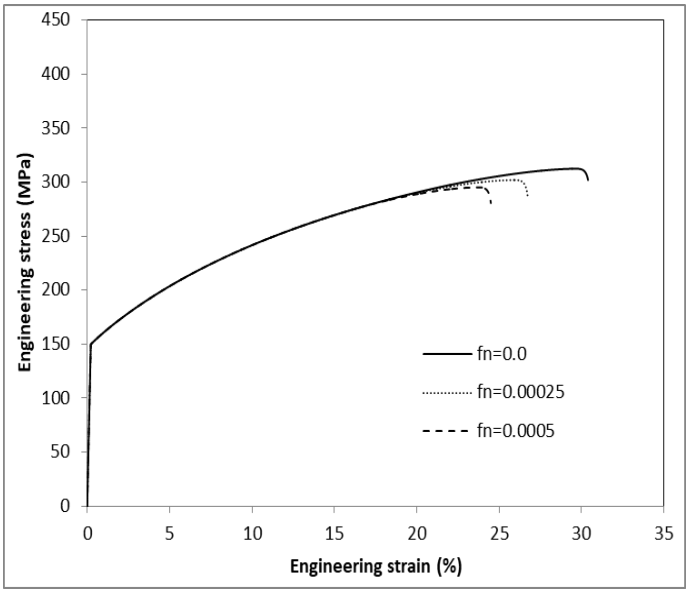

Figure 3. 10. f_N sensitivity on ductile damage

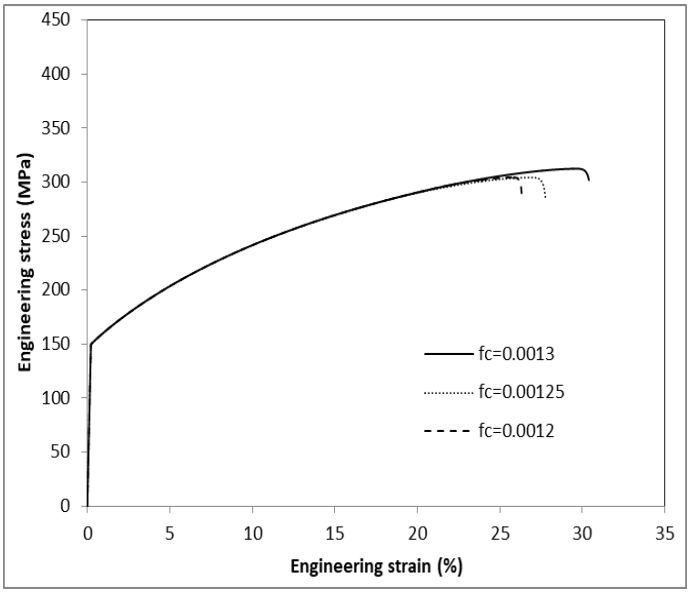

Figure 3 .11 .f_c sensitivity on ductile damage

The sensitivity of the results with $\bar{k}$ is presented in Figure 3.12. The load-carrying capability of the material drops when $f = f_c$. The void volume fraction increases linearly with the slope,$\bar{k}$, following Equation (77). Thus, the load capability of the material at ductile damage decreases with the increase in $\bar{k}$. Figure 3.12(a) shows that $f_N = 0$, which does not affect the ductile damage. The load capability of the material also does not drop sharply. Drop in load capability of material occurs first with nearly the same rate with different $\bar{k}$ values, and then it changes sharply at different strains. In Figure 3.12(b), the effect of $\bar{k}$ on drop in load capability of material has been investigated by considering a non-zero value for f_N $(f_N = 0.036)$. In this way, f_c must be recalibrated to match the simulation results with experimental data. Figure 3.12(b) shows that load capability of material drops at the same strain with varying $\bar{k}$ but with different slopes.

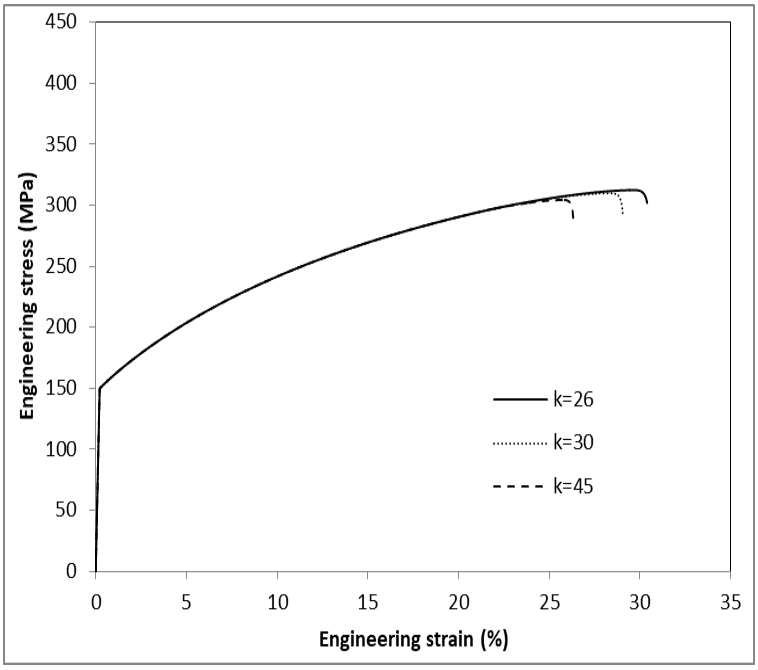

(a) $f_N = 0$

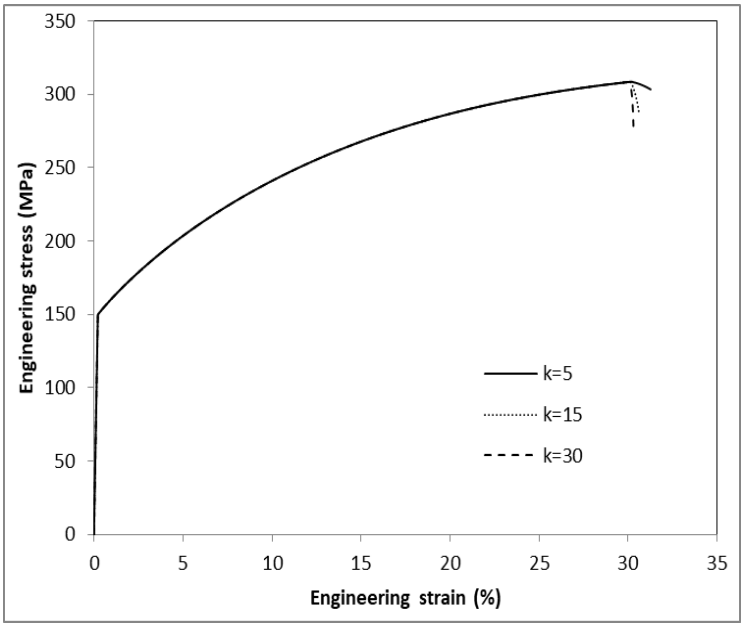

(b) $f_N = 0.036$

Figure 3 12 .$\bar{k}$ sensitivity on ductile damage

3.11. Conclusions

In the present study, GTN plasticity and damage criterion are extended to cover Hill's quadratic anisotropy to predict plastic and damage responses of anisotropic ductile metals. ABAQUS-Standard FE code is used to implement Hill's quadratic anisotropic matrix based on the GTN material model with linearized tangent moduli formulation as a user material subroutine. A uniaxial tensile test sample geometry is used, and the required parameters for simulation are calibrated to reproduce the experimental result of the AA6016 sheet. Swift law parameters in constitutive law for damage-free stress–strain curve of matrix material are initially obtained. Next, the ductile damage parameters are calibrated by the model's ability to reproduce the experimental results. Hill's quadratic anisotropy case indicates higher damage evolution compared with the isotropic case. Thus, higher values for the damage-free stress–strain curve must be considered to reproduce the experimental results. Hence, effective anisotropic coefficients are used instead of Hill's anisotropic coefficients to reduce damage growth. Moreover, algorithm implementations for ellipsoidal voids and plane stress element for the anisotropic case are performed and described in detail. The results show that the uniaxial stress–strain responses for 3D and plane stress elements are nearly identical. Finally, the salient conclusions of this study can be summarized as follows:

- The results for three-dimensional and plane stress elements are similar.

- Void volume fraction reaches a critical value in ellipsoidal voids earlier than in spherical voids. As a result, necking occurs earlier in the material in ellipsoidal voids.
- Anisotropic case presents higher damage evolution compared with the experimental results. Thus, higher values for the damage-free stress-strain curve in the matrix should be considered to reproduce the experimental data which is unrealistic in metals.
- An approximate model is considered to predict the plastic response of the anisotropic metals. In this approximate model, the effective anisotropy coefficient is used for Hill's 48 constants. The effects of individual Hill's constants are removed, but the substantial damage growth is neglected without changing the equivalent stress in anisotropic model.

Appendix I - Parameters to define c_p and $c_q$in 3-D case

$$A_{11} = \frac{\partial g}{\partial q} + \Delta\varepsilon_p \left(\frac{\partial^2 g}{\partial q \partial p} \frac{\partial p}{\partial \Delta\varepsilon_p} + \sum_{\alpha=1}^{n} \left\{ \frac{\partial^2 g}{\partial q \partial H^\alpha} \frac{\partial H^\alpha}{\partial \Delta\varepsilon_p} \right\} \right) + \Delta\varepsilon_q \left(\frac{\partial^2 g}{\partial p^2} \frac{\partial p}{\partial \Delta\varepsilon_p} + \sum_{\alpha=1}^{n} \left\{ \frac{\partial^2 g}{\partial p \partial H^\alpha} \frac{\partial H^\alpha}{\partial \Delta\varepsilon_p} \right\} \right)$$

$$A_{12} = \frac{\partial g}{\partial p} + \Delta\varepsilon_p \left(\frac{\partial^2 g}{\partial q^2} \frac{\partial q}{\partial \Delta\varepsilon_q} + \sum_{\alpha=1}^{n} \left\{ \frac{\partial^2 g}{\partial q \partial H^\alpha} \frac{\partial H^\alpha}{\partial \Delta\varepsilon_q} \right\} \right)$$

$$+ \Delta\varepsilon_q \left(\frac{\partial^2 g}{\partial q \partial p} \frac{\partial q}{\partial \Delta\varepsilon_q} + \sum_{\alpha=1}^{n} \left\{ \frac{\partial^2 g}{\partial p \partial H^\alpha} \frac{\partial H^\alpha}{\partial \Delta\varepsilon_q} \right\} \right)$$

$$A_{21} = \frac{\partial \Phi}{\partial p} \frac{\partial p}{\partial \Delta\varepsilon_p} + \sum_{\alpha=1}^{n} \left\{ \frac{\partial \Phi}{\partial H^\alpha} \frac{\partial H^\alpha}{\partial \Delta\varepsilon_p} \right\}$$

$$A_{22} = \frac{\partial \Phi}{\partial q} \frac{\partial q}{\partial \Delta\varepsilon_q} + \sum_{\alpha=1}^{n} \left\{ \frac{\partial \Phi}{\partial H^\alpha} \frac{\partial H^\alpha}{\partial \Delta\varepsilon_q} \right\}$$

$$b_1 = -\Delta\varepsilon_p \frac{\partial g}{\partial q} - \Delta\varepsilon_q \frac{\partial g}{\partial p}$$

$$b_2 = -\Phi$$

$$\frac{\partial H^\alpha}{\partial \Delta\varepsilon_p} = \sum_{\beta=1}^{n} c_{\alpha\beta} \left(\frac{\partial h^\beta}{\partial \Delta\varepsilon_p} + \frac{\partial h^\beta}{\partial p} \frac{\partial p}{\partial \Delta\varepsilon_p} \right)$$

$$\frac{\partial H^\alpha}{\partial \Delta\varepsilon_q} = \sum_{\beta=1}^{n} c_{\alpha\beta} \left(\frac{\partial h^\beta}{\partial \Delta\varepsilon_q} + \frac{\partial h^\beta}{\partial q} \frac{\partial q}{\partial \Delta\varepsilon_q} \right)$$

where, $\frac{\partial p}{\partial \Delta\varepsilon_p} = K$, $\frac{\partial q}{\partial \Delta\varepsilon_q} = -3G\bar{H}$, and $c_{\alpha\beta}$ is defined as:

$$c_{\alpha\beta} = \left(\delta_{\alpha\beta} - \frac{\partial h^\alpha}{\partial H^\beta} \right)^{-1}$$

Appendix II - Parameters to define c_p , $c_q$and c_3 in the plane stress case

$$A_{13} = \Delta\varepsilon_p \left(\frac{\partial^2 g}{\partial q^2} \frac{\partial q}{\partial \Delta\varepsilon_3} + \frac{\partial^2 g}{\partial q \partial p} \frac{\partial p}{\partial \Delta\varepsilon_3} \right) + \Delta\varepsilon_q \left(\frac{\partial^2 g}{\partial p^2} \frac{\partial p}{\partial \Delta\varepsilon_3} + \frac{\partial^2 g}{\partial q \partial p} \frac{\partial q}{\partial \Delta\varepsilon_3} \right)$$

$$A_{23} = \frac{\partial \Phi}{\partial p} \frac{\partial p}{\partial \Delta\varepsilon_3} + \frac{\partial \Phi}{\partial q} \frac{\partial q}{\partial \Delta\varepsilon_3}$$

$$A_{31} = \left(q + 3G\Delta\varepsilon_q \bar{H} \right) \frac{\partial p}{\partial \Delta\varepsilon_p}$$

$$A_{32} = -\left(S_{33}^{el} + \frac{4}{3} G\Delta\varepsilon_3 \right) \frac{\partial q}{\partial \Delta\varepsilon_q}$$

$$A_{33} = \frac{\partial q}{\partial \Delta\varepsilon_3} p + \left(q + 3G\Delta\varepsilon_q \bar{H} \right) \frac{\partial p}{\partial \Delta\varepsilon_3} - \frac{4}{3} Gq - \left(S_{33}^{el} + \frac{4}{3} G\Delta\varepsilon_3 \right) \frac{\partial q}{\partial \Delta\varepsilon_3}$$

$$b_3 = \left(q + 3G\Delta\varepsilon_q \bar{H} \right) p - \left(S_{33}^{el} + \frac{4}{3} G\Delta\varepsilon_3 \right) q$$

where,

$\frac{\partial p}{\partial \Delta\varepsilon_p} = K, \frac{\partial p}{\partial \Delta\varepsilon_3} = -K$, $\frac{\partial q}{\partial \Delta\varepsilon_q} = -3G\bar{H}$, $\frac{\partial q}{\partial \Delta\varepsilon_3} = \frac{3GH_{3333} S_{33}^{el} + 4G^2 H_{3333} \Delta\varepsilon_3}{q + 3G\Delta\varepsilon_q \bar{H}}$ and $\frac{\partial^2 \Phi}{\partial q \partial p} = 0.$

Also, $A_{11}, A_{12}, A_{21}, A_{22}, b_1 \; and \; b_2$ are the same as in Appendix I.

Appendix III – Parameters to define Jacobian matrix

$$A_{11} = \frac{\partial g}{\partial q} + \sum_{\alpha=1}^{n} \sum_{\beta=1}^{n} \left\{ \Delta\varepsilon_p \frac{\partial^2 g}{\partial q \partial H^\alpha} + \Delta\varepsilon_q \frac{\partial^2 g}{\partial p \partial H^\alpha} \right\} c_{\alpha\beta} \frac{\partial h^\beta}{\partial \Delta\varepsilon_p}$$

$$A_{12} = \frac{\partial g}{\partial p} + \sum_{\alpha=1}^{n}\sum_{\beta=1}^{n}\left\{\Delta\varepsilon_p \frac{\partial^2 g}{\partial q \partial H^\alpha} + \Delta\varepsilon_q \frac{\partial^2 g}{\partial p \partial H^\alpha}\right\} c_{\alpha\beta}\frac{\partial h^\beta}{\partial \Delta\varepsilon_q}$$

$$A_{21} = \sum_{\alpha=1}^{n}\sum_{\beta=1}^{n}\frac{\partial \Phi}{\partial H^\alpha} c_{\alpha\beta}\frac{\partial h^\beta}{\partial \Delta\varepsilon_p}$$

$$A_{22} = \sum_{\alpha=1}^{n}\sum_{\beta=1}^{n}\frac{\partial \Phi}{\partial H^\alpha} c_{\alpha\beta}\frac{\partial h^\beta}{\partial \Delta\varepsilon_q}$$

$$B_{11} = \frac{1}{3}\Delta\varepsilon_p\left(\frac{\partial^2 g}{\partial q \partial p} + \sum_{\alpha=1}^{n}\sum_{\beta=1}^{n}\frac{\partial^2 g}{\partial q \partial H^\alpha} c_{\alpha\beta}\frac{\partial h^\beta}{\partial p}\right)$$

$$+\frac{1}{3}\Delta\varepsilon_q\left(\frac{\partial^2 g}{\partial p^2} + \sum_{\alpha=1}^{n}\sum_{\beta=1}^{n}\frac{\partial^2 g}{\partial p \partial H^\alpha} c_{\alpha\beta}\frac{\partial h^\beta}{\partial p}\right)$$

$$B_{12} = -\Delta\varepsilon_p\left(\frac{\partial^2 g}{\partial q^2} + \sum_{\alpha=1}^{n}\sum_{\beta=1}^{n}\frac{\partial^2 g}{\partial q \partial H^\alpha} c_{\alpha\beta}\frac{\partial h^\beta}{\partial q}\right)$$

$$-\Delta\varepsilon_q\left(\frac{\partial^2 g}{\partial q \partial p} + \sum_{\alpha=1}^{n}\sum_{\beta=1}^{n}\frac{\partial^2 g}{\partial p \partial H^\alpha} c_{\alpha\beta}\frac{\partial h^\beta}{\partial q}\right)$$

$$B_{21} = \frac{1}{3}\left(\frac{\partial \Phi}{\partial p} + \sum_{\alpha=1}^{n}\sum_{\beta=1}^{n}\frac{\partial \Phi}{\partial H^\alpha} c_{\alpha\beta}\frac{\partial h^\beta}{\partial p}\right)$$

$$B_{22} = -\left(\frac{\partial \Phi}{\partial q} + \sum_{\alpha=1}^{n}\sum_{\beta=1}^{n}\frac{\partial \Phi}{\partial H^\alpha} c_{\alpha\beta}\frac{\partial h^\beta}{\partial q}\right)$$

Appendix IV - Terms for calculating constants in Appendices I, II and III for ellipsoidal voids

$$\frac{\partial \Phi}{\partial p} = -2q_1 f^* \frac{k}{\bar{\sigma}_M} \sinh\left(-k\frac{p}{\bar{\sigma}_M}\right)$$

$$\frac{\partial^2 \Phi}{\partial p^2} = 2q_1 f^* \frac{k^2}{{\bar{\sigma}_M}^2} \cosh\left(-k\frac{p}{\bar{\sigma}_M}\right)$$

$$\frac{\partial^2 \Phi}{\partial p \partial \bar{\varepsilon}^{pl}} = 2q_1 f^* \frac{k}{{\bar{\sigma}_M}^2}\frac{d\bar{\sigma}_M}{d\bar{\varepsilon}^{pl}} \left\{sinh\left(-k\frac{p}{\bar{\sigma}_M}\right) - \frac{kp}{\bar{\sigma}_M}\cosh\left(-k\frac{p}{\bar{\sigma}_M}\right)\right\}$$

$$\frac{\partial^2 \Phi}{\partial p \partial f} = -2q_1 \frac{k}{\bar{\sigma}_M}\sinh\left(-k\frac{p}{\bar{\sigma}_M}\right) \times \frac{\partial f^*}{\partial f} - 2q_1 \frac{f^*}{\bar{\sigma}_M}\sinh\left(-k\frac{p}{\bar{\sigma}_M}\right) \times \frac{\partial k}{\partial f}$$

$$+ 2q_1 f^* \frac{kp}{{\bar{\sigma}_M}^2}\cosh\left(-k\frac{p}{\bar{\sigma}_M}\right)\frac{\partial k}{\partial f}$$

where $$\frac{\partial k}{\partial f} = \frac{\partial k}{\partial f^*} \times \frac{\partial f^*}{\partial f}$$

$$\frac{\partial \Phi}{\partial \bar{\varepsilon}^{pl}} = -2\frac{q^2}{{\bar{\sigma}_M}^3}\frac{d\bar{\sigma}_M}{d\bar{\varepsilon}^{pl}} + 2q_1 f^* \sinh\left(-\frac{kp}{\bar{\sigma}_M}\right)\frac{kp}{{\bar{\sigma}_M}^2}\frac{d\bar{\sigma}_M}{d\bar{\varepsilon}^{pl}}$$

$$\frac{\partial \Phi}{\partial f} = 2q_1 \cosh\left(-\frac{kp}{\bar{\sigma}_M}\right)\frac{\partial f^*}{\partial f} - 2q_1 f^* \sinh\left(-\frac{kp}{\bar{\sigma}_M}\right)\frac{p}{\bar{\sigma}_M}\frac{\partial k}{\partial f} - 2q_3 f^* \frac{\partial f^*}{\partial f}$$

REFERENCES

1. Gurson, A.L., Continuum theory of ductile rupture by void nucleation and growth: Part I—Yield criteria and flow rules for porous ductile media. *Journal of engineering materials and technology*, 1977. 99(1): p. 2-15.

2. Tvergaard, V., Influence of voids on shear band instabilities under plane strain conditions. *International Journal of fracture*, 1981. 17(4): p. 389-407.

3. Tvergaard, V., On localization in ductile materials containing spherical voids. *International Journal of Fractu*re, 1982. 18(4): p. 237-252.

4. Needleman, A. and V. Tvergaard, An analysis of ductile rupture in notched bars. *Journal of the Mechanics and Physics of Solids*, 1984. 32(6): p. 461-490.

5. Tvergaard, V. and A. Needleman, Analysis of the cup-cone fracture in a round tensile bar. *Acta metallurgica*, 1984. 32(1): p. 157-169.

6. Le Maoût, N., S. Thuillier, and P.-Y. Manach, Aluminum alloy damage evolution for different strain paths–Application to hemming process. *Engineering Fracture Mechanics*, 2009. 76(9): p. 1202-1214.

7. Brunet, M., S. Mguil, and F. Morestin, Analytical and experimental studies of necking in sheet metal forming processes. *Journal of Materials Processing Technology*, 1998. 80: p. 40-46.

8. Kami, A., et al., Numerical determination of the forming limit curves of anisotropic sheet metals using GTN damage model. *Journal of Materials Processing Technology*, 2015. 216: p. 472-483.

9. Chen, Z. and X. Dong, The GTN damage model based on Hill'48 anisotropic yield criterion and its application in sheet metal forming. *Computational Materials Science*, 2009. 44(3): p. 1013-1021.

10. Jin, C., et al., Modeling thermal cycling induced micro-damage in aluminum welds: An extension of Gurson void nucleation model. *Computational Materials Science*, 2008. 43(4): p. 1165-1171.

11. Abbasi, M., et al., Identification of GTN model parameters by application of response surface methodology. *Procedia engineering*, 2011. 10: p. 415-420.

12. Shen, Y., et al., Experimental and numerical characterization of anisotropic damage evolution of forged Al6061-T6 alloy. *Procedia Engineering*, 2011. 10: p. 3429-3434.

13. Achouri, M., et al. Implementation and validation of a Gurson damage model modified for shear loading: effect of void growth rate and mesh size on the predicted behavior. *in Key Engineering Materials*. 2012. *Trans Tech Publ*.

14. Ramazani, A., et al., Failure analysis of DP600 steel during the cross-die test. *Computational Materials Science*, 2012. 64: p. 101-105.

15. Kami, A., et al., Application of a GTN damage model to predict the fracture of metallic sheets subjected to deep-drawing. *Proc Rom Acad A*, 2014. 15: p. 300-309.

16. Simha, C.H.M., S. Xu, and W. Tyson, Computational modeling of the drop-weight tear test: A comparison of two failure modeling approaches. *Engineering Fracture Mechanics*, 2015. 148: p. 304-323.

17. Lim, Y., et al., Formability of coated vinyl on sheet metal during deep drawing process. *Journal of Materials Processing Technology*, 2016. 227: p. 178-189.

18. Soyarslan, C., et al., Modeling of fracture in small punch tests for small-and large-scale yielding conditions at various temperatures. *International Journal of Mechanical Sciences*, 2016. 106: p. 266-285.

19. Ayatollahi, M., et al., 3D Micromechanical Modeling of Failure and Damage Evolution in Dual Phase Steel Based on a Real 2D Microstructure. *Acta Mechanica Solida Sinica*, 2016. 29(1): p. 95-110.

20. Xin, H., S. Sun, and J. Fish, A surrogate modeling approach for additive-manufactured materials. *International Journal for Multiscale Computational Engineering*, 2017.

21. Hill, R. A theory of the yielding and plastic flow of anisotropic metals. *in Proceedings of the Royal Society of London A: Mathematical, Physical and Engineering Sciences*. 1948. The Royal Society.

22. Liao, K.-C., J. Pan, and S. Tang, Approximate yield criteria for anisotropic porous ductile sheet metals. *Mechanics of Materials*, 1997. 26(4): p. 213-226.

23. Hosford, W., A generalized isotropic yield criterion. *Journal of Applied Mechanics*, 1972. 39(2): p. 607-609.

24. Barlat, F. and K. Lian, Plastic behavior and stretchability of sheet metals. Part I: A yield function for orthotropic sheets under plane stress conditions. *International Journal of Plasticity*, 1989. 5(1): p. 51-66.

25. Ragab, A.-R.A. and S.E.A. Bayoumi, Engineering solid mechanics: fundamentals and applications. 1998: *CRC Press*.

26. Kim, Y., et al., Approximate yield criterion for voided anisotropic ductile materials. *KSME international journal*, 2001. 15(10): p. 1349-1355.

27. Kim, Y.S., et al. Prediction of forming limits for voided anisotropic sheets using strain gradient dependent yield criterion. *in Key Engineering Materials*. 2003. *Trans Tech Publ*.

28. Kim, Y.-S., S.-Y. Won, and K.-H. Na, Effect of material damage on forming limits of voided anisotropic sheet metals. *Metallurgical and Materials Transactions A*, 2003. 34(6): p. 1283-1290.

29. Monchiet, V., et al., Macroscopic yield criteria for plastic anisotropic materials containing spheroidal voids. *International Journal of Plasticity*, 2008. 24(7): p. 1158-1189.

30. Pastor, F., J. Pastor, and D. Kondo, Limit analysis of hollow spheres or spheroids with Hill orthotropic matrix. *Comptes Rendus Mécanique*, 2012. 340(3): p. 120-129.

31. Morin, L., et al., A new technique for finite element limit-analysis of Hill materials, with an application to the assessment of criteria for anisotropic plastic porous solids. *International Journal of Engineering Science*, 2014. 74: p. 65-79.

32. Morin, L., J.-B. Leblond, and D. Kondo, A Gurson-type criterion for plastically anisotropic solids containing arbitrary ellipsoidal voids. *International Journal of Solids and Structures*, 2015. 77: p. 86-101.

33. Paux, J., et al., An approximate yield criterion for porous single crystals. European *Journal of Mechanics-A/Solids*, 2015. 51: p. 1-10.

34. Keralavarma, S. and S. Chockalingam, A criterion for void coalescence in anisotropic ductile materials. *International Journal of Plasticity*, 2016. 82: p. 159-176.

35. Aravas, N., On the numerical integration of a class of pressure-dependent plasticity models. *International Journal for numerical methods in engineering*, 1987. 24(7): p. 1395-1416.

36. Mühlich, U., W. Brocks, and T. Siegmund, A User-material Subroutine of the Modified Gurson-Tvergaard-Needleman-model of Porous Metal Plasticity for Rate and Temperature Dependent Hardening. 2000: *Inst. für Werkstofforschung, GKSS-Forschungszentrum*.

37. Gologanu, M., J.-B. Leblond, and J. Devaux, Approximate models for ductile metals containing non-spherical voids—case of axisymmetric prolate ellipsoidal cavities. *Journal of the Mechanics and Physics of Solids*, 1993. 41(11): p. 1723-1754.

38. Son, H.S. and Y.S. Kim, Prediction of forming limits for anisotropic sheets containing prolate ellipsoidal voids. *International journal of mechanical sciences*, 2003. 45(10): p. 1625-1643.

39. Slimane, A., et al., Parametric study of the ductile damage by the Gurson–Tvergaard–Needleman model of structures in carbon steel A48-AP. *Journal of Materials Research and Technology*, 2015. 4(2): p. 217-223.

40. Gullerud, A.S., et al., Simulation of ductile crack growth using computational cells: numerical aspects. *Engineering Fracture Mechanics*, 2000. 66(1): p. 65-92.

41. Nielsen, K.L. and J.W. Hutchinson, Cohesive traction–separation laws for tearing of ductile metal plates. *International Journal of Impact Engineering*, 2012. 48: p. 15-23.

42. Jiang, W., Y. Li, and Y. Shu. Analysis of Metallic Ductile Fracture by extended Gurson models. *in ICF13*. 2013.

43. Ghosh, S., M. Li, and A. Khadke, 3D modeling of shear-slitting process for aluminum alloys. *Journal of Materials Processing Technology*, 2005. 167(1): p. 91-102.

44. Kossakowski, P. and W. Wciślik, Experimental determination and application of critical void volume fraction fc for S235JR steel subjected to multi-axial stress state. *Recent Advances in Computational Mechanics*, 2014. 303: p. 309.

45. Wcislik, W., Experimental determination of critical void volume fraction f F for the Gurson Tvergaard Needleman (GTN) model. *Procedia Structural Integrity*, 2016. 2: p. 1676-1683.

46. Kossakowski, P., Experimental determination of the void volume fraction for S235JR steel at failure in the range of high stress triaxialities. *Archives of Metallurgy and Materials*, 2017. 62(1): p. 167-172.

47. Abaqus/6.9 Software, Abaqus Analysis User's Manual (6.9), Porous metal plasticity; 2009.

48. Springmann, M. and M. Kuna, Identification of material parameters of the Gurson–Tvergaard–Needleman model by combined experimental and numerical techniques. *Computational Materials Science*, 2005. 32(3): p. 544-552.

49. Cuesta, I., J. Alegre, and R. Lacalle, Determination of the Gurson–Tvergaard damage model parameters for simulating small punch tests. *Fatigue & fracture of engineering materials & structures*, 2010. 33(11): p. 703-713.

50. Bernauer, G. and W. Brocks, Micro-mechanical modelling of ductile damage and tearing–results of a European numerical round robin. *Fatigue & Fracture of Engineering Materials & Structures*, 2002. 25(4): p. 363-384.

51. Brunet, M. and F. Morestin, Experimental and analytical necking studies of anisotropic sheet metals. *Journal of Materials Processing Technology*, 2001. 112(2): p. 214-226.

52. Thuillier, S., N. Le Maoût, and P.-Y. Manach, Influence of ductile damage on the bending behaviour of aluminium alloy thin sheets. *Materials & Design*, 2011. 32(4): p. 2049-2057.

CHAPTER 4

Study of influence of superimposed hydrostatic pressure on bendability of sheet metals

Complete citation:

XXXXXXXXXXXXX

Copyrights:

Relative contributions:

M.M. Shahzamanian: Performed all the simulations, interpretation and analysis of the data, wrote the first draft of the manuscript including all figures and text and was responsible for the final draft submittal to the journal.

D.J. Lloyd: Revised and modified the journal paper draft

P.D. Wu: supervisor of M.M.Shahzamanian, revised and modified the journal paper draft.

Zhutian Xu: Provided the VUMAT GTN model to analyze the stress based void nucleating.

ABSTRACT

The effect of superimposed hydrostatic pressure on the bendability of sheet metal is investigated using the finite element method employing the Gurson-Tvergaard-Needleman (GTN) model. It is shown that bendability and fracture strain increase significantly by imposing hydrostatic pressure as it delays the growth and coalescence of microvoids but it has insignificant effect on void nucleation using the GTN model, which is strain controlled for void nucleating. Furthermore, the effect of superimposed hydrostatic pressure on tensile test simulation under plane strain state is investigated and the predicted fracture strains are compared with those corresponding to bending tests. It is demonstrated that ductility under various superimposed hydrostatic pressures for bending test are higher than those predicted in tensile tests. Lastly, the sensitivity of ductile fracture parameters in the GTN model on bendability is considered. Numerical results are found to be in good agreement with experimental observations.

Keywords: Superimposed hydrostatic pressure; Bendability; Fracture; Finite element analysis (FEA).

4.1. Introduction

Bending is an important deformation mode in many applications and it is an important property in a range of applications and extensively used in the auto industry [1,2]. The

bending properties of various materials has been studied in [3-5]. Mechanical performance of materials can be studied via the three-point bending test [6-8]. On the other hand, a superimposed hydrostatic pressure has been proven to increase tensile ductility as it delays void growth and coalescence [9]. However, to the best of our knowledge, the effect of a superimposed hydrostatic pressure on bendability is not considered in detail elsewhere.

Different types of fracture mechanisms, such as brittle, fully plastic, ductile and shear fractures are explained by Ashby et al. [9] and it is stated that the fracture mode changes under a superimposed hydrostatic pressure or temperature. Herein, fully plastic failure happens if all other fracture mechanisms are suppressed. The material starts to neck and strain localizes in the necked region and consequently with further continuing strain the section reduces to a point of zero area. Such a failure mode can happen under superimposed hydrostatic pressure when void growth and nucleation are suppressed. The effect of superimposed hydrostatic pressure on void formation in the tensile test was characterized using quantitative metallography and the fracture mechanism is analyzed through fractography in [10]. It was observed that a significant increase in ductility occurs with the suppression of microvoid development, while the flow stress change is negligible. It is shown in [10] that externally applied pressure excludes the void-sheet mechanism leaving shear decohesion as the dominant failure mechanism since it is not very sensitive to hydrostatic pressure. In this way, a cup-and-cone mode of fracture under atmospheric pressure changes to a slant fracture under high superimposed hydrostatic pressure. The effect of superimposed hydrostatic pressure on the bending fracture strain of low carbon steel containing globular sulfides was studied by Kao et al. [11]. It was found that a

superimposed hydrostatic pressure increased the fracture strain and it enhanced the bendability significantly. The experimental results presented in [11] show that the fracture is due to the nucleation, growth and coalescence of voids and a superimposed hydrostatic pressure delays or completely eliminates the nucleation, growth and coalescence of voids which results in increased fracture strain and bendability. Weinrich and French investigated the effect of superimposed hydrostatic pressure on the fracture mechanisms of sheet tensile specimens [12]. They found that the mode of fracture at room pressure is smooth and it is planar (P-type) and it changes to chisel-edge without any void sheet (C-type) with increase of hydrostatic pressure. Overall, it is generally accepted that a superimposed hydrostatic pressure increases ductility as it delays or completely eliminates the void growth and nucleation [13-18].

Wu et al. [19] studied the effect of superimposed hydrostatic pressure on the formability of sheet metal by constructing the forming limit diagram (FLD) based on the M-K approach and it was found that pressure delayed the initiation of necking and the formability increased. Furthermore, transition of the fracture surface in a tensile round bar from cup-cone mode under atmospheric pressure to a slant structure under high pressure is numerically reproduced employing the GTN model. Peng et al. [20] investigated the effect of superimposed hydrostatic pressure on fracture in round bars. First, they showed that a superimposed pressure has no noticeable effect on the necking strain as void formation was not significant prior to necking. The numerical results showed that the fracture strain increased due to the fact that a superimposed pressure delayed or eliminated void nucleation and growth completely. The fracture surface changes from a cup-cone

mode under atmospheric pressure to a slant smooth surface under high pressure. It was observed that a superimposed pressure not only increased the fracture strain but also extended the failure process. The effect of superimposed pressure on fracture in sheet metals under tension was studied in [21] and again it was found that a hydrostatic pressure increased the ductility in sheet metal and numerical results show the transition of fracture surface from P-type mode at atmospheric pressure to C-type mode under high pressure as observed experimentally. Lastly, in [22], the effect of a superimposed hydrostatic pressure on bendability was investigated numerically and it was found that a hydrostatic pressure increased the fracture strain.

The aim of this study is to perform a numerical study of the effect of a superimposed hydrostatic pressure on fracture in sheet metal under three-point bending. All the simulations presented in this study are performed using ABAQUS/Explicit [23] based on the GTN model. The effect of hydrostatic pressure on the three-point bending test is explained in detail and the sensitivity of ductile fracture parameters in the GTN model under various hydrostatic pressures are discussed. Numerical results are found in good agreement with experimental observations presented in [11].

4.2. Constitutive model

The Gurson-Tvergaard-Needleman (GTN) model [24-27] is used in this study which is on the basis of damage growth in metals due to nucleation, void growth and coalescence and

this model was originally developed by Gurson [28]. The void growth is a function of the plastic strain rate $\mathbf{D}^P$:

$$\left(\dot{f}\right)_{\text{growth}} = (1-f)\mathbf{I}\colon \mathbf{D}^{P} \tag{1}$$

And the void nucleation is assumed to be strain controlled as following:

$$\left(\dot{f}\right)_{\text{strain controlled nucleation}} = \bar{A}\dot{\bar{\varepsilon}}^{P} \tag{2}$$

where $\dot{\bar{\varepsilon}}^P$ is the effective plastic strain rate, and the parameter $\bar{A}$ is chosen so that nucleation follows a normal distribution as suggested by Chu and Needleman [29]:

$$\bar{A} = \frac{f_N}{S_N\sqrt{2\pi}}\exp\left[-\frac{1}{2}\left(\frac{\bar{\varepsilon}^{p}-\varepsilon_N}{S_N}\right)^2\right] \tag{3}$$

here, ε_N is the average void nucleating strain, f_N is the volume fraction of void nucleating particles, S_N is the standard deviation of void nucleating strain. It is to be noted that in ABAQUS, only strain controlled void nucleation is considered and the stress controlled void nucleation is not available. In order to implement a void nucleation to be stress controlled GTN model in ABAQUS, one must use UMAT/VUMAT subroutine. However, assuming void nucleation to be stress controlled we have [30]:

$$\left(\dot{f}\right)_{\text{stress controlled nucleation}} = B\left(\dot{\bar{\sigma}} + \frac{1}{3}c\dot{\sigma}_H\right) \tag{4}$$

where, B is taken to depend on the current stress state value of the matrix equivalent plastic strain.

$$B = \frac{f_N}{S_N\sigma_y\sqrt{2\pi}}\exp\left[-\frac{1}{2}\left(\frac{\bar{\sigma}+c\sigma_H-\sigma_N}{S_N\sigma_y}\right)^2\right] \tag{5}$$

σ_N is the average nucleation stress and c is a redundant factor for hydrostatic pressure and it takes values between 0.3 and 0.4 [31-32].

The growth of existing voids and the nucleation of new voids are considered in the evolution of void volume fraction as follows:

$$\dot{f} = (\dot{f})_{growth} + (\dot{f})_{nucleation} \tag{6}$$

and the function of void volume fraction ($f^*(f)$) is defined to consider coalescence as follows:

$$f^* = \begin{cases} f & \text{for } f \le f_c \\ f_c + \frac{f_u^* - f_c}{f_f - f_c}(f - f_c) & \text{for } f > f_c \end{cases} \tag{7}$$

where f_c is the critical void volume fraction when coalescence happens and f_f is the void volume fraction at failure. Lastly, the parameter $f_u^* = \frac{1}{q_1}$ is defined. It should be mentioned that void growth and nucleation does not happen when the stress state of an element is compressive in ABAQUS and void growth and nucleation only happen in tension.

Finally, the approximate yield function to be used in which f^* is distributed randomly is as follows:

$$\Phi(\boldsymbol{\sigma}, \bar{\sigma}, f) = \frac{\sigma_e^2}{\bar{\sigma}^2} + 2f^* q_1 \cosh\left(\frac{3q_2\sigma_H}{2\bar{\sigma}}\right) - [1.0 + (q_1 f^*)^2] = 0 \tag{8}$$

where, $\boldsymbol{\sigma}$ is the macroscopic Cauchy stress tensor and σ_e, σ_H and $\bar{\sigma}$ are equivalent stress, hydrostatic stress and matrix stress, respectively. Also, q_1 and q_2 are the calibrated parameters.

The uniaxial elastic-plastic undamaged stress-strain curve for the matrix material is provided by the following power-law form:

$$\bar{\varepsilon} = \begin{cases} \frac{\bar{\sigma}}{E}, & \text{for } \bar{\sigma} \leq \sigma_y \\ \frac{\sigma_y}{E}\left(\frac{\bar{\sigma}}{\sigma_y}\right)^n, & \text{for } \bar{\sigma} > \sigma_y \end{cases} \tag{9}$$

4.3. Problem formulation and method of solution

The schematic presentation of a sheet metal under pressure with length L_o and thickness t_o is considered and shown in Figure 4.1. It is assumed that the sheet is wide enough with no deformation in width direction to consider the plane strain state. Rigid bodies are considered for both punch and mandrel with radii R_p and R_m, respectively. The mandrel is stationary with a length span L_m when the punch applies a force in the middle section of the sheet. The superimposed hydrostatic pressure is shown with arrows. The sequence of plane strain three-point bending under superimposed hydrostatic pressure is modeled as two steps. In the first step, the pressure is applied gradually up to a desired level $p = -\alpha\sigma_y$ without applying any force by the punch and in the second step, the punch applies force to the sheet at the constant pressure value of $p = -\alpha\sigma_y$.

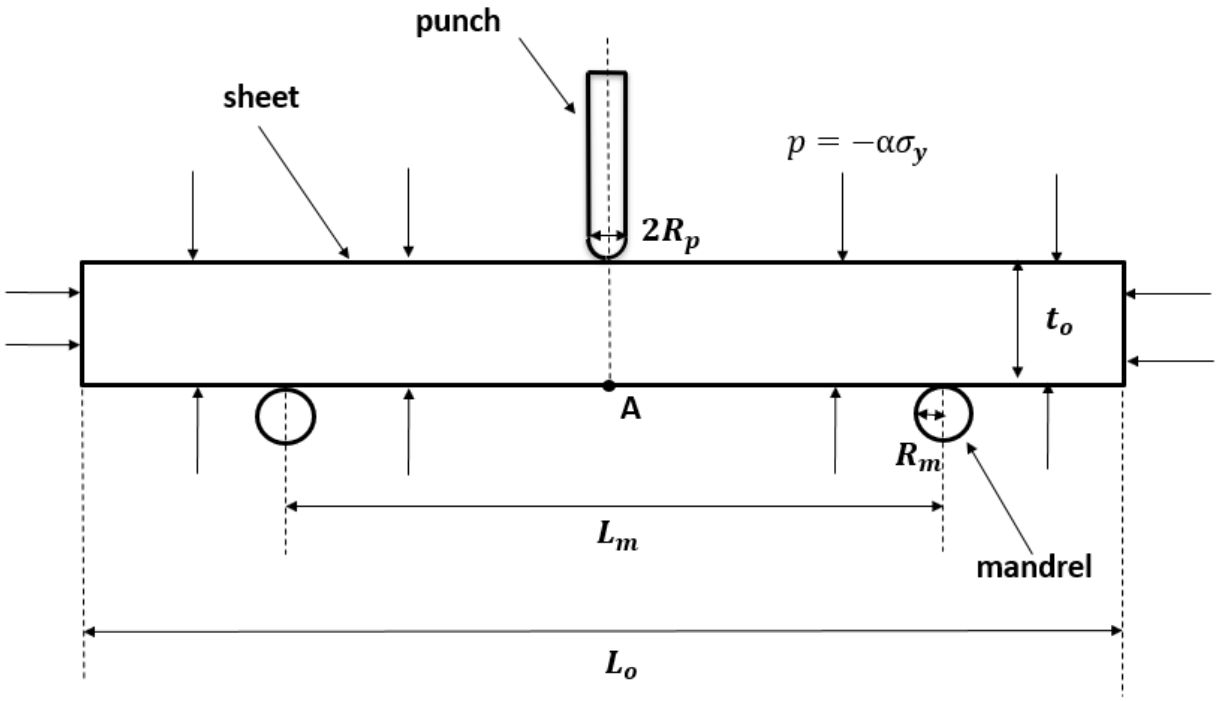

Figure 4. 1. Schematic of three-point bending test of a sheet metal under hydrostatic superimposed pressure

4.4. Results and discussion

The elastic-plastic properties of the matrix material is specified by $\sigma_y/E = 0.0033, \nu = 0.3$ and $n = 10$. It is assumed that the initial void volume fraction is zero and the fit parameters in the GTN model (Equation (8)) are $q_1 = 1.5$ and $q_2 = 1.0$. Void nucleation is assumed to be plastic strain controlled with the volume fraction $f_N = 0.04$ of void nucleating particles, the mean strain for nucleation is $\varepsilon_N = 0.3$, and the corresponding standard deviation is $S_N = 0.1$. The final failure is taken to be characterized by the parameters $f_c = 0.15$ and $f_f = 0.25$. Theses values of mechanical properties are taken

from Tvergaard and Needleman [24]. It should be emphasized that the main purpose of the present study is to assess the effect of superimposed hydrostatic pressure on the bendability of sheet metals, and that the overall results and conclusions are not particularly dependent on the above values of the material parameters. However, a parametric study on ductile fracture parameters in the GTN model was performed under various superimposed hydrostatic pressure to understand the effect of each parameter.

The Penalty contact method is used for the interaction between sheet and mandrels as well as punch. Contact pair interactions are defined by specifying each of the individual surface pairs that can interact with each other which searches for node-into-face and edge-into-edge penetrations in the current configuration. The sheet metal is considered to be under plane strain three-point bending. Therefore, plane strain quadrilateral element CPE4R in ABAQUS/Explicit is considered for the sheet. Also, rigid body element R2D2 is considered for the punch and mandrels. Length of sheet (L_o), thickness (t_o) and plane strain thickness are 20 mm, 2.5 mm and 10 mm, respectively. Also, R_m, R_p and L_m are 0.25 mm, 0.2 mm and 13 mm, respectively.

As mesh sensitivity is expected in numerical simulations involving localized deformation and fracture, different meshes are considered in this simulation. Figure 4.2 shows the FE configuration of three-point bending test with a typical mesh for metal sheet consisting of 60×110 plane strain quadrilateral elements (CPE4R) in which the element distribution in the refined area is biased to the middle section of the specimen where fracture is expected to occur. The effect of mesh sensitivity on fracture bending strain will be discussed later

in this section. Due to the symmetry, only half of the sheet is investigated and symmetric boundary conditions are imposed in the middle section of specimen.

Although three-point bending test is a static analysis, ABAQUS/Explicit is used as ABAQUS/Standard is not able to provide failure in the GTN model. However, the mass scaling method with sufficient low target time increment is used and it is carefully attempted to minimize the dynamic effect of the sample. It is to be noted that the results of ABAQUS/Explicit are comparable well with those obtained using ABAQUS/Standard before initiation of failure as shown in Figure 4.3.

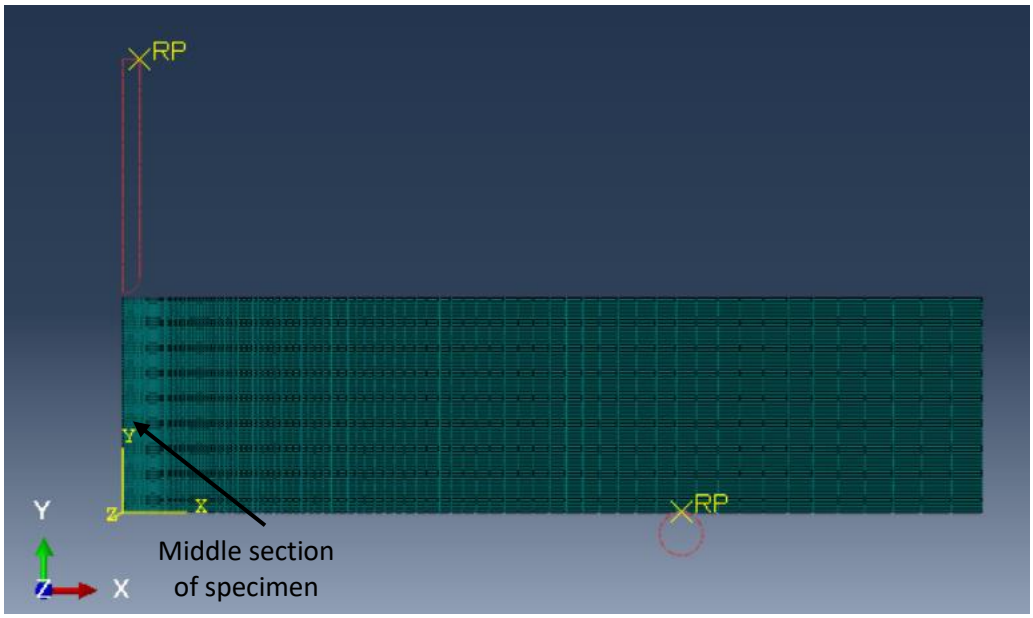

Figure 4. 2. FE configuration of three-point bending test; A typical mesh for metal sheet with 60×110 quadrilateral elements (CPE4R in ABAQUS/Explicit)

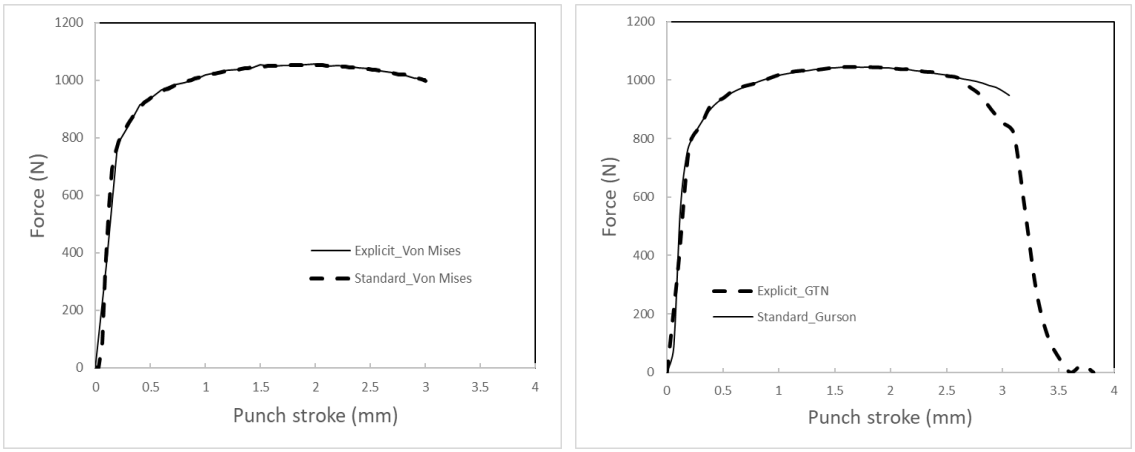

Figure 4. 3. Results comparison between ABAQUS/Explicit and ABAQUS/Standard

Figure 4.4 represents the punch force F as a function of the punch stroke δ at room pressure $(\alpha = 0)$ and the effect of mesh sensitivity on the force-displacement curve is also included. Initially the load increases linearly with a very small amount of punch movement and the sheet is essentially in the elastic state. Then the load increases gradually and reaches its maximum followed by a gradually decrease with continued increase in the punch stroke. Further punch movement results in a sharp "knee" on the load and punch stroke curve which is associated with reaching the critical value of the void volume fraction (f_c) at the outer surface of the specimen in the middle section which is under tension. Immediately after the sharp knee, a burst of void growth and nucleation leads to a rapid drop in punch force, indicating a rapid loss of load carrying capacity for the sheet sample. Two different meshes of 60×110 elements (60 elements in Y direction and 110 elements in X direction) and 100×150 elements (100 elements in Y direction and 150 elements in X direction) are investigated and the effect of mesh sensitivity on the force-displacement curves are shown in Figure 4.4. These two meshes are very carefully designed to have the aspect ratio close

to 1.0 in the middle section of specimen where fracture occurs. It is observed that mesh size has a insignificant effect on the initiation of fracture.

It is to be mentioned that in the numerical study of effects of the superimposed hydrostatic pressure on fracture of sheet metals under plane strain tension, Wu et al. [21] stated that two crossed shear bands, symmetric to the middle plane are developed after onset of necking. Fracture initiates at the center of the neck, where the two shear bands cross each other and where the maximum stress triaxiality is expected to occur. Due to the initial symmetry, it is expected that cracks will be developed and propagated along the crossed shear bands. However, the initial symmetry cannot be retained. Instead, the simulations result in a nonsymmetric solution with a single crack as it dissipates less energy. The selection of the single crack is however due to numerical round-off errors, which are sensitive to the mesh used. In the present study, it was found that the difference in the predicted initiation of fracture from the symmetric solution and non-symmetric solution is very small, although the two solutions predict very different patterns of crack propagation. On the other hand, it is to be noted that the calculated subtle change in appearance of crack pattern due to the superimposed hydrostatic pressure can be very sensitive to the mesh used and may even be an artefact of the mesh, regardless of symmetric or non-symmetric assumption is applied. Nevertheless, it should be emphasized again that the main purpose of this study is to assess the influence of the superimposed hydrostatic pressure on the bendability, and that the overall results and conclusions are not particularly dependent on the symmetry assumption considered as well.

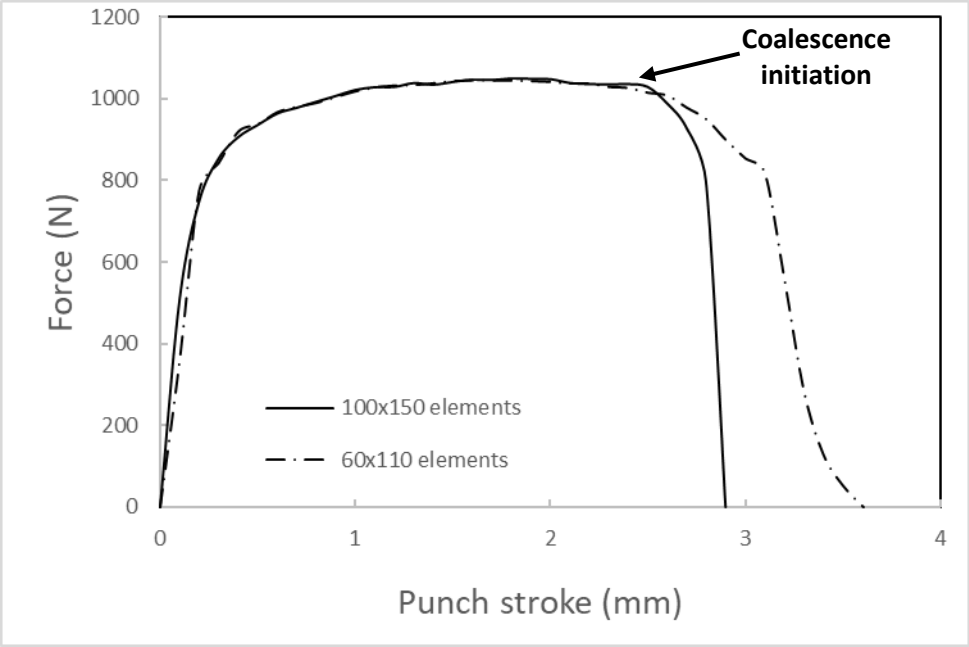

Figure 4. 4. Effect of mesh sensitivity on force-displacement curve at room pressure ($\alpha = 0$)

4.4.1. Superimposed hydrostatic pressure effect in bending test

The effect of a superimposed hydrostatic pressure ($p = -\alpha\sigma_y$) on fracture under plane strain three-point bending test is studied. Figure 4.5 shows the effect of α on force-displacement curve and it is found that the maximum force does not change but the hydrostatic pressure delays the sharp knee on force-displacement curve. At a relatively high pressure $p = -0.4\sigma_y$, the force decreases more gradually than those under lower applied pressures and fracture does not occur at pressure higher than $p = -0.4\sigma_y$.

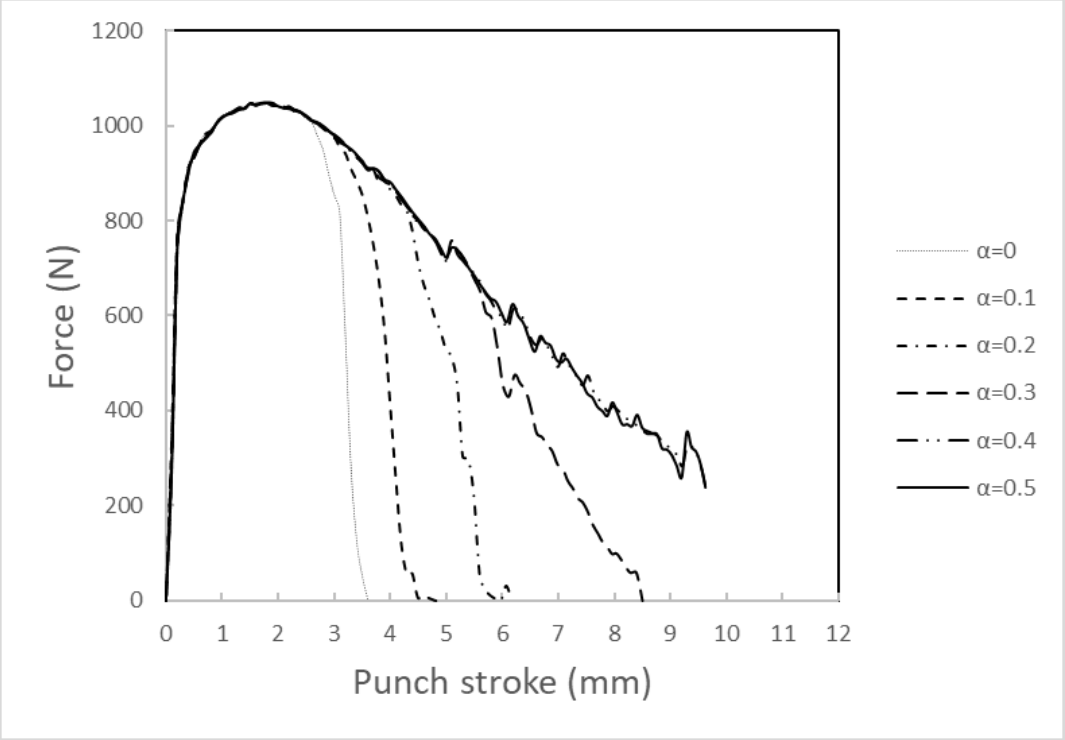

Figure 4. 5. Effect of superimposed hydrostatic pressure on force-displacement curve

Figure 4.6 presents the crack patterns in sheet metals under various superimposed hydrostatic pressures. It is shown that crack propagates from the outer surface along the middle section of the specimen at room pressure and under a pressure $p = -0.1\sigma_y$ but it propagates in a zig-zag shape as shown in Figure 4.6(c and d) under pressures $p = -0.2\sigma_y$ and $p = -0.3\sigma_y$. It is to be noted that the crack shapes in the latter cases were investigated using finer meshes and the same patterns were obtained.

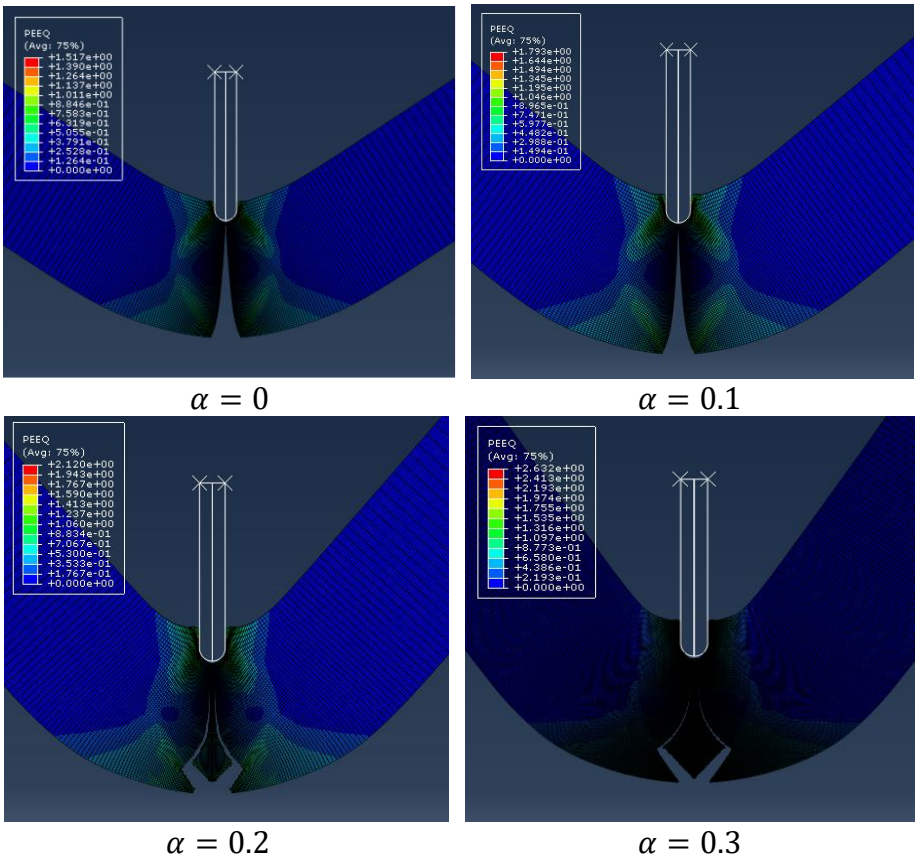

Figure 4. 6. Crack shapes of sheet metals under various superimposed hydrostatic pressures

As mentioned in [33], bendability in wrap bend testing is defined by the parameter $\frac{r}{t}$ where r is the minimum radius of mandrel that the specimen is bent around without appearance of fracture on the outer surface of specimen and t is the specimen thickness. Also, Kao et al. in [11, 13] presented a forming limit diagram obtained from bending test with specimens having various width/thickness ratios. The major and minor strains in [11, 13] are calculated at the initiation of fracture on the outer surface of specimen. However, the effect of superimposed hydrostatic pressure on normalized minimum cross-sectional area

$\left(\frac{A_{min}}{A_o}\right)$ and bending fracture strain $\left(\varepsilon_f^c\right)$ in the middle section of the specimen are shown in Figure 4.7. Here, the bending fracture strain ε_f^c is defined as $\varepsilon_f^c = \ln\frac{A_o}{A_{min}}$ calculated in the middle section of the specimen. A_{min} is the minimum cross-sectional area of sheet which is calculated one step right before fracture initiation in ABAQUS. It is found that the minimum cross-sectional area decreases with increasing the hydrostatic pressure and it allows the specimen to deform more and it increases the ductility and bending fracture strain.

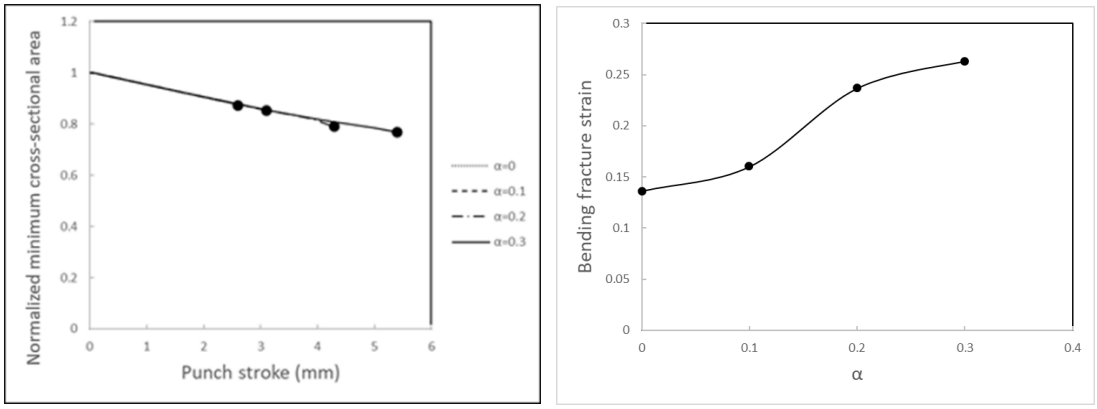

(a) Normalized minimum cross-sectional area (b) Bending fracture strain

Figure 4. 7. Predicted (a) normalized minimum cross-sectional area and (b) bending fracture strain for various values of α

The delay of fracture can be explained by showing how a superimposed hydrostatic pressure $p = -\alpha\sigma_y$ affects the hydrostatic pressure and stress triaxiality in the middle section of specimen which results in delaying or completely eliminating void growth. Figure 4.8 presents the hydrostatic pressure $\sigma_H = (1/3)\left(\sigma_{xx} + \sigma_{yy} + \sigma_{zz}\right)$ and stress

triaxiality $\frac{\sigma_H}{\bar{\sigma}}$ at point A (see Figure 4.1) where fracture initiates as a function of punch stroke under various superimposed hydrostatic pressures. At room pressure $p = 0$, both hydrostatic pressure and stress triaxiality develops in a way to assist the void growth but hydrostatic pressure (σ_H) and stress triaxiality are initially compressive under a superimposed hydrostatic pressure $p = -\alpha\sigma_y$. This implies that void growth is delayed until a sufficiently large tensile component of stress is introduced.

The effect of superimposed double-sided pressure on the formability of biaxially stretched AA6111-T4 sheet metal was studied in [34] numerically employing the GTN model and it was found that double-sided pressure increased formability while void nucleation is invariable and only the void growth changes, decreasing with an increase of pressure. Figure 4.9(a) shows the effect of superimposed hydrostatic pressure on void nucleation, void growth and total volume fraction. It is shown that superimposed hydrostatic pressure has no effect on void nucleation as the GTN model used in this study assumes that the nucleation is strain controlled (Equations 2-3), and hydrostatic pressure is not involved in void nucleation. However, the effect of superimposed hydrostatic pressure on void growth is shown in Figure 4.9(b) and it is clearly observed that hydrostatic pressure delays or completely eliminates the void growth. Figure 4.9(c) shows the total void volume fraction under various superimposed hydrostatic pressures. In this study, the GTN model available in ABAQUS is used when the void nucleation is strain controlled. However, the effect of superimposed hydrostatic pressure on stress controlled void nucleation is studied and discussed later in subsection 4.3 using a subroutine in ABAQUS.

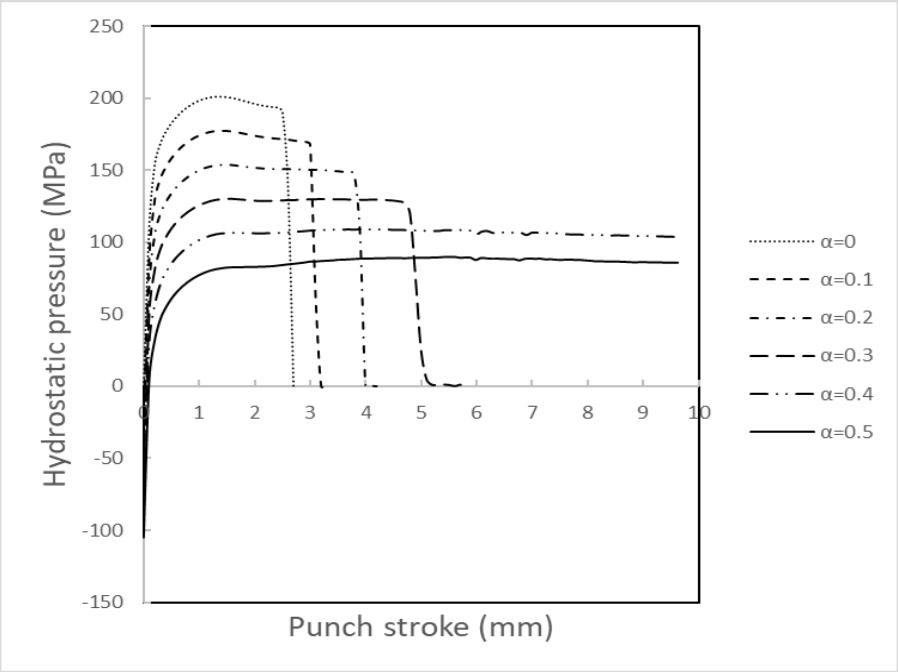

(a) Hydrostatic pressure

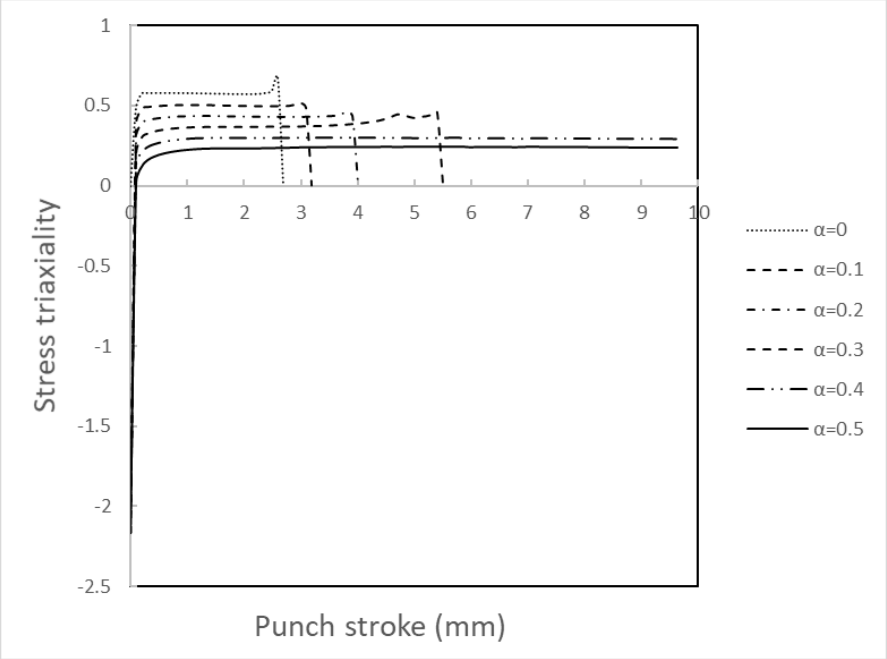

(b) Stress triaxiality

Figure 4. 8. Effect of superimposed hydrostatic pressure on (a) hydrostatic pressure and (b) stress triaxiality at point A

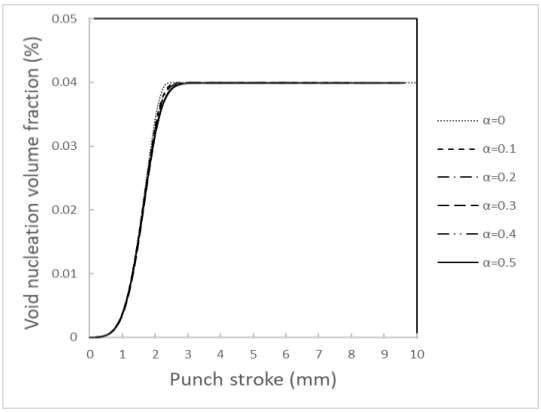

(a) Void nucleation volume fraction

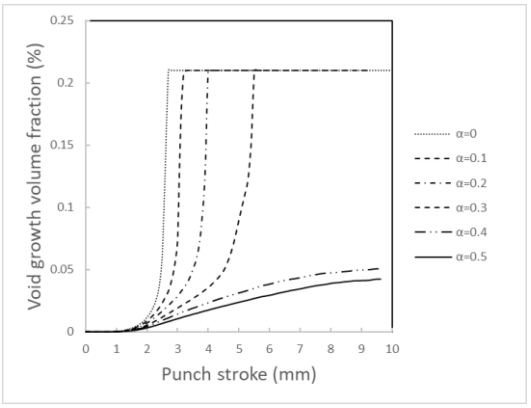

(b) Void growth volume fraction

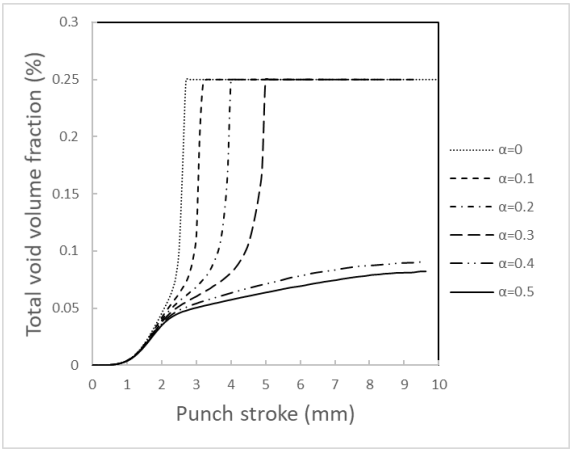

(c) Total void volume fraction

Figure 4. 9. Predicted (a) void nucleation volume fraction, (b) void growth volume fraction and (c) total void volume fraction at point A for various values of α

The effect of mesh sensitivity on the force-displacement curve at room pressure was shown in Figure 4.4. As mentioned previously, the results of this study are presented corresponding to a mesh with 60×110 elements and Figure 4.7(b) presents the ε_f^c under various superimposed hydrostatic pressure. The effect of mesh sensitivity on ε_f^c is shown in Figure 4.10(a). It is observed that ε_f^c at room pressure are almost similar. Although ε_f^c are nearly similar for two meshes when α=0.3, mesh sensitivity increases with increasing

hydrostatic pressure. The gain in ductility for these two meshes is shown in Figure 4.10(b). It is to be noted that the percentage change of ε_f^c under superimposed pressure relative to ε_f^c at room pressure is defined as a gain in ductility in Figure 4.10(b).

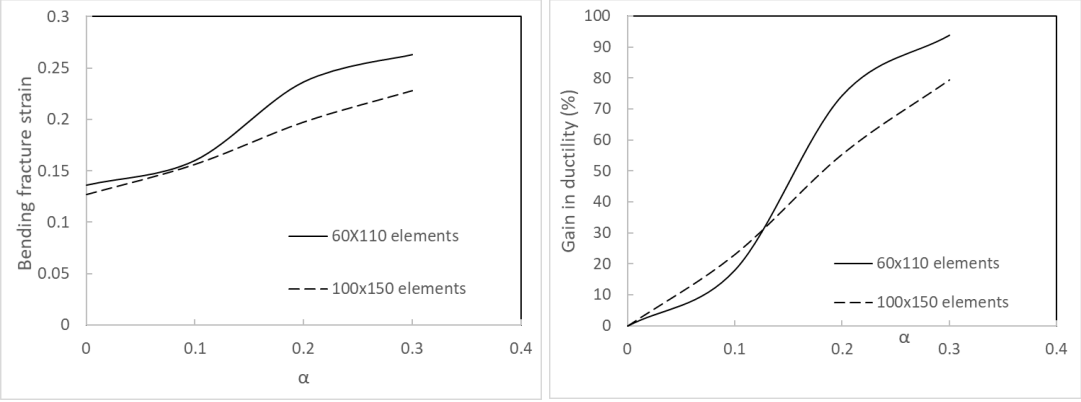

(a) Bending fracture strain (b) Gain in ductility

Figure 4. 10. Effect of mesh sensitivity on (a) bending fracture strain and (b) gain in ductility

4.4.2. Fracture strain comparison in tensile and bending tests

As shown in [21], mesh size has a significant effect in the prediction of fracture strain in sheet metal under tension with various superimposed hydrostatic pressures. It is to be noted that the fracture strain is calculated when complete fracture happens in [21]. It was found that mesh size has little influence on the fracture strain when the superimposed hydrostatic pressure is close to zero, but the mesh sensitivity increases with increasing superimposed hydrostatic pressures. The situation for deformation under bending to calculate the ε_f^c at the initiation of fracture is comparable.

Figure 4.11 shows the schematic and FE configuration of a tensile test under plane strain state with a typical mesh consisting of 100×150 plane strain quadrilateral elements (CPE4R) in which the element distribution in the refined area is biased to the middle section of the specimen where fracture is expected to occur. A rather stubby specimen is considered since only the neck region is concerned. The length of the tensile specimen is three times the initial thickness of the tensile sample, as simulated in [21]. In Figure 4.11(a), the superimposed hydrostatic pressure is shown with thin arrows and applied strains are shown with thick arrows. In this study, the fracture strain for tensile test is calculated one step right before the initiation of fracture in ABAQUS.

Fracture is initiated at the center of specimen in the tensile test and then it propagates toward the surfaces along the generated shear bands as reported in [10, 20]. Figure 4.12 shows the shear bands before and after fracture in tensile test specimen. As mentioned in [1], the failure mechanism in bending is different from that in the tensile test. It is to be noted that the material points considered in the two tests experience very different loading histories and, thus the results are not directly comparable. In the bend test, strain localizes in severe bands often associated with grain boundaries close to the outer surface of specimen which is a free and unconstrained surface and strain decreases with strain gradient through the thickness of the sample to the neutral axis and cracks form on the outer surface of specimen. Furthermore, the surface strain developed in the bend test can be larger than in tensile deformation [1]. Tensile failure initiates at the uniaxial tensile strength (UTS) when a geometrical instability, that is a neck, is initiated and at this stage triaxial stresses develop in the neck promoting void nucleation and growth. On the

contrary, geometrical necking does not occur under bending due to the developed gradient of strain. Thus, global triaxiality is absent in bending. In fact, only local stress triaxiality associated with microstructure is generated. So significant cracks have formed at the surface of the bend sample long before bend sample fracture occurs. The experiments presented in [35-36] evident that the fracture strain and equivalent plastic strain at failure obtained from bending test are higher than those obtained from tensile test. Figure 4.13 shows the effective plastic strain one step right before the initiation of fracture for both bending and tensile tests. The results are obtained at the center of the tensile test specimen and at the outer surface in the middle section of bending specimen where fracture is expected to occur, fracture initiates at Point A as shown in Figure 4.1. It is clearly shown in Figure 4.13 that ductility is higher in the bend test than those obtained in the tensile test for various superimposed pressures.

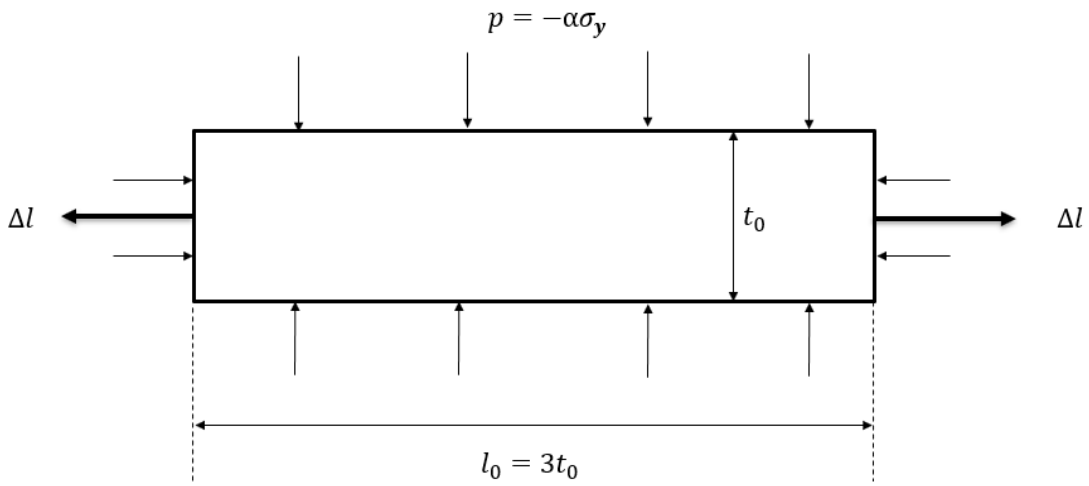

(a) Schematic

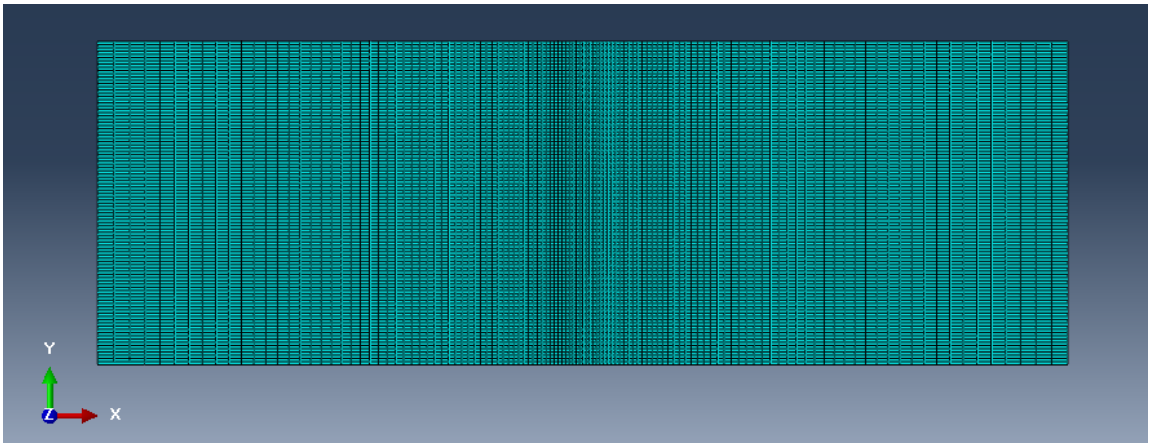

(b) FE configuration

Figure 4. 11. Tensile test specimen; (a) schematic and (b) FE configuration with a typical mesh with 100×150 quadrilateral elements (CPE4R in ABAQUS/Explicit)

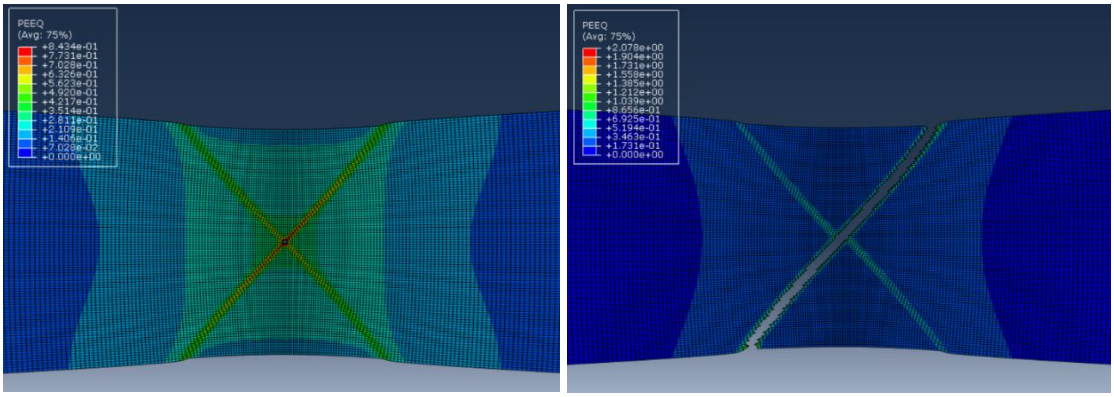

(a) (b)

Figure 4. 12. Developed shear bands in tensile test specimen; (a) before fracture (b) after fracture

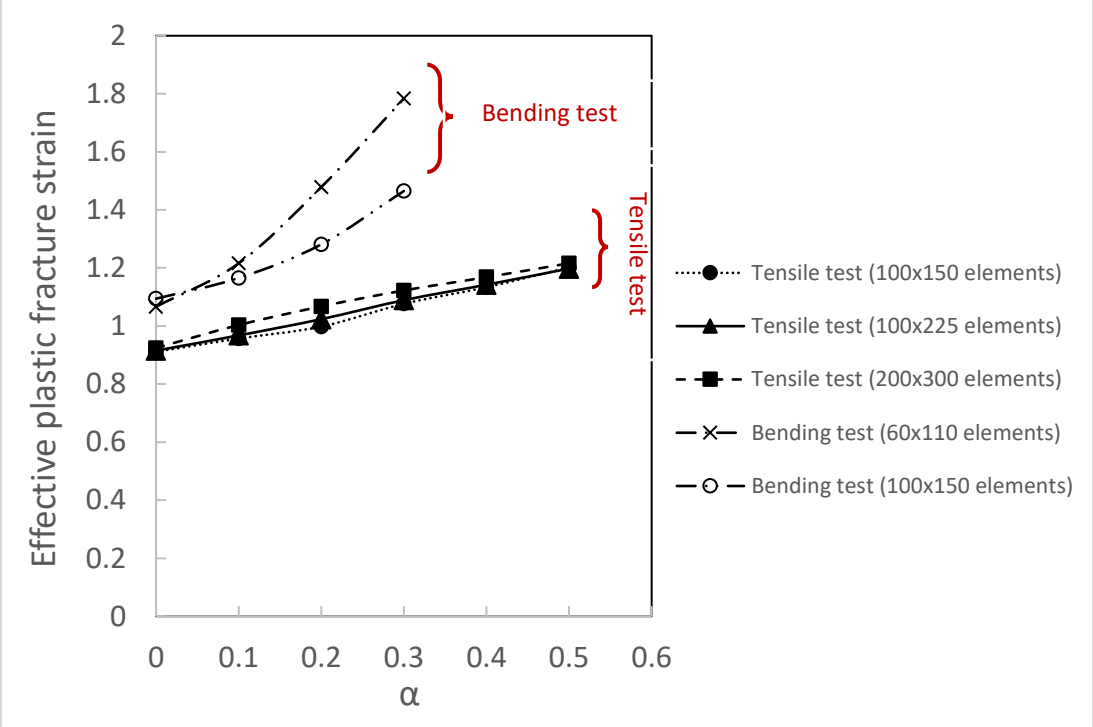

Figure 4. 13. Effective plastic fracture strain in bending and tensile tests

4.4.3. Stress controlled void nucleation

As mentioned previously, in ABAQUS only strain controlled void nucleation is considered and stress controlled void nucleation is not available. As shown in Figure 4.9(a), the nucleated void volume fraction is unchanged under various superimposed hydrostatic pressures. In order to study the effect of hydrostatic pressure on void nucleation when it is stress controlled, the GTN model is implemented via a VUMAT subroutine in which stress controlled void nucleation is considered. This subroutine only supports three-dimensional elements.

A very wide specimen (width=100 mm) is considered to simulate the plane stain condition. However, this condition is not fully plane strain and it causes a reduction in the fracture strain as the width/thickness of the specimen decreases [37]. A low L_m (=10 mm) is considered to increase the fracture strain as the fracture strain increases with a decrease of L_m [8]. The stress controlled void nucleation volume fraction, void growth and total volume fractions are shown in Figure 4.14. $\sigma_N = 610\ MPa$ and $c = 0.35$ are assumed for this study. Fracture occurs when $\alpha = 0.1$ and it does not happen beyond this value. Results show that a hydrostatic pressure delays both void nucleation and void growth, contrary to strain controlled void nucleation when only void growth is delayed.

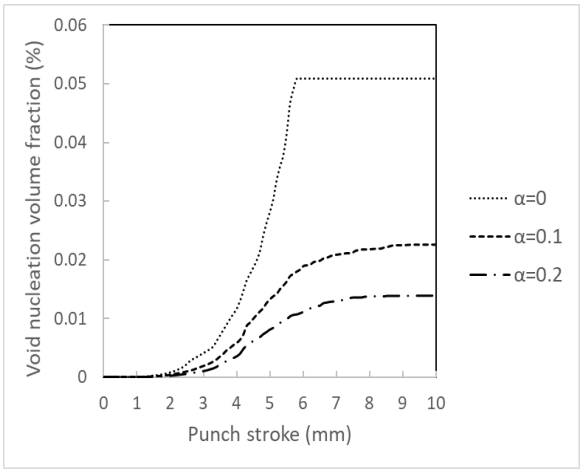

(a) Stress controlled void nucleation volume fraction

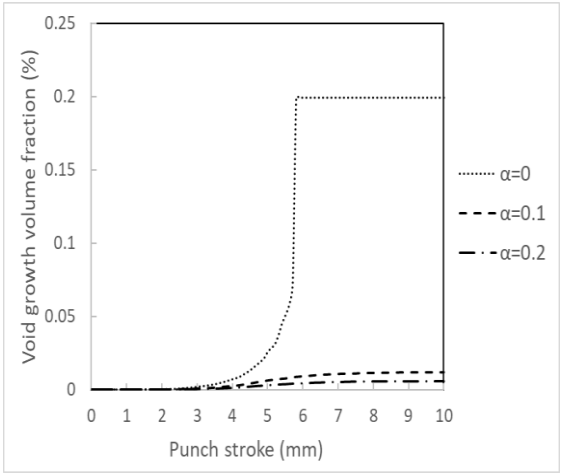

(b) Void growth volume fraction

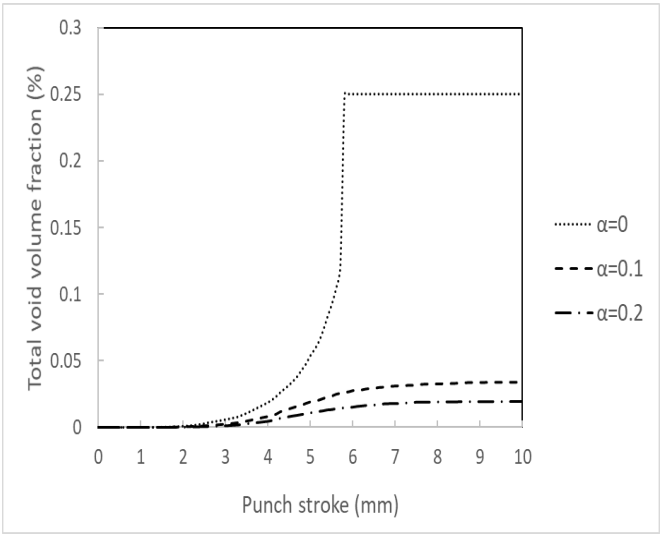

(c) Total void volume fraction

Figure 4. 14. Predicted (a) stress controlled void nucleation volume fraction, (b) void growth volume fraction and (c) total void volume fraction at point A for various values of α

4.4.4. GTN ductile fracture parametric study in bending test

As presented in Equation (3), normal distribution function is used in the GTN model to present the void nucleation growth and f_N, ε_N and S_N are void nucleation volume fraction, average void nucleating strain and standard deviation of void nucleating strain, respectively. Furthermore, coalescence happens following Equation (7) and there is a sharp increase when void volume fraction reaches critical void volume fraction (f_c) and failure happens when void volume fraction reaches f_f. Sensitivity of each ductile fracture parameters in the GTN model on force-displacement curve as well as bending fracture strain at room pressure and under superimposed pressure $p = -0.2\sigma_y$ is studied. The gain in ductility for two cases with various pressures are obtained and sensitivity of ε_N and f_c is discussed. Although not shown the effect of all parameters here, our numerical testing indicates that it is observed that ductility increases with increasing the ε_N, S_N and f_c and it decreases with increasing the f_N and it is unchanged with variation of f_f. Void volume fraction respect to punch stroke increases vertically beyond $f_c(= 0.15)$ and it can be understood that void volume fraction reaches f_f with a very low punch advancing beyond f_c. Thus, f_f does not have significant effect on ductility. Also, the ductility increases with increasing the σ_N when the stress-controlled GTN model is used. It is found that gain in ductility is higher at room pressure than under superimposed hydrostatic pressure for every ductile fracture parametric study. Ductility gain in this parametric study is the fracture strain change over the fracture strain of bending test with initial values of a parameters set. Superimposed hydrostatic pressure has insignificant effect on fracture strain change. On

the other hand, superimposed hydrostatic pressure increases the ductility (or fracture strain). Thus, this matter can be a justification as a decrease in ductility gain under superimposed hydrostatic pressure.

4.4.4.1. ε_N sensitivity

The sensitivity of ε_N under room pressure and superimposed pressure $p = -0.2\sigma_y$ is studied and force-displacement curves for each case are shown in Figures 4.15(a-b). As expected, ductility increases with increasing $\varepsilon_N$because void nucleation delays. Normal distribution function for various values of ε_N are shown in Figure 4.15(c) while other parameters are constant. It is seen clearly that void nucleation respect to effective plastic strain delays with increasing the ε_N. Furthermore, bending fracture strains are calculated and the gain in ductility for both cases are calculated and shown in Figure 4.15(d).

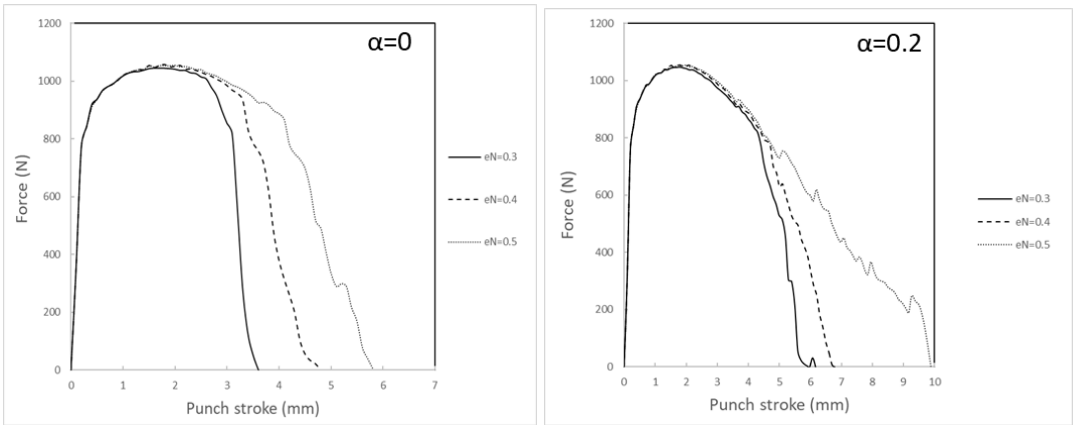

(a) Force-displacement curve ($\alpha = 0$) (b) Force-displacement curve ($\alpha = 0.2$)

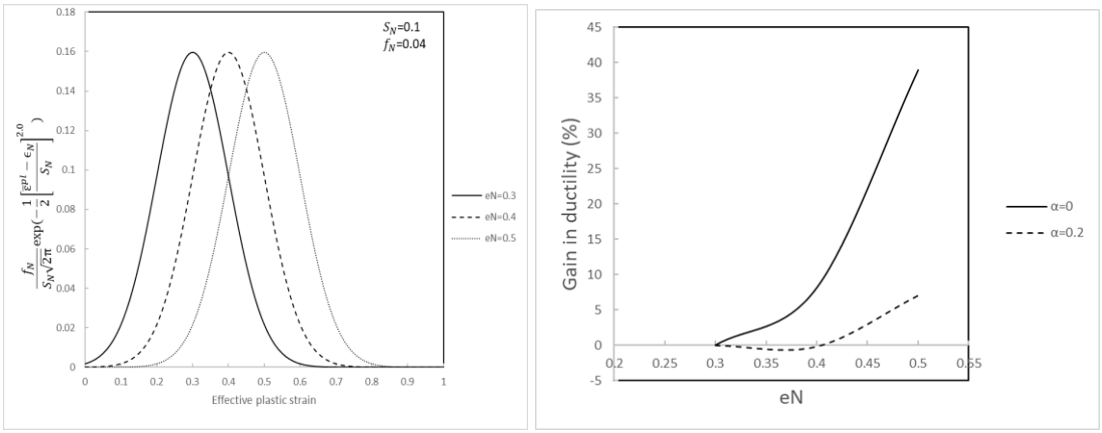

(c) Normal distribution function (d) Gain in ductility

Figure 4. 15. Effect of superimposed hydrostatic pressure on ε_N sensitivity

4.4.4.2. f_c sensitivity

The sensitivity of f_c under room pressure and superimposed pressure $p = -0.2\sigma_y$ is studied and force-displacement curves for each case are shown in Figures 4.16(a-b). As explained previously in Figure 4.4, there is a sharp knee on the load when void volume

fraction reaches f_c and then f varies linearly with the slope $\frac{f_u^* - f_c}{f_f - f_c}$ following Equation (7). As shown in Figure 4.16(c) ductility increases with increasing f_c as expected and the gain in ductility corresponding to room pressure is higher than that under superimposed hydrostatic pressure.

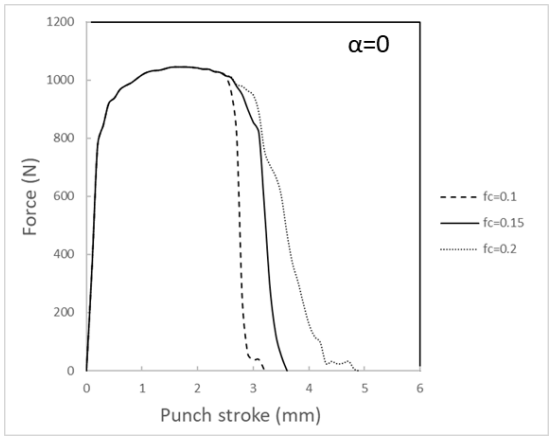

(a) Force-displacement curve ($\alpha = 0$)

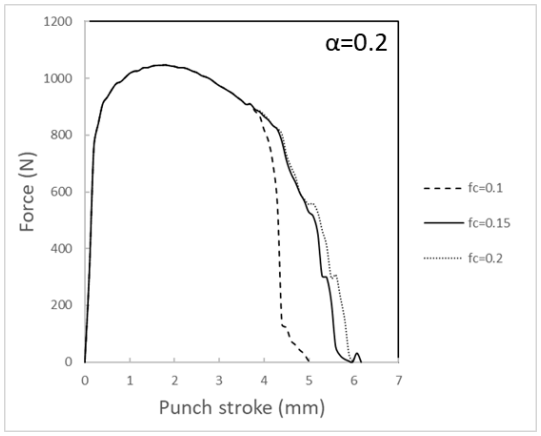

(b) Force-displacement curve ($\alpha = 0.2$)

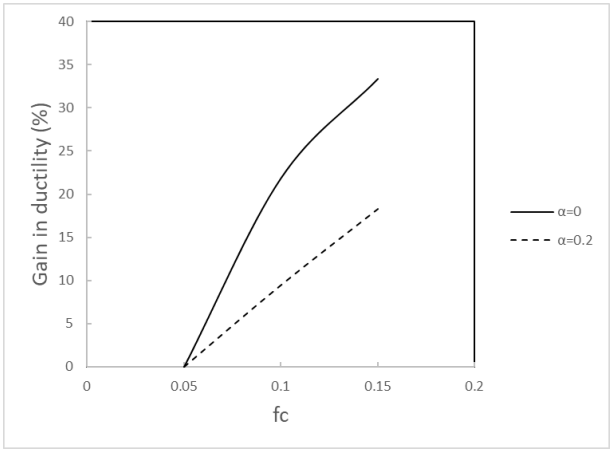

(c) Gain in ductility

Figure 4. 16. Effect of superimposed hydrostatic pressure on f_c sensitivity

4.5. Conclusion

In this study, a finite element analysis of plane strain three-point bending test for sheet metal under superimposed hydrostatic pressure is carried out. It is found that the superimposed hydrostatic pressure increases bendability significantly as hydrostatic pressure delays or completely eliminates void growth and coalescence of microvoids or microcracks. The fracture strains of bending tests are compared with those obtained in tensile tests under various superimposed hydrostatic pressures and it is demonstrated that the ductility in bending test is higher than those in tensile test. Lastly, ductile fracture parametric study in the GTN model is performed under various superimposed hydrostatic pressure and it is observed that ductility increases with increasing the ε_N, S_N and f_c and it decreases with increasing the f_N and it is unchanged with variation of f_f.

REFRENCES

1. D.J. Lloyd, M. Gallerneault, and R.B. Wagstaff, The deformation of clad aluminum sheet produced by direct chill casting. *Metallurgical and Materials Transactions A*, 2010. 41(8): p. 2093-2103.

2. Y. Shi, P.Z. Zhao, H. Jin, P.D. Wu, and D.J. Lloyd, Analysis of surface roughening in AA6111 automotive sheet under pure bending. Metallurgical and Materials Transactions A, 2016. 47(2): p. 949-960.

3. D. J. Lloyd, D. Evans, C. Pelow, P. Nolan and M. Jain, Bending in aluminium alloys AA 6111 and AA 5754 using the cantilever bend test. *Materials science technology*, 2002. 18(6): p. 621-628.

4. S.J. Sarkar, T.R.G. Kutty, K.T. Conlon, D.S. Wilkinson, J.D. Embury, D.J. Lloyd, Tensile and bending properties of AA5754 aluminum alloys. *Materials Science Engineering: A*, 2001. 316(1-2): p. 52-59.

5. S.J. Sarkar, T.R.G. Kutty, D.S. Wilkinson, J.D. Embury, D.J. Lloyd, Tensile properties and bendability of T4 treated AA6111 aluminum alloys. *Materials Science Engineering: A*, 2004. 369(1-2): p. 258-266.

6. P. Hou, H. Zhao, Z. Ma, S. Zhang, J. Li, X. Dong, Y. Sun and Z. Zhu, Influence of punch radius on elastic modulus of three-point bending tests. *Journal of Advances in Mechanical Engineering*, 2016. 8(5): p. 1-8.

7. J. Datsko, and C.T. Yang, Correlation of bendability of materials with their tensile properties. *Journal of Engineering for Industry*, 1960. 82(4): p. 309-313.

8. M.M. Shahzamanian, D.J. Lloyd and P.D. Wu, "Enhanced Bendability in Sheet Metals Produced by Cladding a Ductile Layer" *Materials Today Communications Journal*, 2020. 23: 100952.

9. M.F. Ashby, J.D. Embury, S.H. Cooksley and D. Teirlinck, Fracture maps with pressure as a variable. *Scripta metallurgica*, 1985. 19(4): p. 385-390.

10. A.S. Kao, H.A. Kuhn, O. Richmond and W.A. Spitzig, Tensile fracture and fractographic analysis of 1045 spheroidized steel under hydrostatic pressure. *Journal of Materials Research*, 1990. 5(1): p. 83-91.

11. A.S. Kao, H.A. Kuhn, W.A. Spitzig and O. Richmond, Influence of superimposed hydrostatic pressure on bending fracture and formability of a low carbon steel containing globular sulfides. *Journal of Engineering Materials and Technology*, 1990. 112(1): p. 26-30.

12. P. Weinrich and I. French, The influence of hydrostatic pressure on the fracture mechanisms of sheet tensile specimens of copper and brass. *Acta metallurgica*, 1976. 24(4): p. 317-322.

13. A.S. Kao, H.A. Kuhn, O. Richmond, and W.A. Spitzig, Workability of 1045 spheroidized steel under superimposed hydrostatic pressure. *Metallurgical Transactions A*, 1989. 20(9): p. 1735-1741.

14. M.F. Ashby, J.D. Embury, S.H. Cooksley and D. Teirlinck, Fracture maps with pressure as a variable. *Scripta metallurgica*, 1985. 19(4): p. 385-390.

15. I.E. French and P.F. Weinrich, The influence of hydrostatic pressure on the tensile deformation and fracture of copper. *Metallurgical Transactions A*, 1975. 6(4): p. 785.

16. I. French, P. Weinrich, and C. Weaver, Tensile fracture of free machining brass as a function of hydrostatic pressure. *Acta Metallurgica*, 1973. 21(8): p. 1045-1049.

17. A. Brownrigg, W. A. Spitzig, O. Richmond, D. Teirlinck and J.D. Embury, The influence of hydrostatic pressure on the flow stress and ductility of a spherodized 1045 steel. *Acta Metallurgica*, 1983. 31(8): p. 1141-1150.

18. A. Korbel, V. S. Raghunathant, D. Teirlinck, W. Spitzigs, O. Richminds and J. D. Embury, A structural study of the influence of pressure on shear band formation. *Acta Metallurgica*, 1984. 32(4): p. 511-519.

19. P.D. Wu, J.D. Embury, D.J. Lloyd, Y. Huang and K.W. Neale, Effects of superimposed hydrostatic pressure on sheet metal formability. *International Journal of Plasticity*, 2009. 25(9): p. 1711-1725.

20. J. Peng, P.D. Wu, Y. Huang, X.X. Chen, D.J. Lloyd, J.D. Embury and K.W. Neale, Effects of superimposed hydrostatic pressure on fracture in round bars under tension. *International Journal of Solids Structures*, 2009. 46(20): p. 3741-3749.

21. P.D. Wu, X.X. Chen, D.J. Lloyd, J.D. Embury, Effects of superimposed hydrostatic pressure on fracture in sheet metals under tension. *International Journal of Mechanical Sciences*, 2010. 52(2): p. 236-244.

22. Chen, X., P.D Wu, and D.J. Lloyd. Effect of Superimposed Hydrostatic Pressure on Bendability of Sheet Metals. *in AIP Conference Proceedings*. 2010. AIP.

23. ABAQUS Inc., A.M.V.-., 2014.

24. V. Tvergaard and A. Needleman, Analysis of the cup-cone fracture in a round tensile bar. *Acta metallu*rgica, 1984. 32(1): p. 157-169.

25. V. Tvergaard, Influence of voids on shear band instabilities under plane strain conditions. *International Journal of fracture*, 1981. 17(4): p. 389-407.

26. V. Tvergaard, On localization in ductile materials containing spherical voids. *International Journal of fracture*, 1982. 18(4): p. 237-252.

27. M.M. Shahzamanian, Anisotropic Gurson-Tvergaard-Needleman Plasticity and DamageModel for Finite Element Analysis of Elastic-Plastic Problems. *International Journal of Numerical Methods in Engineering*, 2018. 115(13), 1527-1551.

28. A.L. Gurson, Continuum theory of ductile rupture by void nucleation and growth: Part I—Yield criteria and flow rules for porous ductile media. *Journal of engineering materials technology*, 1977. 99(1): p. 2-15.

29. C. Chu and A. Needleman, Void nucleation effects in biaxially stretched sheets. *Journal of engineering materials technology*, 1980. 102(3): p. 249-256.

30. C. Butcher, Z. Chen, A. Bardelcik and M. Worswick, Damage-based finite-element modeling of tube hydroforming. *International Journal of Fracture*, 2009. 155: p. 55–65.

31. N. Benseddiq and A. Imad, A ductile fracture analysis using a local damage model. *International Journal of Pressure Vessels and Piping*, 2008. 85: p. 219–227.

32. A. Needleman, A continuum model for void nucleation by inclusion debonding. *Journal of Applied Mechanics*, 1987. 54: p. 525–531.

33. Y. Shi, H. Jin, P.D. Wu, and D.J. Lloyd, On the Study of the Sheet Bendability in AA5754-O Temper Alloy. *Metallurgical Materials Transactions A*, 2016. 47(10): p. 5203-5213.

34. J. Liu, Z. Wang, and Q. Meng, Numerical investigations on the influence of superimposed double-sided pressure on the formability of biaxially stretched AA6111-T4 sheet metal. *Journal of Materials Engineering Performance*, 2012. 21(4): p. 429-436.

35. R.G. Andersen, J.G. Londono, P.B. Woelke and K.L. Nielsen, Fundamental differences between plane strain bending and far-field plane strain tension in ductile plate failure. *Journal of the Mechanics and Physics of Solids*, 2020. 141. 103960

36. M. Costas, D. Morin , O. S. Hopperstad , T. Borvik and M. Langseth, A through-thickness damage regularisation scheme for shell elements subjected to severe bending and membrane deformations. *Journal of the Mechanics and Physics of Solids*, 2019. 123: p. 190–206.

37. A.R. Ragab and C.A. Saleh, Evaluation of bendability of sheet metals using void coalescence models. *Materials Science and Engineering: A*, 2005. 395(1-2): p. 102-109.

CHAPTER 5

Enhanced bendability in sheet metal produced by cladding a ductile layer

Complete citation:

M.M. Shahzamanian, D.J. Lloyd and P.D. Wu "Enhanced bendability in sheet metal produced by cladding a ductile layer" Journal of Materials Today Communications, 23 (2020) 100952

Copyrights:

Relative contributions:

M.M. Shahzamanian: Performed all the simulations, interpretation and analysis of the data, wrote the first draft of the manuscript including all figures and text and was responsible for the final draft submittal to the journal.

D.J. Lloyd: Revised and modified the journal paper draft

P.D. Wu: supervisor of M.M.Shahzamanian, revised and modified the journal paper draft.

ABSTRACT

The effect of cladding on the bendability of sheet metal is investigated numerically using the finite element method by employing the Gurson-Tvergaard-Needleman (GTN) model. The bendability and fracture strain increase significantly by cladding the sheet. In clad sheet metal, the development of the stress triaxiality in the region of the fracture slows down, thereby delaying the nucleation and growth of voids. In thin clad layers, the damage is initiated in the core but the crack is blunted at the clad core interface until the cladding thins and fails with increasing bending. Failure occurs in the cladding at sufficiently large cladding thickness. The effect of mandrel span length on bendability, which reflects the degree of bending in a three-point bend test, is also investigated to understand how failure transition from core fail to clad failure occurs. Finally, the effect of work hardening in the cladding material is examined, and bendability increases if the rate of hardening in the cladding material increases. Numerical results are found to be in good agreement with experimental observations.

Keywords: Laminated sheet; Bendability; Fracture; Finite element method (FEM).

5.1. Introduction

Monolithic materials may not provide the desired mechanical properties for various applications but utilizing laminated metal composites (LMCs) composed of alternating material layers may produce a more desirable combination of properties for an application [1]. As stated in [2], LMCs can improve many properties significantly, including fracture toughness [3], fatigue behavior [4], and impact behavior [5], or enhance formability and ductility [6–9]. Metal sheet strength and ductility can be provided simultaneously by cladding the sheet [10]. Conversely, the mechanical performance of materials can be studied through the three-point bending test [11–15]. However, to the best of our knowledge, the effect of cladding a sheet metal on bendability has not been considered numerically in detail elsewhere.

Cladding sheet metals has been performed through various methods such as cold roll bonding [16], hot-rolling [17], multilayer-friction stir brazing [18], Fusion Technology [7] and etc. Stainless steel (SS) has been clad with Niobium (Nb) in [19] via roll bonding and a micron-thick layer is generated at the interface during annealing. This layer leads to a brittle failure along with the interface between the SS core and Nb cladding. Hot-rolling can provide shear bond strength for low-carbon steel/austenitic stainless-steel clad composite as reported in [20]. However, roll bonding is costly and the “Fusion Technology” technique introduced by Novalis Inc. provides clad sheet metals with high strength and an oxide-free zone at the clad-core interface at a reduced cost [7]. To prove that high strength

at the clad-core interface is provided and bendability is improved, the tensile and bending tests of clad material consisting of an x609 core and softer AA3003 cladding materials were reported in [21]. Initial damage occurs away from the clad-core interface. This outcome demonstrated that the two materials were bonded with high interfacial strength and that interface delamination does not occur when the laminate is deformed. Final fracture under bending is initiated on the outer surface of the specimen, which is a free and unconstrained surface because of strain distribution in a bend test [21]. A superimposed hydrostatic pressure during bending delays void growth and the coalescence of micro-voids, thereby increasing bendability [22-24]. Nevertheless, bendability can also be improved by cladding the outer surface of the sheet with a more ductile layer [21]. Under these circumstances, failure initiates in a region close to the core-clad interface and then propagates toward the surface of the bent sample. The cladding thins locally and eventually fails with the crack propagating to the surface. Figure 5.1 shows the mechanism of fracture progression in a clad sheet metal under bending.

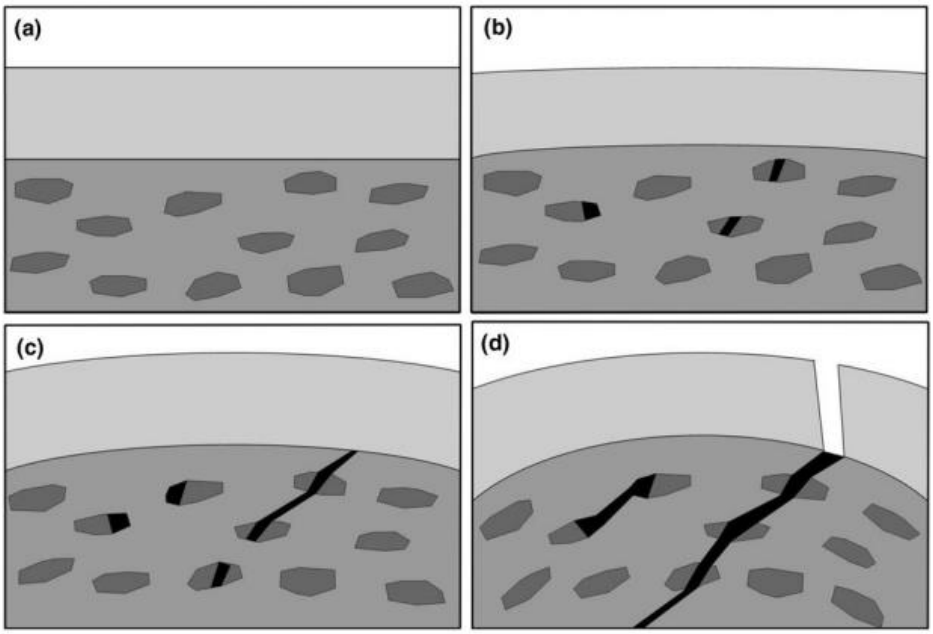

Figure 5. 1. The schematic of fracture path progression in a clad sheet under bending [21] through (a) to (d)

Chen et al. [25–26] investigated numerically the effect of cladding a ductile layer on a sheet sample and deforming under plane strain tension and assessed the effects of the clad layer on the necking and fracture strains using the finite element method. Cladding a ductile ring increases both the necking and fracture strains. Cladding enhances the hardening and the necking strain increases following the rule of mixture, which inhibits void nucleation and growth. Thus, ductility is significantly increased. Moreover, the topological arrangement of the cladding had a noticeable effect on the fracture strain while the necking strain remained unaffected. Furthermore, Hu et al. [27] studied the necking behavior of the clad sheet with a rate-sensitive cladding on rate-insensitive core materials.

The necking strain of the laminate increased with increasing strain-rate sensitivity of the clad layer and increased volume fraction of the cladding.

The aim of this study is to perform a numerical study of the effects of cladding on failure in sheet metal under three-point bending. All simulations are performed using ABAQUS/Explicit [28] according to the GTN model. The effect of cladding on the three-point bending test is explained in detail, and the effect of work hardening in clad materials on bendability is discussed.

5.2. Constitutive model

The Gurson-Tvergaard-Needleman (GTN) model [29-31] is used in this study which is based on damage growth in metals due to nucleation, void growth and coalescence. This model was originally developed by Gurson [32]. The void growth is a function of the plastic strain rate $\mathbf{D}^P$:

$$\left(\dot{f}\right)_{growth} = (1-f)\mathbf{I}\colon \mathbf{D}^P \tag{1}$$

and the void nucleation in ABAQUS is assumed to be strain controlled as following:

$$\dot{f} = \bar{A}\dot{\bar{\varepsilon}}^P \tag{2}$$

where $\dot{\bar{\varepsilon}}^P$ is the effective plastic strain rate, and the parameter $\bar{A}$ is chosen so that nucleation follows a normal distribution as suggested by Chu and Needleman [33]:

$$\bar{A} = \frac{f_N}{S_N\sqrt{2\pi}} exp\left[-\frac{1}{2}\left(\frac{\bar{\varepsilon}^p - \varepsilon_N}{S_N}\right)^2\right] \tag{3}$$

here, ε_N is the average void nucleating strain, f_N is the volume fraction of void nucleating particles and S_N is the standard deviation of void nucleating strain.

The growth of existing voids and the nucleation of new voids are considered in the evolution of void volume fraction as follows:

$$\dot{f} = \left(\dot{f}\right)_{growth} + \left(\dot{f}\right)_{nucleation} \tag{4}$$

and the function of void volume fraction $(f^*(f))$ is defined to consider coalescence as follows:

$$f^* = \begin{cases} f & for\ f \le f_c \\ f_c + \frac{f_u^* - f_c}{f_f - f_c}(f - f_c) & for\ f > f_c \end{cases} \tag{5}$$

where f_c is the critical void volume fraction when coalescence happens and f_f is the void volume fraction at failure. Lastly, the parameter $f_u^* = \frac{1}{q_1}$ is defined. It should be mentioned that void growth and nucleation does not happen when the stress state of an element is compressive in ABAQUS and void growth and nucleation only occurs in tension.

Finally, the approximate yield function to be used in which f^* is distributed randomly is as follows:

$$\Phi(\boldsymbol{\sigma}, \bar{\sigma}, f) = \frac{\sigma_e^2}{\bar{\sigma}^2} + 2f^* q_1 cosh\left(\frac{3q_2\sigma_H}{2\bar{\sigma}}\right) - [1.0 + (q_2 f^*)^2] = 0 \tag{6}$$

where, $\boldsymbol{\sigma}$ is the macroscopic Cauchy stress tensor and σ_e, σ_H and $\bar{\sigma}$ are equivalent stress, hydrostatic stress and matrix stress, respectively. Also, q_1 and q_2 are the calibrated

parameters. The uniaxial elastic-plastic undamaged stress-strain curve for the matrix material is provided by the following power-law form:

$$\bar{\sigma} = \begin{cases} E\bar{\varepsilon}, & for\ \bar{\sigma} \le \sigma_y \\ K\bar{\varepsilon}^n, & for\ \bar{\sigma} > \sigma_y \end{cases} \tag{7}$$

5.3. Problem formulation and method of solution

The schematic presentation of a clad metal sheet with a length L_o and thickness t_o is considered (Figure 5.2). Due to the symmetry, only half of the sheet is investigated. The sheet is assumed to be wide enough with no deformation in the width direction to consider the plane strain state. The sheet is presumed to consist of a soft cladding layer with a thickness $\bar{t}_o$ and a core with thickness of $t_o - \bar{t}_o$. Thus, the cladding ratio is defined as $\Gamma = \frac{\bar{t}_o}{t_o}$. In [7], the cladding layer and core are assumed to be bonded perfectly. Rigid bodies are considered for both punch and mandrel with radii R_p and R_m, respectively. The Mandrel is stationary with a span length L_m when the punch applies force in the middle section of the sheet.

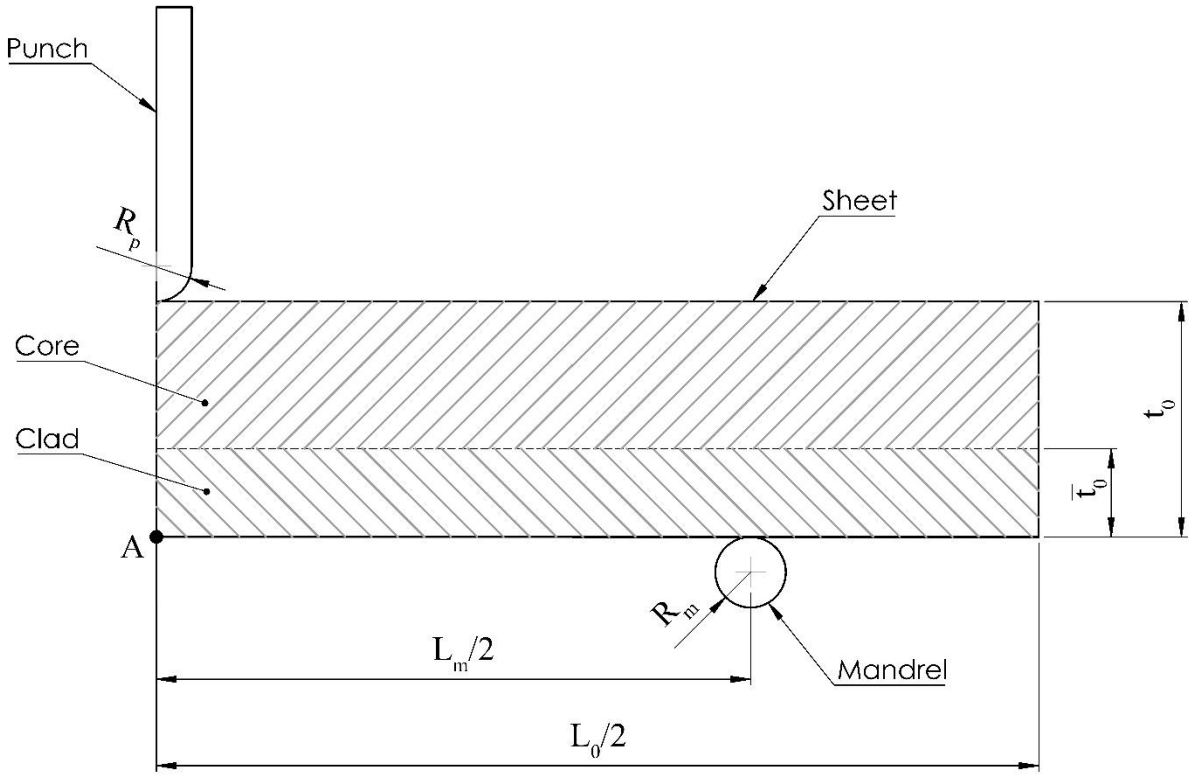

Figure 5. 2. Schematic of three-point bending test for a clad sheet metal 5.4. Results

5.4. Results

The elastic-plastic properties of the matrix and cladding materials are specified as presented in Table 5.1. The values of the mechanical properties regarding the GTN model for the matrix material are taken from Tvergaard and Needleman [34].

Table 5. 1. Matrix and cladding material constants

	$E\ (GPa)$	ν	$\sigma_y\ (MPa)$	K	n	q_1	q_2	f_N	ε_N	S_N	f_c	f_f
Matrix material	71	0.3	234.3	414.9	0.1	1.5	1.0	0.04	0.3	0.1	0.15	0.25
Cladding material	71	0.3	142	492.1	0.2	1.5	1.0	0.03	0.5	0.1	0.25	0.35

The purpose of cladding in this study is to enhance formability and ductility, the clad material is assumed to have higher work hardening and greater ductility than the core material. In other words, compared with the core material, the clad material has relatively lower yielding stress but higher hardening and higher resistance to void nucleation [25]. Therefore, the values of the material parameters for the cladding material are supposed to be similar to those for the core except for E, σ_y , K, n, f_N, ε_N, f_c, and f_f. Figure 5.3 shows the true stress and true strain curves of the core and cladding materials under homogeneous uniaxial tension. It should be emphasized that the main purpose of the present research is to assess the effect of cladding on the bendability of sheet metals and that the overall results and conclusions are not particularly dependent on the above values of the material parameters.

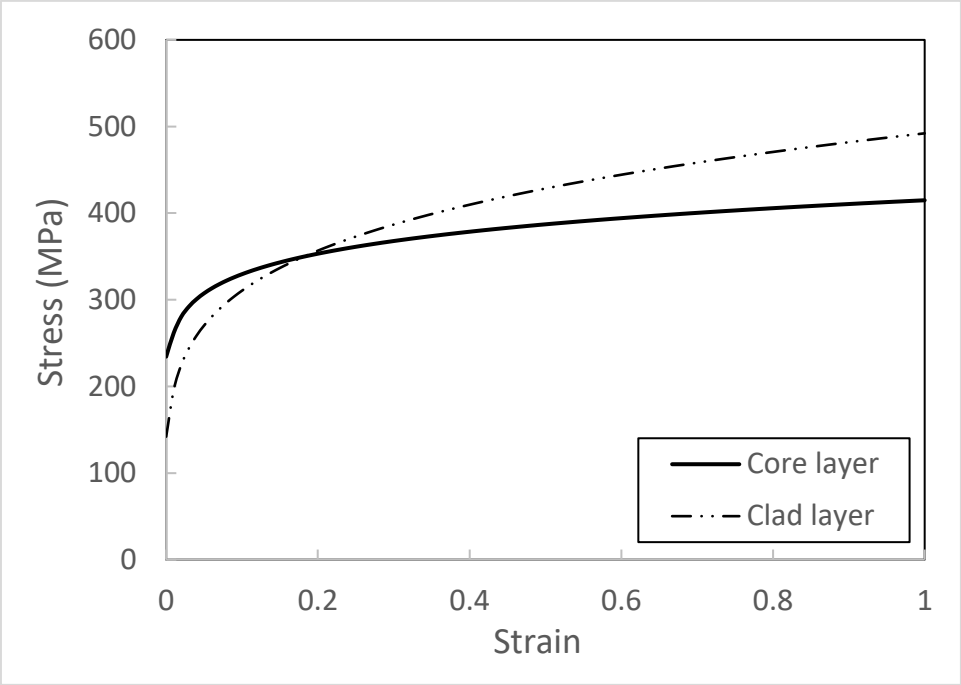

Figure 5. 3. Uniaxial tension stress and strain curves of the core and cladding materials

The penalty contact method is considered for the contact interaction between the sheet and mandrels and the punch. Contact pair interactions are defined by specifying each of the individual surface pairs that can interact with each other and which searches for node-into-face and edge-into-edge penetrations in the current configuration. The plane strain is considered for the sheet metal in the three-point bending test. Thus, the plane strain quadrilateral element CPE4R in ABAQUS/Explicit is used for the sheet. The rigid body element R2D2 is also utilized for the punch and mandrels. The length of the sheet (L_o), thickness (t_o), and plane strain thicknesses are 20, 2.5, and 10 mm, respectively. Moreover, R_m and R_p are 0.25 and 0.2 mm, respectively.

ABAQUS/Explicit is used in this analysis because ABAQUS/Standard does not provide failure in the GTN model. To minimize the dynamic effect of the sample, the mass scaling method with enough low target time increment is applied. The ABAQUS/Explicit results and those obtained with ABAQUS/Standard before initiation of failure showed satisfactory agreement.

Mesh sensitivity is inevitable in finite element simulations, especially those involving localized deformation and fracture. Thus, different meshes are considered in this simulation. Figure 5.4 shows the finite element (FE) configuration of a three-point bending test for a monolithic specimen ($\Gamma = 0$) with a typical mesh consisting of 30 × 500 plane strain quadrilateral elements (CPE4R) distributed uniformly. The effect of mesh sensitivity on bending fracture strain will be discussed later in this section. Due to the symmetry, only half of the sheet is considered, and symmetric boundary conditions are applied in the middle section of the specimen.

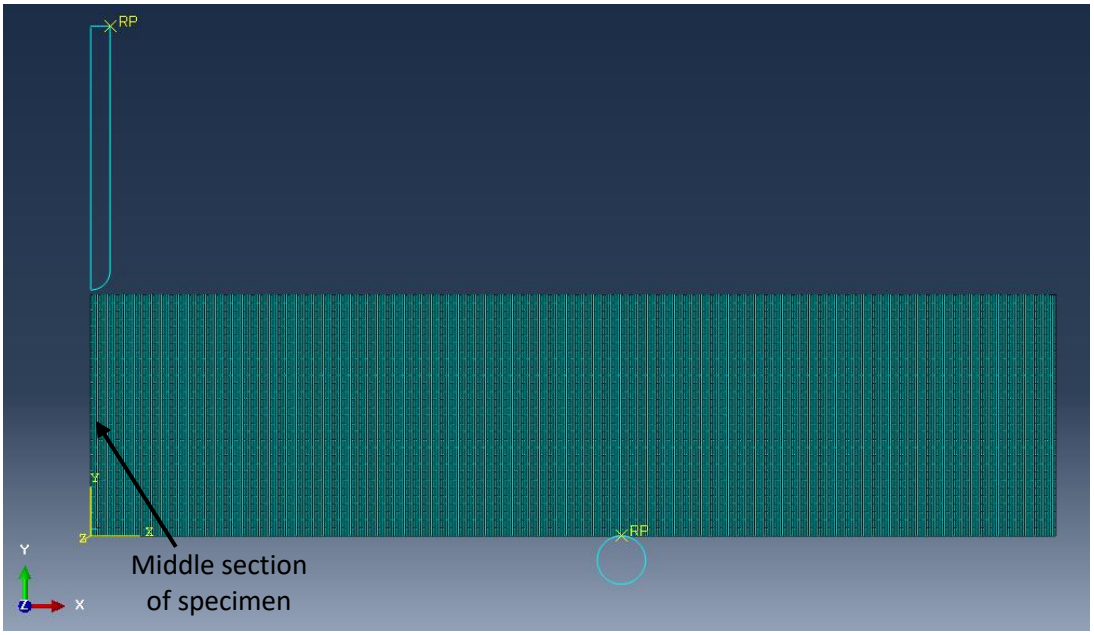

Figure 5. 4. FE configuration of the three-point bending test: a typical mesh for a metal sheet with 30 × 500 quadrilateral elements (CPE4R in ABAQUS/Explicit)

Figure 5.5 shows the punch force F as a function of punch stroke d for the core material $(\Gamma = 0)$. The effect of mesh sensitivity on the force–displacement curve is also shown in this figure. First, the load increases linearly with a very small amount of punch stroke in which the sheet is in the elastic state. Then, the force increases gradually and reaches its maximum followed by a gradual decrease with further a punch stroke. The additional punch stroke leads to a sharp "knee" on the force. At this stage, the void volume fraction (f) at the outer surface in the middle of the specimen section, which is under tension, reaches the critical void volume fraction (f_c). Immediately after the sharp knee, a burst of void growth and nucleation results in a rapid drop in the punch force, thereby implying a rapid loss of load carrying capacity for the sheet metal specimen. Two different meshes of 30 × 500 elements (30 elements in the Y direction and 500 elements in the X direction)

and 45 × 750 elements (45 elements in Y direction and 750 elements in X direction) are examined and the effect of mesh sensitivity on the force–displacement curves are presented in Figure 5.5. These two meshes are very carefully designed to have an aspect ratio close to 1.0 in the middle section of the specimen where the fracture occurs. The size of the elements has an insignificant effect on fracture initiation.

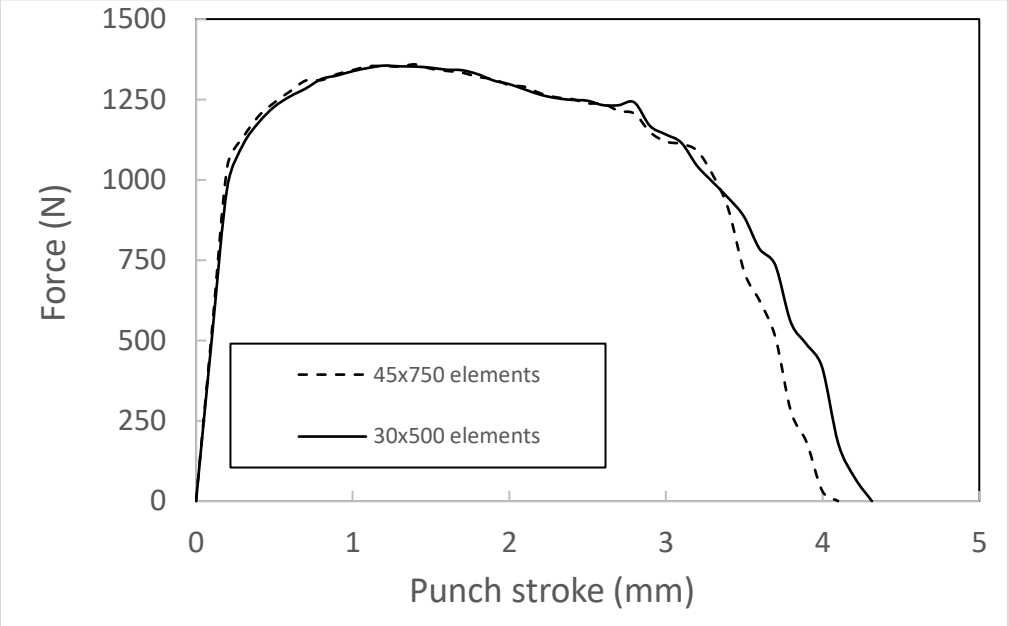

Figure 5. 5. Effect of mesh sensitivity on the force–displacement curve ($\Gamma = 0$)

5.4.1. Effect of span length of mandrel

The bending moment increases with the decreasing mandrel span length as stated in [35]. Moreover, the three-point bending test requires more load to deform the sheet metal than the test with a longer span. Figure 5.6(a) shows the force–displacement curves of

monolithic sheets ($\Gamma = 0$) with various spans while the thickness is kept constant. The maximum value of the force increases with decreasing span length. Furthermore, decreasing the span causes less deflection and prompts the material to fail earlier as the concentrated load in the middle section of the sheet specimen increases. Figure 5.6(b) shows that the fracture strain decreases with an increasing span length.

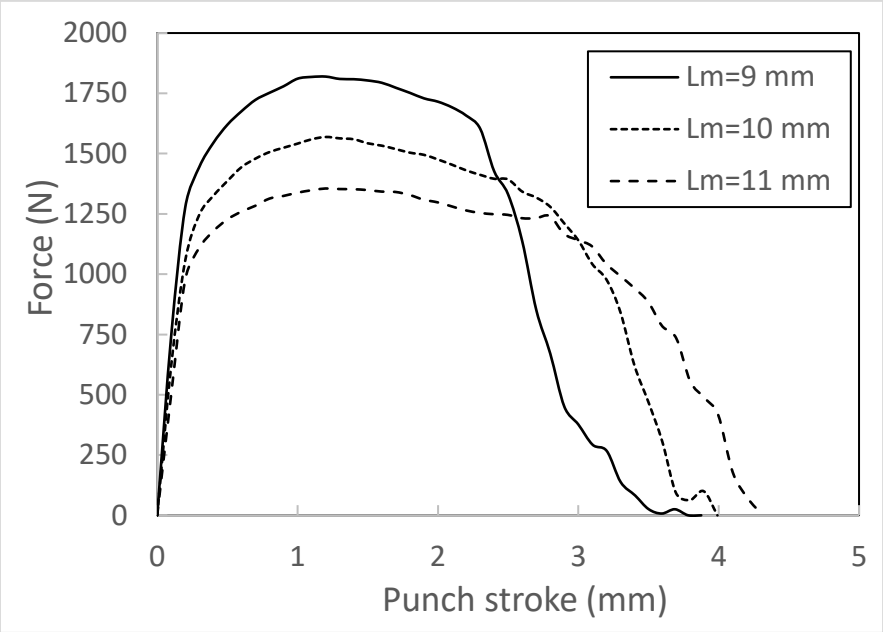

(a) Force-displacement curves

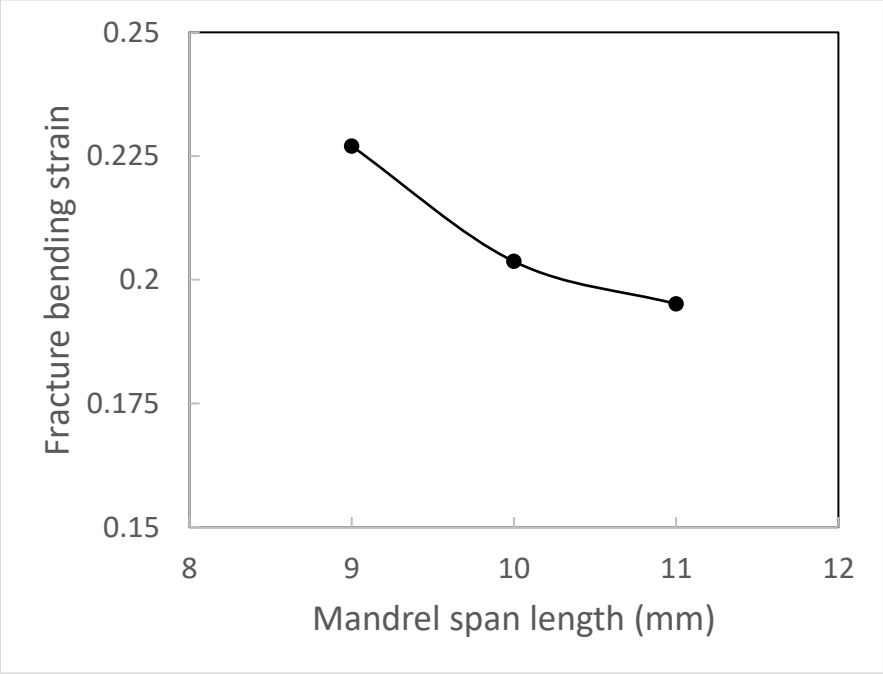

(b) Fracture bending strains

Figure 5. 6. Effect of the mandrel span length on the bendability of sheet metals: (a) force–displacement curves and (b) bending fracture strains

5.4.2. Effect of cladding thickness ratio (Γ)

The effect of the cladding ratio, Γ on fracture under plane strain three-point bending test was studied. Figure 5.7 shows the effect of Γ on the force–displacement curve. The force in the clad sheet first decreases and then increases with punch advancement compared to the force in the monolithic sheet. This phenomenon is consistent with the stress-strain behavior of the core and clad materials shown in Figure 5.3. The sharp knee on the force–displacement curve is delayed with an increase in Γ. The effect of Γ was investigated for three different cases of $\frac{L_m}{2} = 4.5, 5.0, \text{and } 5.5\ mm$. Fracture did not occur for cladding ratios higher than $\Gamma = 0.3$ and $\Gamma = 0.2$ for cases with $\frac{L_m}{2} = 5.0$ mm and $\frac{L_m}{2} = 5.5\ mm$, respectively.

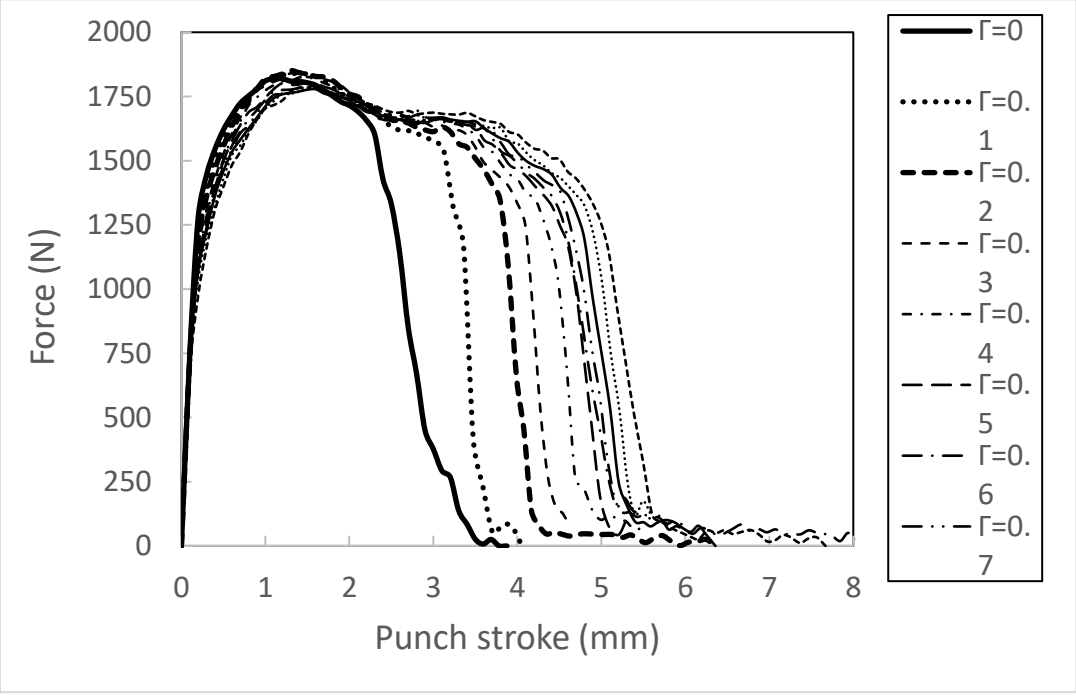

(a) $\frac{L_m}{2} = 4.5\ mm$

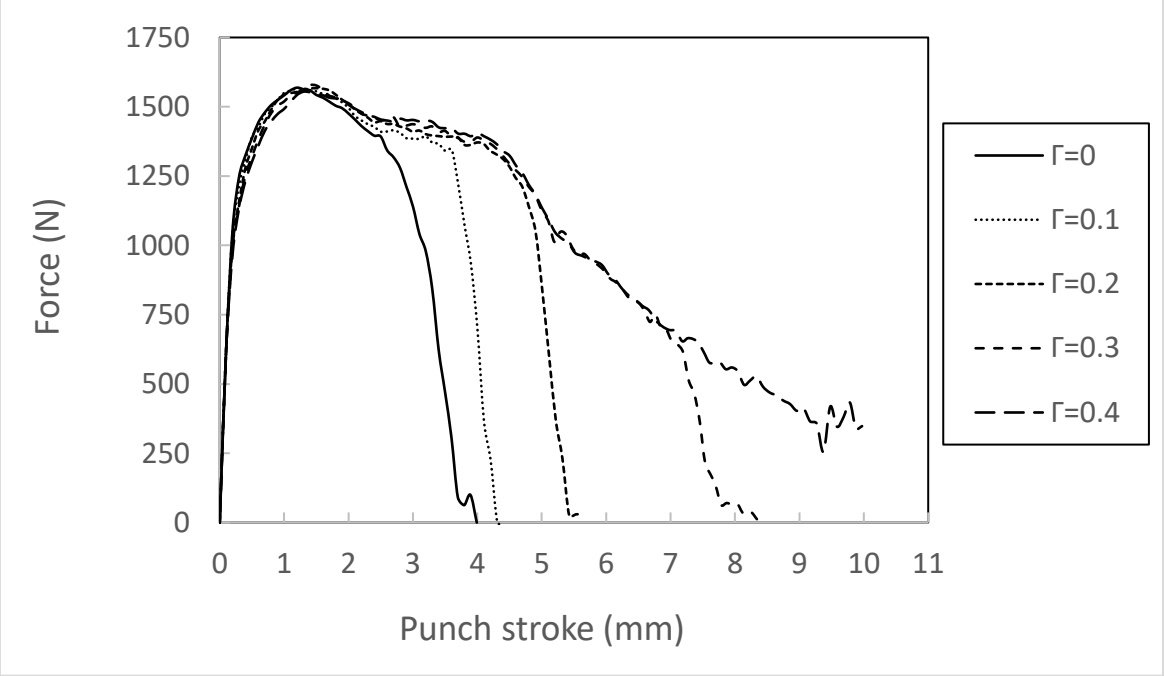

(b) $\frac{L_m}{2} = 5.0\ mm$

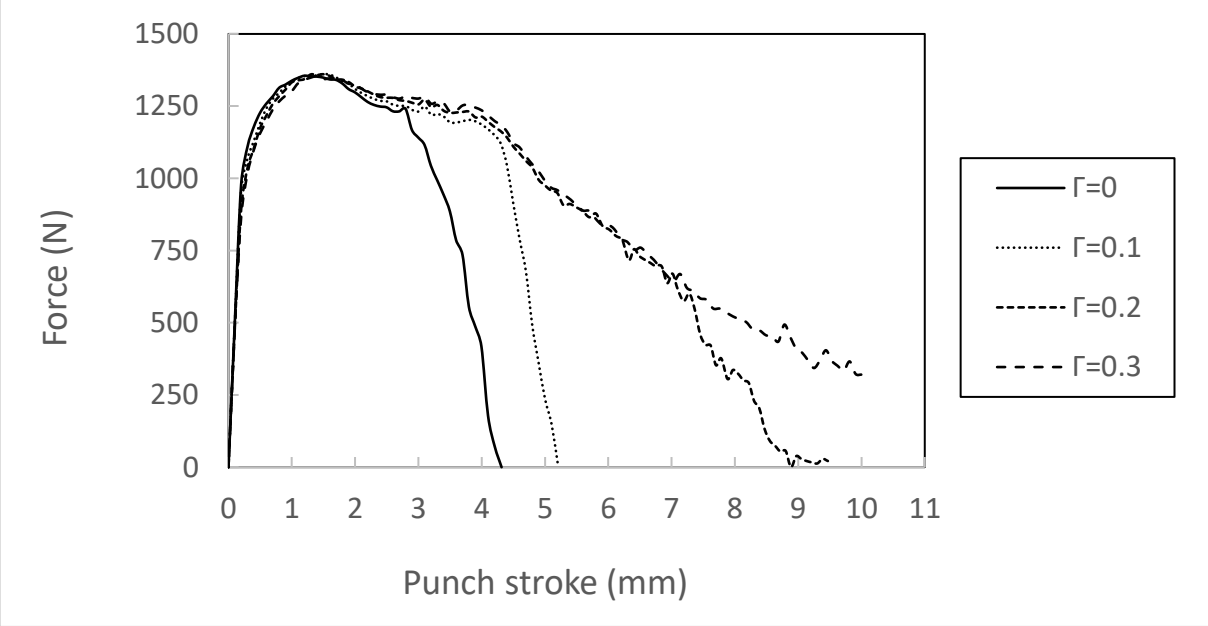

(c) $\frac{L_m}{2} = 5.5\ mm$

Figure 5. 7. Effect of Γ on the force–displacement curves for three different L_m values: (a) $\frac{L_m}{2} = 4.5\ mm$ (b) $\frac{L_m}{2} = 5.0\ mm$, and (c) $\frac{L_m}{2} = 5.5\ mm$

Figure 5.8 presents the crack patterns in the clad sheet metals for various Γ with three different values of $\frac{L_m}{2} = 4.5, 5.0, \text{and } 5.5\ mm$. The location of failure initiation changes with an increase of Γ and a variation in the span length. In Figure 5.8, the core clad interface is indicated with arrows. Decreasing the span length increases the bending strain for any punch displacement. For the highest bending strain $\frac{L_m}{2} = 4.5$, failure initiation is dominated by failure in the core for cladding ratios below 0.3; conversely, failure initiation occurs in the core and cladding above this level until failure of the cladding predominates at a cladding ratio above 0.4. This progression of failure in the core to that in the cladding is also observed at the other span lengths but the cladding ratio at which they occur changes and in some cases no bend failure occurs for high cladding ratios. These trends are consistent with the force displacement plots shown in Fig. 7.

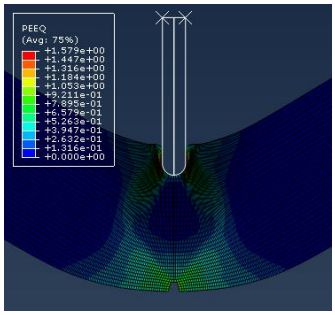

$\Gamma = 0$
(crack in core)

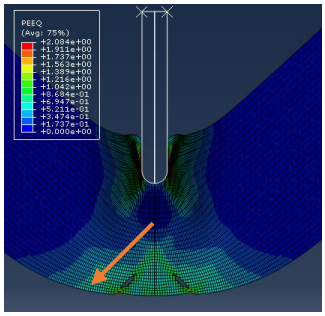

$\Gamma = 0.1$
(crack in core)

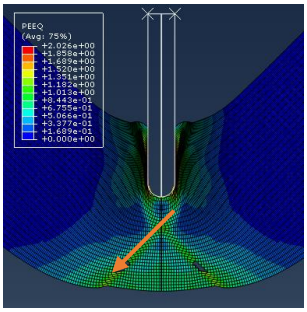

$\Gamma = 0.2$
(crack in core)

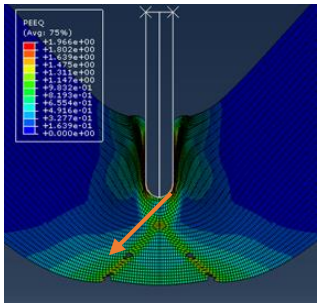

$\Gamma = 0.3$
(crack in core and clad)

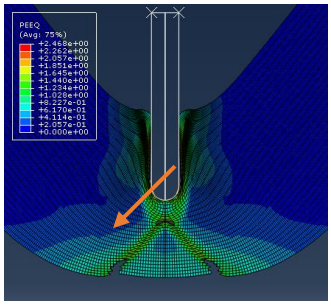

$\Gamma = 0.4$
(crack in clad)

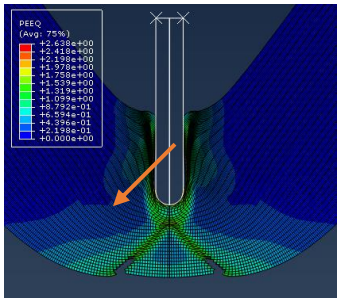

$\Gamma = 0.5$
(crack in clad)

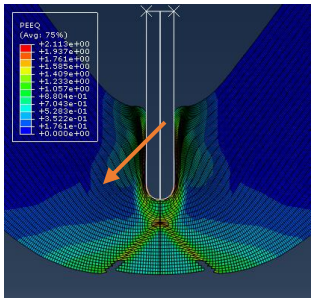

$\Gamma = 0.6$
(crack in clad)

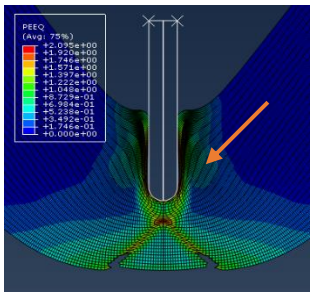

$\Gamma = 0.7$
(crack in clad)

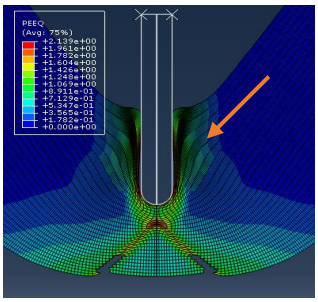

$\Gamma = 0.8$
(crack in clad)

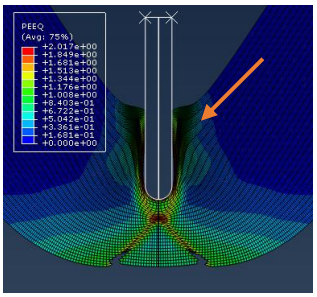

$\Gamma = 0.9$
(crack in clad)

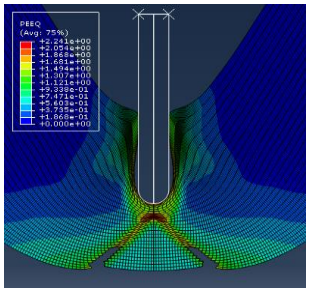

$\Gamma = 1.0$
(crack in clad)

(a) $\frac{L_m}{2} = 4.5$

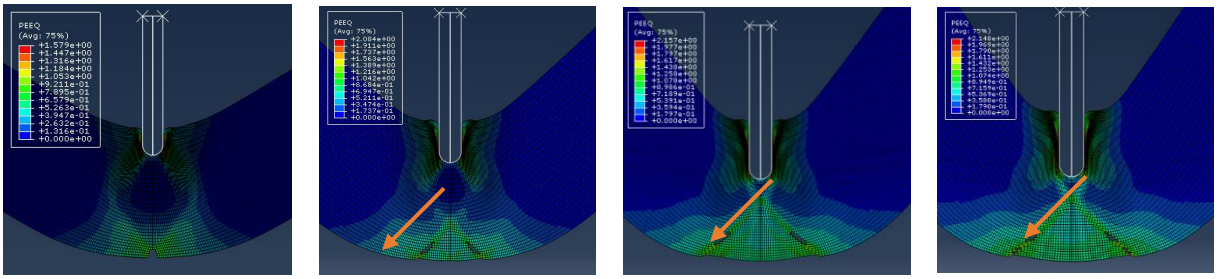

$\Gamma = 0$ $(crack\ core)$ $\Gamma = 0.1$ $(crack\ in\ clad)$ $\Gamma = 0.2$ *(crack in clad)* $\Gamma = 0.25$ *(core and clad)* *crack in core is dominant*

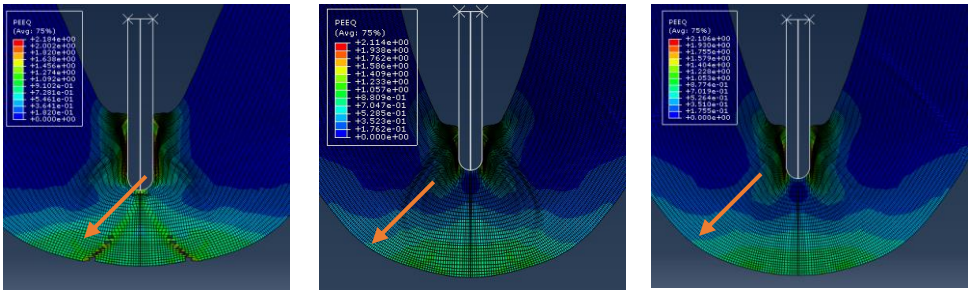

$\Gamma = 0.3$ *(core and clad)* *crack in clad is dominant* $\Gamma = 0.35$ *(No fracture)* $\Gamma = 0.4$ *(No fracture)*

(b) $\frac{L_m}{2} = 5.0\ mm$

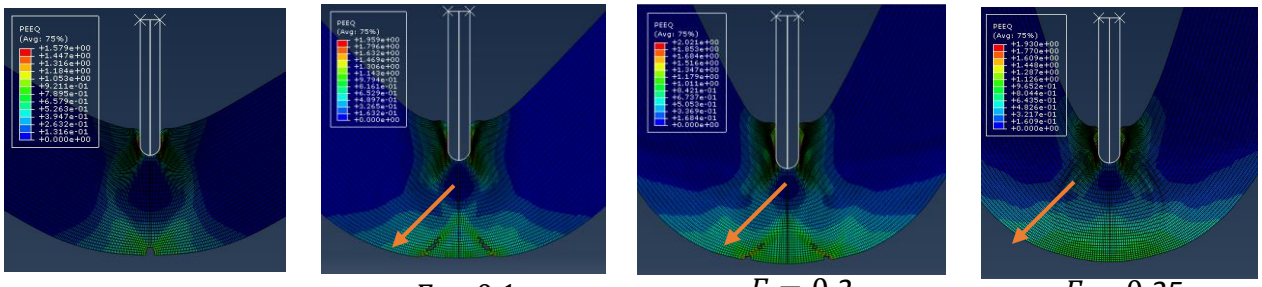

$\Gamma = 0$ $(crack\ in\ core)$ $\Gamma = 0.1$ $(crack\ in\ core)$ $\Gamma = 0.2$ $(crack\ in\ both\ core\ and\ clad)$ $\Gamma = 0.25$ *(No fracture)*

(c) $\frac{L_m}{2} = 5.5\ mm$

Figure 5. 8. Crack shapes of sheet metals for various Γ with three different cases: (a) $\frac{L_m}{2} = 4.5\ mm$, (b) $\frac{L_m}{2} = 5.0\ mm$, and (c) $\frac{L_m}{2} = 5.5\ mm$

The effect of Γ on the normalized minimum cross-sectional area $\left(\frac{A_{min}}{A_o}\right)$ and bending fracture strain $\varepsilon_f^c = \ln \frac{A_o}{A_{min}}$ in the middle section of the specimen are shown in Figures 5.9 and 10. A_{min} is the minimum cross-sectional area of the sheet which is calculated one step right before fracture initiation in ABAQUS. Note that the cross-sectional area in the tensile test decreases because of neck development, but macroscopic necking does not occur in a bend test. The cross-sectional area of a specimen decreases because of the general thinning of the bending sample in response to the punch stroke. A bigger ε_f^c means more ductility because the punch advances more without fracture initiation in the specimen. The minimum cross-sectional area decreases with increasing Γ and allows the specimen to deform more, thereby increasing the ductility and bending fracture strain.

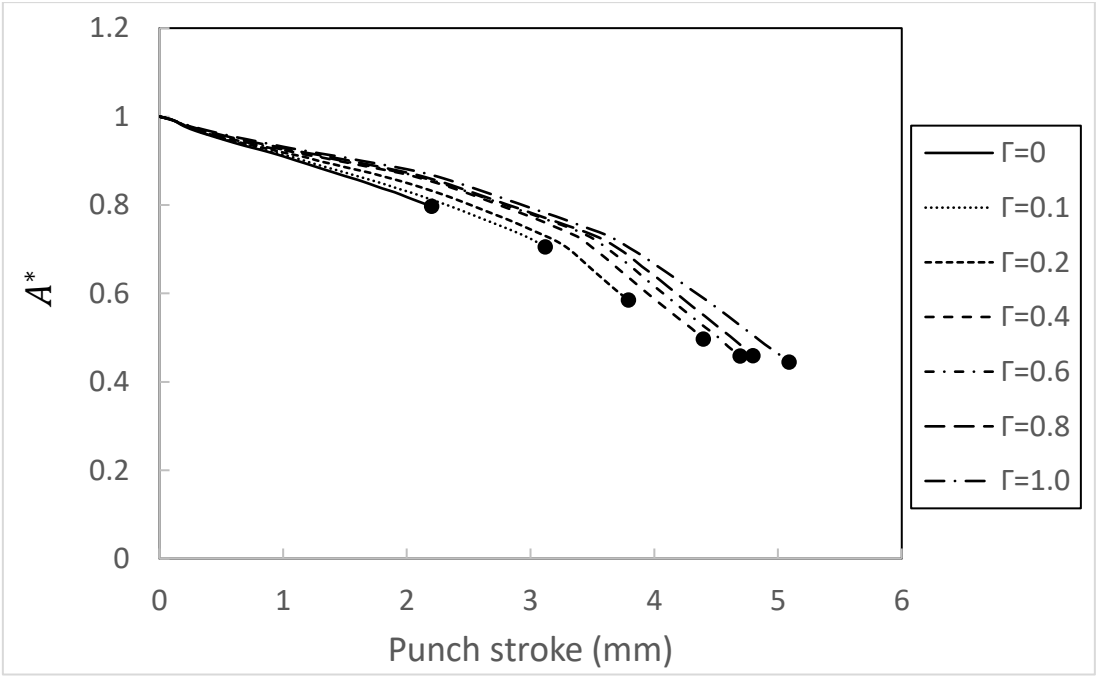

Figure 5. 9. Normalized minimum cross-sectional area ($\frac{L_m}{2} = 4.5\ mm$)

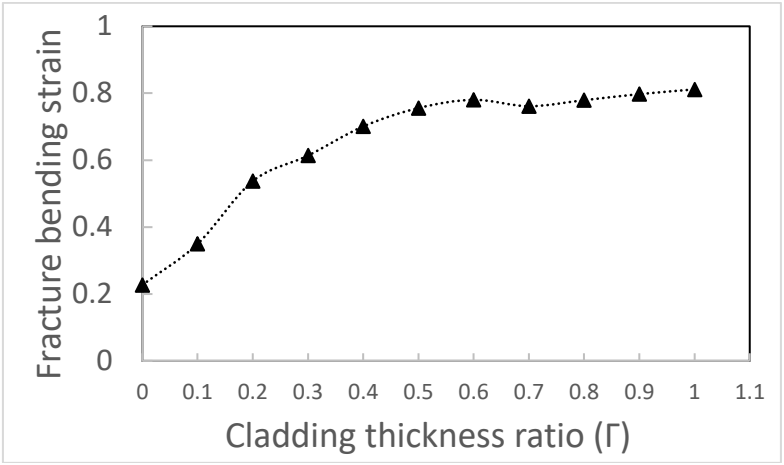

(a) $\frac{L_m}{2} = 4.5\ mm$

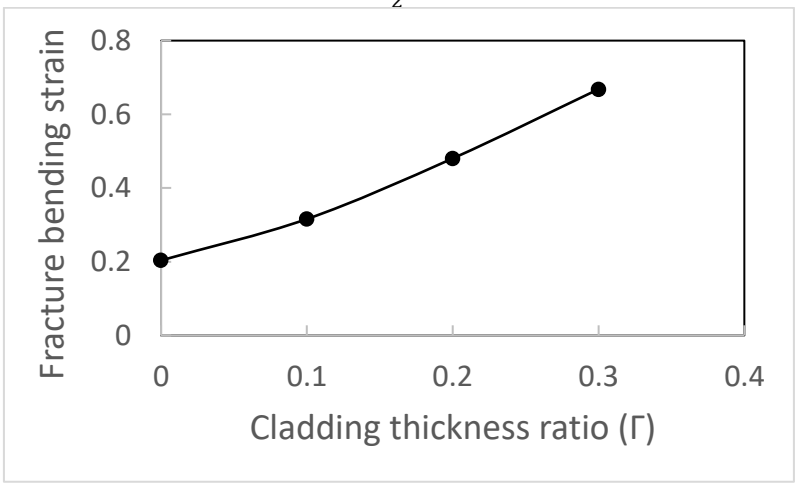

(b) $\frac{L_m}{2} = 5.0\ mm$

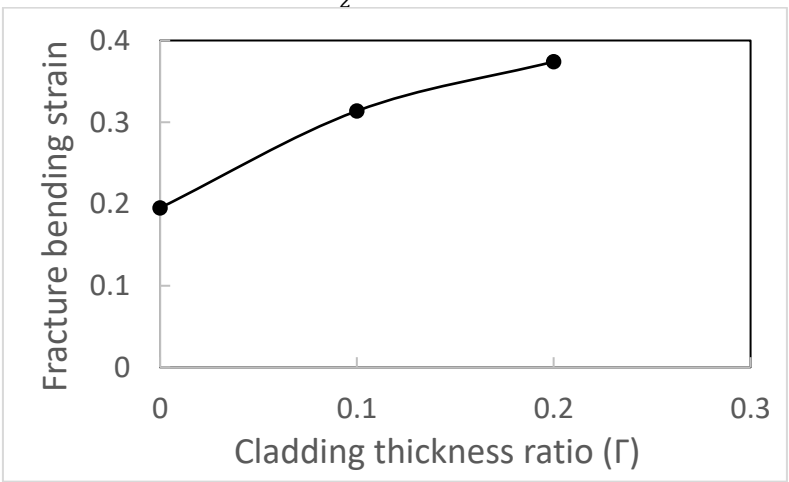

(b) $\frac{L_m}{2} = 5.5\ mm$

Figure 5. 10. Fracture bending strain; (a) $\frac{L_m}{2} = 4.5$, $(b)\ \frac{L_m}{2} = 5.0$ and $\frac{L_m}{2} = 5.5$

Cladding also affects the development of hydrostatic pressure $\sigma_H = (1/3)(\sigma_{xx} + \sigma_{yy} + \sigma_{zz})$ and stress triaxiality $\frac{\sigma_H}{\bar{\sigma}}$ at the fracture initiation site. Figure 5.11 presents the hydrostatic pressure and stress triaxiality at the fracture site when $\frac{L_m}{2} = 4.5\ mm$ for various values of Γ. Hydrostatic pressure and stress triaxiality change at different locations in a bent specimen due to the generated strain gradient and fracture initiates at different locations with various values of Γ. Fracture occurs at the outer surface in the middle section of the specimen for case $\Gamma = 0$. For cases $\Gamma = 0.1$ and $\Gamma = 0.2$, fracture appears in the core close to the clad-core interface of cladding material. For cases with $\Gamma > 0.2$, fracture transpires at the outer surface of the specimen where the material is clad. In general, the hydrostatic stress increases with increasing cladding ratio, as does the stress triaxiality. Both effects are pronounced particularly at large bending strains. Figure 5.12 presents the void volume fraction growth at fracture sites with various values of Γ when $\frac{L_m}{2} = 4.5\ mm$. Clearly, the void volume fraction slows down with the increase of Γ. For cases $\Gamma \leq 0.2$, fracture initiates in the core material when the $f_f = 0.25$ and for cases $\Gamma > 0.2$ fracture initiates in the cladding material when $f_f = 0.35$.

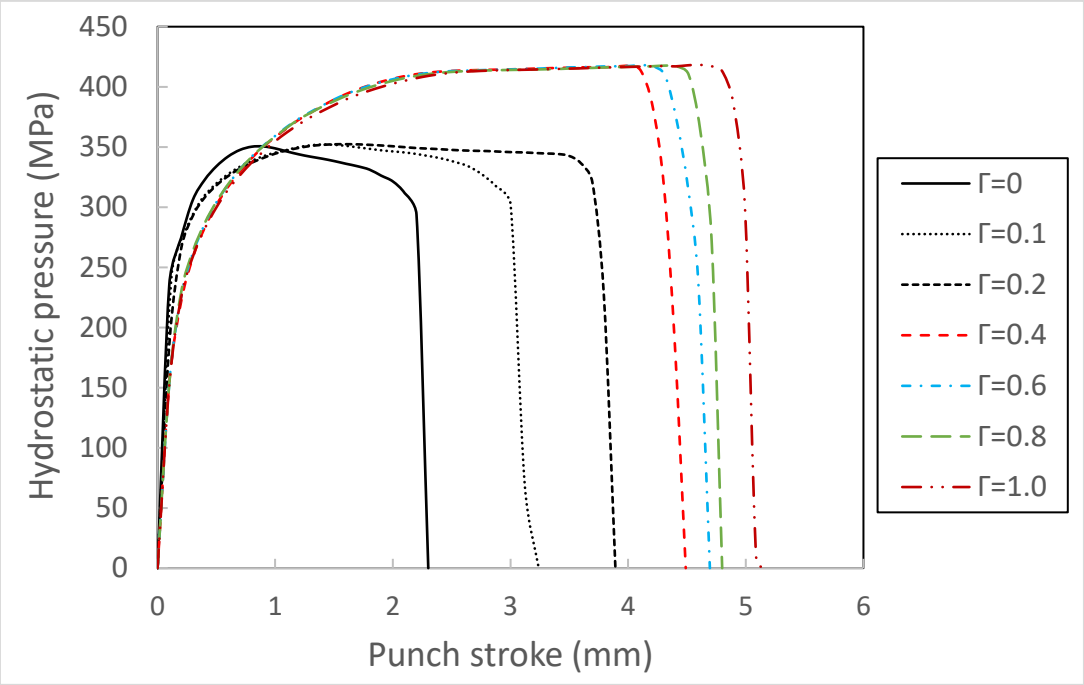

(a) Hydrostatic pressure

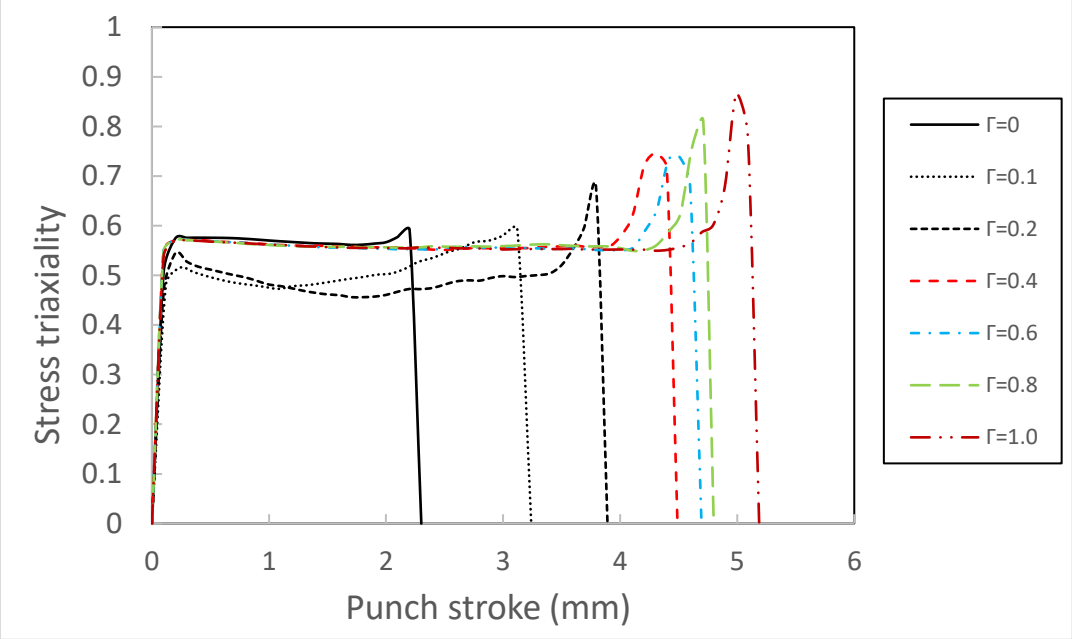

(b) Stress triaxiality

Figure 5. 11. Effect of cladding on (a) hydrostatic pressure and (b) stress triaxiality at fracture sites ($\frac{L_m}{2} = 4.5\ mm$)

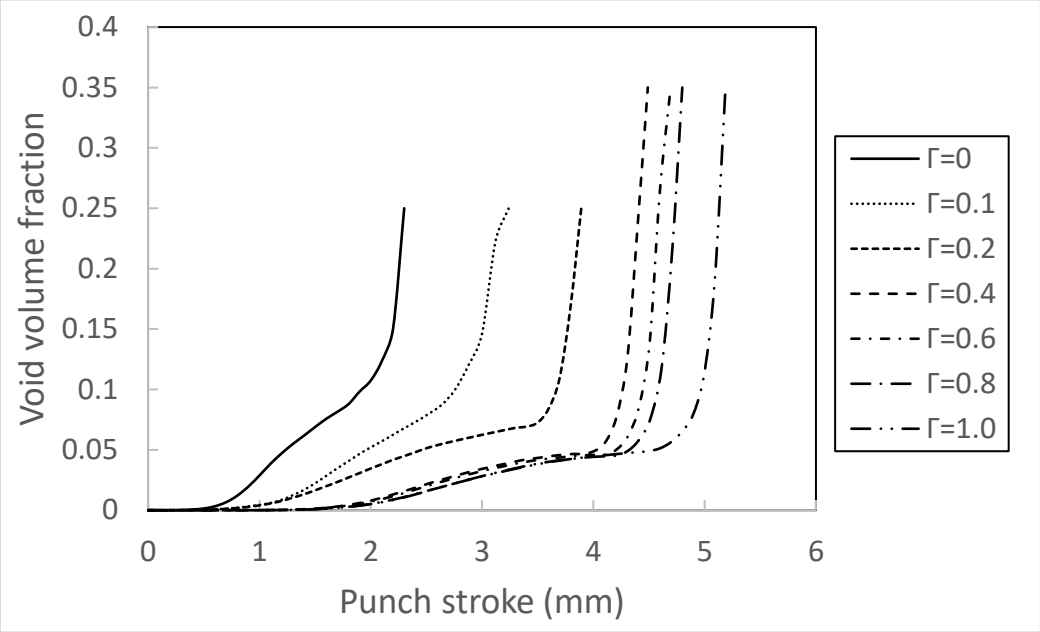

Figure 5. 12. Effect of Γ on void volume fraction ($\frac{L_m}{2} = 4.5\ mm$)

5.4.3. Effect of work hardening in clad material

The main mechanical properties of the laminate are provided by the core properties, but these can be modified by the choice and behavior of the cladding alloy. The effect of cladding material work hardening on bendability is investigated in this section when $\frac{L_m}{2} = 5.5\ mm$. The effect of parameters "*K*" and "*n*" in the cladding following the power law equation $\bar{\sigma} = K\bar{\varepsilon}^n$ is considered. Different stress-strain curves with various values of "*K*" and "*n*" are shown in Figure 5.13. The rate of hardening remains constant with varying "*K*" but changes with various values of "*n*". In Figure 5.14, the force–displacement curves of the clad sheet with $\Gamma = 0.1$ and $\Gamma = 0.2$ are presented. As expected, the magnitude of the

bending force increases with higher values of stress in the cladding material. These figures indicate that "*K*" has an insignificant effect on bendability, but "*n*" has a significant effect.

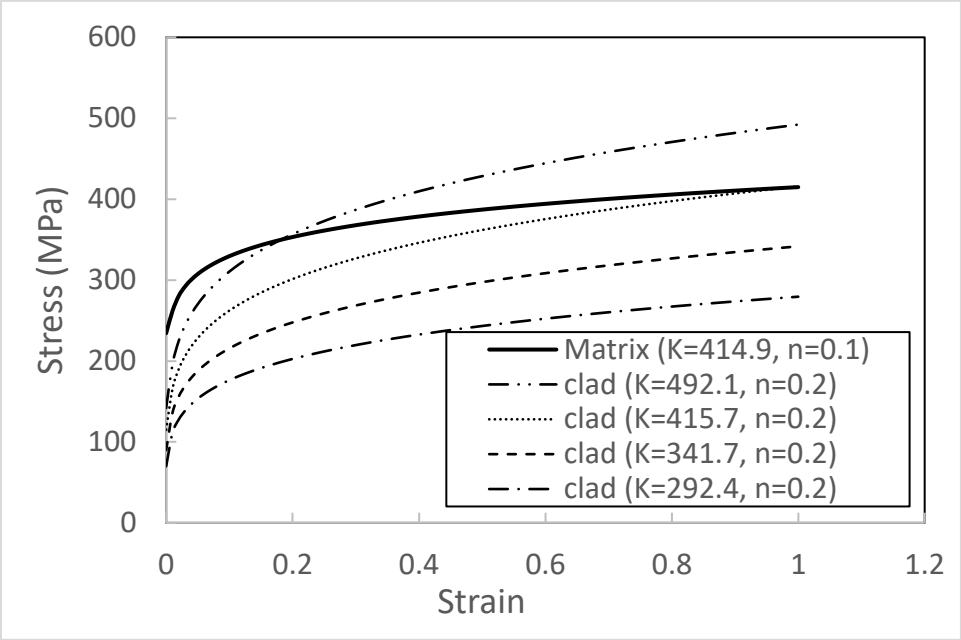

(a) "*K*" sensitivity

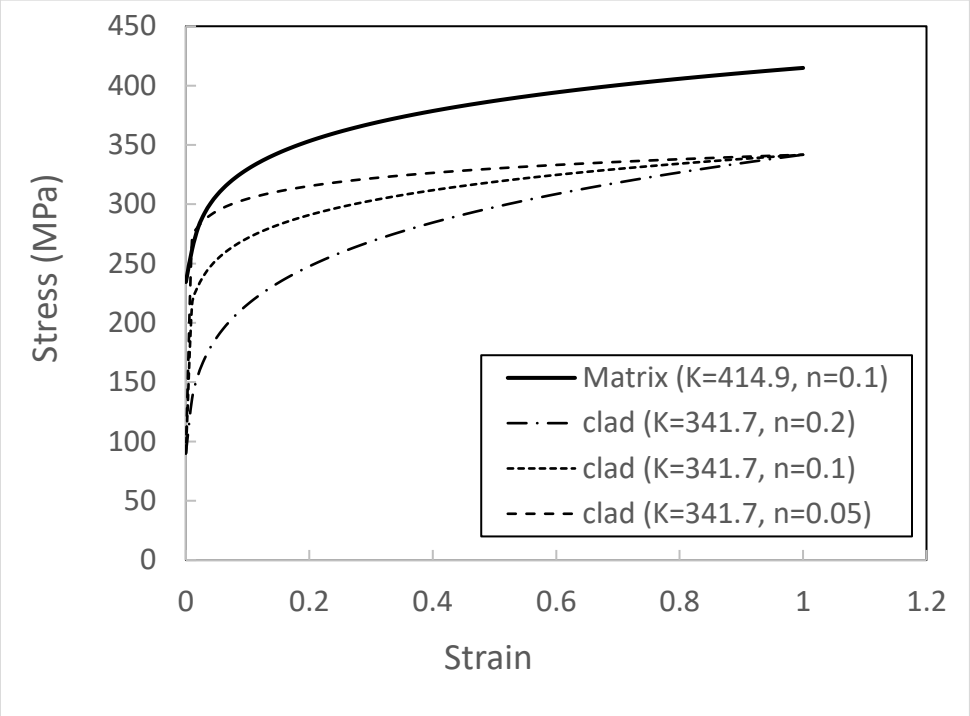

(b) "*n*" sensitivity

Figure 5. 13. Stress-strain curves for the matrix and cladding materials with various values of (a) "*K*" and (b) "*n*"

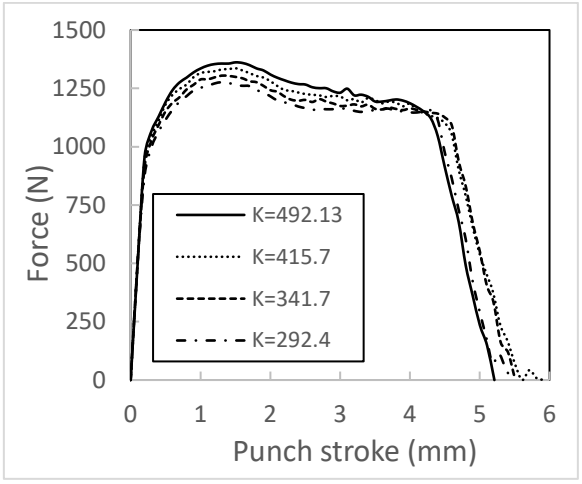

(a) "*K*" sensitivity, $\Gamma = 0.1$

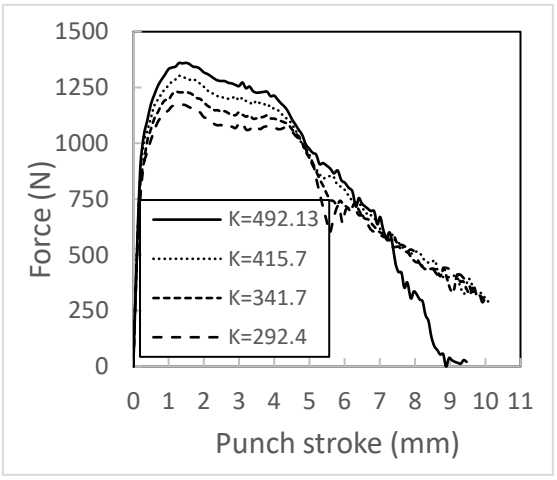

(b) "*K*" sensitivity, $\Gamma = 0.2$

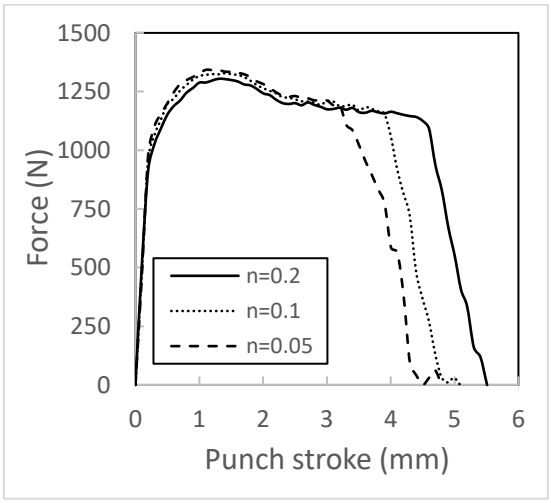

(c) "*n*" sensitivity, $\Gamma = 0.1$

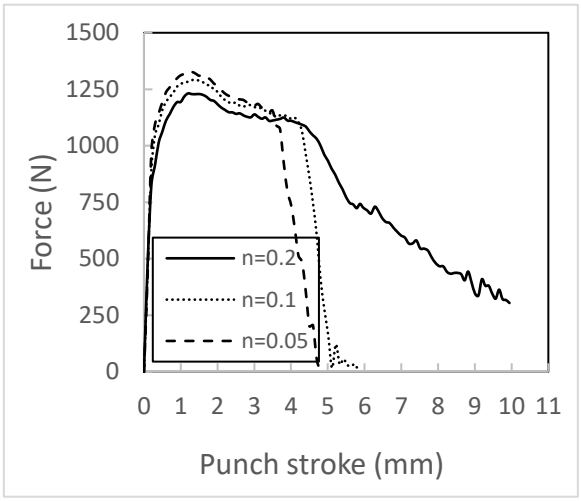

(d) "*n*" sensitivity, $\Gamma = 0.2$

Figure 5. 14. Effects of "*K*" and "*n*" on force-displacement curves ($\frac{L_m}{2} = 5.5\ mm$)

Bending fracture strains for various values of "*K*" and "*n*" are calculated and presented in Figure 5.15. "*K*" has a less significant effect on bending fracture strain (Figure 5.15[a]), but the parameter "*n*" has a significant effect on bending fracture stain (Figure 5.15[b]). Note that no fracture occurs for case $\Gamma = 0.2$ when $n = 0.2$.

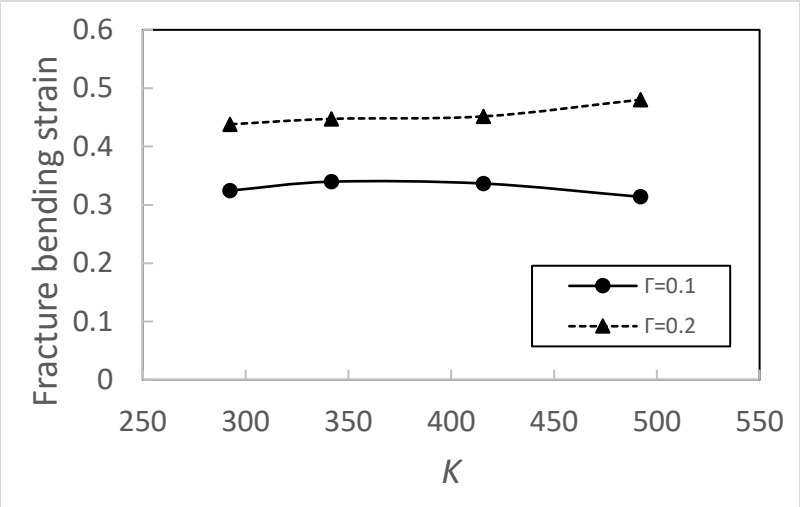

(a) "*K*" sensitivity

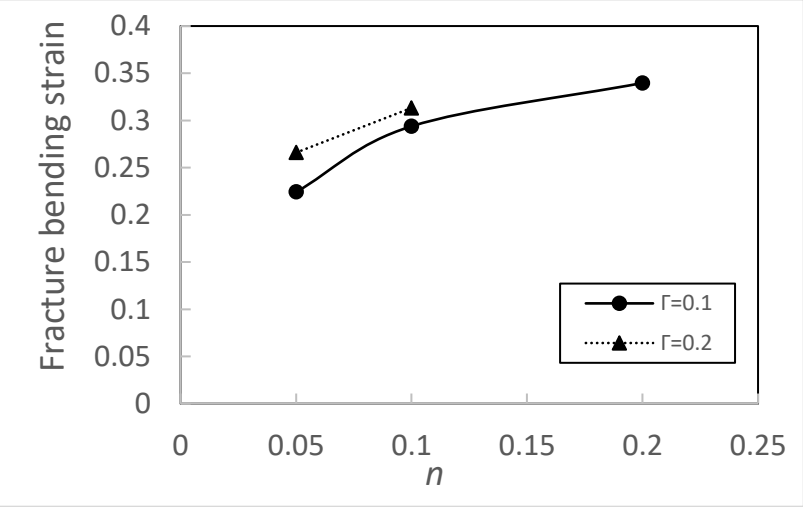

(b) "*n*" sensitivity

Figure 5. 15. Effects of (a) "*K*" and (b) "*n*" on fracture bending strain ($\frac{L_m}{2} = 5.5\ mm$)

5.5. Discussion

The present modeling results quantitatively establish the evolution of plasticity and fracture in the bending of a clad sheet sample. Previous experimental and theoretical work

has established the strain gradients developed in bending and demonstrated that failure is fracture controlled [36, 37]. When a clad layer is placed on the outer bend surface of a sheet, several factors come in to play:

1. The clad surface has the highest strain but since the clad surface is more ductile, its bending fracture strain is larger than that of the underlying, lower ductility core.
2. As the cladding thickness increases, the strain developed in the core is decreased for any bending deformation.
3. The development of hydrostatic and triaxial stresses in the core, which is the most susceptible region for failure, is modified. The effects are particularly apparent in the latter period of bending as fracture develops.

The present results quantitatively demonstrate the increase in bendability with the increasing clad thickness (Figure 5.7). At low clad thickness, the strain in the cladding exceeds the fracture strain in the core and damage is initiated in the core close to the clad-core interface, where the strain in the core is highest and the core is especially softer and less ductile than the clad material. As the clad thickness increases as a result of the strain gradients in the sheet, the strain in the core decrease, as does the damage in the core. Meanwhile, larger strains develop in the cladding due to its higher ductility. Eventually, however, the cladding thins and fails. At higher clad thickness, the strain developed in the core is insufficient to cause clad failure and the sample does not fail. The amount of generated strain in the bent specimen increases with the decrease of L_m. This matter explains why the fracture initiation transition zone happens with lower values of Γ with the decrease of L_m.

As the strain in the core decreases, the hydrostatic and triaxial stresses are modified, thereby reflecting the evolution of the damage with bending strains (Figure 5.11). As the failure transitions from the core to cladding with increasing clad thickness, the hydrostatic and triaxial components increase in the cladding, reflecting the higher strain regions.

Modifying the plastic response of the cladding affects bendability. Increasing the work hardening rate of the cladding, as reflected in an increase in "*n*" in the Power Law formulation, will result in an increase in the fracture strain and a consequent increase in bendability.

The present modeling results are consistent with strain gradient development under bending and the notion that bending is controlled by factors that influence fracture.

5.6. Conclusion

The present results show that at low cladding thicknesses, the damage is initiated in the core, but the resulting crack is blunted by the cladding. Additional bending is required until the cladding thins and fails under bending surface strain. At thicker levels of cladding, the strain in the core and the level of core damage decrease. Thus, a higher level of strain is required in the cladding to produce failure. At large cladding thickness, the bending strain in the core is insufficient to produce damage in either the core or the cladding and specimen failure does not occur. Factors that influence the plasticity and fracture of cladding affects

the bendability of the sheet. Hence, the choice of cladding has an important effect on sheet bendability.

Declaration of Competing Interest

The authors declare that they have no known competing financial interests or personal relationships that could have appeared to influence the work reported in this paper.

REFERENCES

1. X. Chen, Numerical Simulation of Effects of Cladding and Superimposed Hydrostatic Pressure on Fracture in Metals Under Tension, *Master Thesis, McMaster Univer*sity, 2009.

2. D.R. Lesuer, C.K. Syn, O.D. Sherby, J. Wadsworth, J.J. Lewandowski, W.H. Hunt, Mechanical behaviour of laminated metal composites, *Int. Mater. Rev*. 41 (5) (1996) 169–197.

3. M. Manoharan, L. Ellis, J. Lewandowski, Laminated Composites With Improved Toughness, *Technical Report, Case Western Reserve Univ., Cleveland, OH (USA)*, 1990.

4. R. Ritchie, Mechanisms of fatigue crack propagation in metals, ceramics and composites: role of crack tip shielding, *Mater. Sci. Eng. A* 103 (1) (1988) 15–28.

5. D.W. Kum, T. Oyama, J. Wadsworth, O.D. Sherby, The impact properties of laminated composites containing ultrahigh carbon (UHC) steels, *J. Mech. Phys. Solids* 31 (2) (1983) 173–186.

6. K.J. Kim, D. Kim, S.H. Choi, K. Chung, K.S. Shin, F. Barlat, K.H. Oh, J.R. Youn, Formability of AA5182/polypropylene/AA5182 sandwich sheets, *J. Mater. Process. Technol*. 139 (1–3) (2003) 1–7.

7. R.B. Wagstaff, D.J. Lloyd, T.F. Bischoff, Direct Chill Casting of CLAD Ingot, *Materials Science Forum, Trans Tech Publ*., 2006.

8. T. Li, Z. Suo, Deformability of thin metal films on elastomer substrates, *Int. J. Solids Struct*. 43 (7–8) (2006) 2351–2363.

9. Z. Xue, J.W. Hutchinson, Neck retardation and enhanced energy absorption in metal–elastomer bilayers, *Mech. Mater*. 39 (5) (2007) 473–487.

10. O. Bouaziz, Y. Brechet, J.D. Embury, Heterogeneous and architectured materials: a possible strategy for design of structural materials, *Adv. Eng. Mater*. 10 (1-2) (2008) 24–36.

11. J. Galos, A.S. Best, A.P. Mouritz, Multifunctional sandwich composites containing embedded lithium-ion polymer batteries under bending loads, *Mater. Des*. 185 (2020) 108228.

12. M. Harhash, R.R. Gilbert, S. Hartmann, H. Palkowski, Experimental characterization, analytical and numerical investigations of metal/polymer/metal sandwich composites–part 2: free bending, *J. Compos. Struct*. 232 (2020) 111421.

13. A.B. De Morais, A thick bondline beam model for the adhesively bonded 3-point bending specimen, *Int. J. Adhes. Adhes*. 96 (2020) 102465.

14. Z. Huang, X. Zhang, C. Yang, Experimental and numerical studies on the bending collapse of multi-cell Aluminum/CFRP hybrid tubes, *J. Compos. Part B: Eng.* 181 (2020) 107527.

15. S. Koch, C. Hopmann, Analysis and modelling of the media influence on short fibre reinforced amorphous thermoplastics, *J. Polym. Res*. 27 (2020) 15.

16. Y.K. Kim, H. Pouraliakbar, S.I. Hong, Effect of interfacial intermetallic compounds evolution on the mechanical response and fracture of layered Ti/Cu/Ti clad materials, *Mater. Sci. Eng. A* 772 (2020) 138802.

17. Z. Zhao, N.H. Tariq, J. Tang, C. Jia, X. Qiu, Y. Ren, H. Liu, Y. Shen, H. Du, X. Cui, J. Wang, T. Xiong, Microstructural evolutions and mechanical characteristics of Ti/steelclad plates fabricated through cold spray additive manufacturing followed by hot-rolling and annealing, *Mater. Des*. 185 (2020) 1082492.

18. G. Zhang, X. Yang, D. Zhu, L. Zhang, Cladding thick Al plate onto strong steel substrate using a novelprocess of multilayer-friction stir brazing (ML-FSB), *Mater. Des*. 185 (2020) 1082322.

19. S.T. Hong, K.S. Weil, Niobium-clad 304L stainless steel PEMFC bipolar plate material: tensile and bend properties, *J. Power Sources* 168 (2) (2007) 408–417.

20. Z. Dhiba, N. Guermazia, A. Ktaria, M. Gasperinic, N. Haddar, Mechanical bonding properties and interfacial morphologies of austenitic stainless steel clad plates, *Mater. Sci. Eng. A* 696 (2017) 374–386.

21. D.J. Lloyd, M. Gallerneault, R.B. Wagstaff, The deformation of clad aluminum sheet produced by direct chill casting, Metall. *Mater. Trans. A* 41 (8) (2010) 2093–2103.

22. X. Chen, P.D. Wu, D.J. Lloyd, Effect of superimposed hydrostatic pressure on bendability of sheet metals, *AIP Conference Proceedings, AIP*, 2010.

23. A.S. Kao, H.A. Kuhn, W.A. Spitzig, O. Richmond, Influence of superimposed hydrostatic pressure on bending fracture and formability of a low carbon steel containing globular sulfides, *J. Eng. Mater. Technol*. 112 (1) (1990) 26–30.

24. A.S. Kao, H.A. Kuhn, O. Richmond, W.A. Spitzig, Workability of 1045 spheroidized steel under superimposed hydrostatic pressure, *Metall. Trans. A* 20 (9) (1989) 1735–1741.

25. X.X. Chen, P.D. Wu, J.D. Embury, Y. Huang, Enhanced ductility in round tensile bars produced by cladding a ductile ring, Model. *Simul. Mat. Sci. Eng*. 18 (2) (2010) 25005.

26. X.X. Chen, P.D. Wu, D.J. Lloyd, J.D. Embury, Y. Huang, Enhanced ductility in sheet metals produced by cladding a ductile layer, *J. Appl. Mech.* 77 (4) (2010) 41015.

27. X.H. Hu, P.D. Wu, D.J. Lloyd, J.D. Embury, Enhanced formability in sheet metals produced by cladding a high strain-rate sensitive layer, *J. Appl. Mech*. 81 (2) (2014) 21007.

28. ABAQUS Inc., A.M.V.-., 2014.

29. V. Tvergaard, A. Needleman, Analysis of the cup-cone fracture in a round tensile bar, *Acta Metall*. 32 (1) (1984) 157–169.

30. V. Tvergaard, Influence of voids on shear band instabilities under plane strain conditions, *Int. J. Fract*. 17 (4) (1981) 389–407.

31. V. Tvergaard, On localization in ductile materials containing spherical voids, *Int. J. Fract*. 18 (4) (1982) 237–252.

32. A.L. Gurson, Continuum theory of ductile rupture by void nucleation and growth: part I—yield criteria and flow rules for porous ductile media, *J. Eng. Mater. Technol*. 99 (1) (1977) 2–15.

33. C. Chu, A. Needleman, Void nucleation effects in biaxially stretched sheets, *J. Eng. Mater. Technol*. 102 (3) (1980) 249–256.

34. V. Tvergaard, A. Needleman, Analysis of the cup-cone fracture in a round tensile bar, *J. Acta Metal*. 32 (1) (1984) 157–169.

35. Z.S. Racz, L.M. Vas, Relationship between the flexural properties and specimen aspect ratio in unidirectional composites, *Compos. Interfaces* 12 (3–4) (2005) 325–339.

36. D.J. Lloyd, Aspects of Plasticity and Fracture Under Bending in Al Alloys 16 ICAA, 2018 ISBN 978-1-926872-41-4, *plenary paper* 500006.

37. J. Datsko, C.T. Yang, Correlation of bendability of materials with their tensile properties, *J. Eng. Mater*. 82 (1960) 309–314.

CHAPTER 6

Conclusions and Recommendations for Future Work

6.1. Conclusions

The GTN model is extended to be suitable for anisotropic metals to present their elastic–plastic response in FEAs. The effects of void growth and microvoid coalescence, which lead to final ductile fracture, are considered in the model. GTN is first analyzed for understanding, and various elements and void shapes are considered. Its application is then investigated to enhance the ductility of metals under bending by superimposing hydrostatic pressure and cladding the sheet metals with a soft material.

First, the GTN model is extended on the basis of Hill's quadratic anisotropic criterion for the simulation of the plastic and damage responses of anisotropic sheet metals. The FE software ABAQUS is used, and the model is implemented in the user material subroutine with a linearized tangent moduli formulation. The ductile damage parameters are calibrated by the model's ability to reproduce the experimental results for simulating the tensile test for a typical Al alloy. Hill's quadratic anisotropy case predicts a substantial damage evolution compared with that obtained with the isotropic GTN model. Thus, high

values for the damage-free stress–strain curve in the matrix should be considered to reproduce the experimental results. Such consideration, however, is unrealistic. Consequently, Hill's anisotropic coefficients are proposed to be replaced with an effective anisotropic coefficient to reduce the damage growth. The effects of individual Hill's constants are eliminated, but the damage growth was inhibited when the equivalent stress in the anisotropic model is unchanged. For this model implementation, algorithms considering ellipsoidal voids are presented. Void volume fraction reaches a critical value in ellipsoidal voids earlier than in spherical voids. As a result, necking occurs earlier in the material in ellipsoidal voids. An algorithm for plane stress elements is implemented, and the results show that the uniaxial stress–strain responses for 3D and plane stress elements are nearly identical.

Second, the effect of superimposed hydrostatic pressure on the ductility of sheet metals under a plane strain three-point bending test is evaluated via FEM. Superimposed hydrostatic pressure delays or completely eliminates void growth and coalescence and leads to high ductility in sheet metals. Fracture strain increases with rising superimposed hydrostatic pressure. The ductility of sheet metals is higher under bending than under tension for various superimposed hydrostatic pressures. The ductile fracture parametric study in the GTN model shows that ductility increases with increasing ε_N, S_N, and f_c, decreases with increasing f_N, and is unchanged with a variation in f_f.

Third, FEA of a plane strain three-point bending test for clad sheet metals with various Γ is performed. Cladding significantly increases bendability because it slows down the

development of stress triaxiality. Fracture initiation location changes from the core material to the clad material with increasing Γ. The effect of the span length of mandrel on bendability is studied. The transition zone in failure initiation, where fracture occurs at the core and clad materials, is determined at lower values of Γ with an increase in span length. Finally, bendability increases with an increase in hardening exponent in the clad material. The change in bendability is insignificant if the stress–strain curve in the clad material varies but the hardening exponent is constant.

In sum, the GTN model is analyzed, implemented in ABAQUS and extended to be suitable for anisotropic metals. Hill's constants should be replaced with an effective anisotropic coefficient to eliminate the substantial generated damage. The ductility of sheet metals is increased with hydrostatic pressure because it delays void growth and coalescence. The bendability increases by cladding a sheet metal when the development of stress triaxiality slows down in soft materials.

6.2. Recommendations for future work

The implementation of the GTN model suitable for anisotropic metals is presented in this study and the application of the isotropic GTN model to enhance the ductility of metals by superimposing hydrostatic pressure and cladding sheet metals are investigated. The recommendations for future work can be summarized as follows:

[1]. Implementation of the GTN model and considering the strain rate sensitivity of matrix materials.

[2]. Numerical study on the effect of pre-strain on the bendability of sheet metals using the GTN model.

[3]. Numerical study on the effect of width/thickness ratio on bendability using the GTN model.

[4]. Numerical study on the effect of superimposed hydrostatic pressure on the ductility of metal rings under compression.

7. REFERENCES

[1]. Ashby, M.F., Embury, J.D., Cooksley, S.H., Teirlinck, D., Fracture maps with pressure as a variable. *Scripta Metallurgica*, 1985. 19(4): p. 385-390.

[2]. Gatea, S., Ou, H., Lu, B., McCartney. G., Modelling of ductile fracture in single point incremental forming using a modified GTN model. *Engineering Fracture Mechanics*, 2017. 186: p. 59-79.

[3]. Wu, P.D., et al., Evaluation of anisotropic yield functions for aluminum sheets, *International Journal of Plasticity*, 2003. 19(1): p. 121-138.

[4]. Hill, R., A theory of the yielding and plastic flow of anisotropic metals. *in Proceedings of the Royal Society of London A: Mathematical, Physical and Engineering Sciences*. 1948. The Royal Society.

[5]. Liao, K.C., Pan, J., and Tang, S., Approximate yield criteria for anisotropic porous ductile sheet metals. *Mechanics of Materials*, 1997. 26(4): p. 213-226.

[6]. Hosford, W., A generalized isotropic yield criterion. *Journal of Applied Mechanics*, 1972. 39(2): p. 607-609.

[7]. Barlat, F., Lian, K., Plastic behavior and stretchability of sheet metals. Part I: A yield function for orthotropic sheets under plane stress conditions. *International Journal of Plasticity*, 1989. 5(1): p. 51-66.

[8]. Ragab, A.R.A., Bayoumi, S.E.A., Engineering solid mechanics: fundamentals and applications. 1998: *CRC Press*.

[9]. Kim, Y., Won, S., Kim, D., Son, H., Approximate yield criterion for voided anisotropic ductile materials. *KSME International Journal*, 2001. 15(10): p. 1349-1355.

[10]. Kim, Y.S., Won, S.W., Na, K.H., Effect of material damage on forming limits of voided anisotropic sheet metals. *Metallurgical and Materials Transactions A*, 2003. 34(6): p. 1283-1290.

[11]. Kim, Y.S., Son, H.S., Yang, S.H., Lee, S.R., Prediction of forming limits for voided anisotropic sheets using strain gradient dependent yield criterion. in *Key Engineering Materials*. 2003. Trans Tech Publ.

[12]. Lloyd, D.J., Gallerneault, M., Wagstaff, R.B., The deformation of clad aluminum sheet produced by direct chill casting. *Journal of Metallurgical and Materials Transactions A*, 2010. 41(8): p. 2093-2103.

[13]. Shi, Y., Zhao, P.Z., Jin, H., Wu, P.D., Lloyd, D.J., Analysis of surface roughening in AA6111 automotive sheet under pure bending. *Journal of Metallurgical and Materials Transactions A*, 2016. 47(2): p. 949-960.

[14]. Lloyd, D.J., Evans, E., Pelow, C., Nolan, P., Bending in aluminium alloys AA 6111 and AA 5754 using the cantilever bend test. *Materials Science Technology*, 2002. 18(6): p. 621-628.

[15]. Sarkar, J., Kutty, T.R.G., Conlon, K.T., Wilkinson, D.S., Embury, J.D., Lloyd, D.J., Tensile and bending properties of AA5754 aluminum alloys. *Materials Science Engineering: A*, 2001. 316(1-2): p. 52-59.

[16]. Sarkar, J., Kutty, K.T., Wilkinson, D.S., Embury, J.D., Lloyd, D.J., Tensile properties and bendability of T4 treated AA6111 aluminum alloys. *Materials Science Engineering: A*, 2004. 369(1-2): p. 258-266.

[17]. Racz, Z.S., Vas, L.M., Relationship between the flexural properties and specimen aspect ratio in unidirectional composites, *Composite Interfaces*, 2005. 12(3-4): p. 325-339.

[18]. Ragab, A., Saleh, C.A., A, Evaluation of bendability of sheet metals using void coalescence models, *Materials Science Engineering: A*, 2005. 395(1-2): p. 102-109.

[19]. Feister, T., Kim, H., Gwinn, A., Schiller, T., Austin, M., Failure predictions in warm forming of 7075-T6 aluminum structural parts. *in IOP Conference Series: Materials Science and Engineering*. 2018. IOP Publishing.

[20]. Elsharkawy, A.A., El-Domiaty, A.A., Determination of stretch-bendability limits and springback for T-section beams, *Journal of Materials Processing Technology*, 2001. 110(3): p. 265-276.

[21]. Leu, D.K., A simplified approach for evaluating bendability and springback in plastic bending of anisotropic sheet metals, *Journal of Materials Processing Technology*, 1997. 66(1-3): p. 9-17.

[22]. Mattei, L., Daniel, D., Guilionda, G., Klocker, H., Driver, J., Strain localization and damage mechanisms during bending of AA6016 sheet, *Materials Science Engineering: A*, 2013. 559: p. 812-821.

[23]. Davidkov, A. et al., Strain localization and damage development during bending of Al–Mg alloy sheets, *Materials Science Engineering: A*, 2012. 550: p. 395-407.

[24]. Hou, P., Zhao, H., Ma, Z., Zhang, S., Li, J., Dong, X., Sun, Y., Zhu, Z., Influence of punch radius on elastic modulus of three-point bending tests. *Journal of Advances in Mechanical Engineering*, 2016. 8(5): p. 1-8.

[25]. Datsko, J., Yang, C.T., Correlation of bendability of materials with their tensile properties. *Journal of Engineering for Industry*, 1960. 82(4): p. 309-313.

[26]. Kim, J., Ryou, H., Kim, D., Kim, D., Lee, W., Hong, S.H., Chung, K., Constitutive law for AZ31B Mg alloy sheets and finite element simulation for three-point bending, *International Journal of Mechanical Sciences*, 2008. 50(10-11): p. 1510-1518.

[27]. Mehrotra, P., Lillo, T., Agnew, S., Ductility enhancement of a heat-treatable magnesium alloy. *Scripta Materialia*, 2006. 55(10): p. 855-858.

[28]. Ishida, K., Kainuma, R., Nishizawa, T., Ductility enhancement in NiAl (B2)-base alloys by microstructural control. *Metallurgical Transactions A*, 1991. 22(2): p. 441-446.

[29]. Chino, Y., Kado, M., Mabuchi, M., Enhancement of tensile ductility and stretch formability of magnesium by addition of 0.2 wt%(0.035 at%) Ce. *Materials Science and Engineering: A*, 2008. 494(1-2): p. 343-349.

[30]. Ghasemi-Nanesa, H., Nili-Ahmadabadi, M., Shirazi, H., Hossein Nedjad, S., Pishbin, S.H., Ductility enhancement in ultrafine-grained Fe–Ni–Mn martensitic steel by stress-induced reverse transformation. *Materials Science and Engineering: A*, 2010. 527(29-30): p. 7552-7556.

[31]. Kao, A.S, Kuhn, H.A., Richmond, O. Spitzig, W.A., Workability of 1045 spheroidized steel under superimposed hydrostatic pressure, *Metallurgical Transactions A*, 1989. 20(9): p. 1735-1741.

[32]. French, I., Weinrich, P.F., Weaver, C.W., Tensile fracture of free machining brass as a function of hydrostatic pressure, *Acta Mettallurgica*, 1973. 21(8): p. 1045-1049.

[33]. Brownrigg, A., Spitzig, W.A., Richmond, O., Teirlinck, D., Embury, J.D., The influence of hydrostatic pressure on the flow stress and ductility of a spherodized 1045 steel, *Acta Mettallurgica*, 1983. 31(8): p. 1141-1150.

[34]. Korbel, A., Raghunathan, V.S., Teirlinck, D., Spitzig, W., Richmond. O., Embury, J.D., A structural study of the influence of pressure on shear band formation, *Acta Mettallurgica*, 1984. 32(4): p. 511-519.

[35]. French, I.E., Weinrich, P.F., The influence of hydrostatic pressure on the tensile deformation and fracture of copper, *Metallurgical Transactions A*, 1975. 6(4): p. 785.

[36]. Kim, K.J., Kim, D., Choi, S.H., Chung, K., Shin, K.S., Barlat, F., Oh, K.H., Youn, J.R., Formability of AA5182/polypropylene/AA5182 sandwich sheets. *Journal of Materials Processing Technology*, 2003. 139(1-3): p. 1-7.

[37]. Wagstaff, R.B., Lloyd, D.J., Bischoff, T.F., Direct chill casting of CLAD ingot. *in Materials Science Forum*. 2006. *Trans Tech Publ*.

[38]. Li, T., Suo, Z., Deformability of thin metal films on elastomer substrates. *International Journal of Solids and Structures*, 2006. 43(7-8): p. 2351-2363.

[39]. Xue, Z., Hutchinson, J.W., Neck retardation and enhanced energy absorption in metal–elastomer bilayers. *Mechanics of Materials*, 2007. 39(5): p. 473-487.

[40]. Kao, A., Kuhn, H.A., Richmond, O., Spitzig, W.A., Tensile fracture and fractographic analysis of 1045 spheroidized steel under hydrostatic pressure. *Journal of Materials Research*, 1990. 5(1): p. 83-91.

[41]. Kao, A., Kuhn, H.A., Spitzig, W.A., Richmond, O., Influence of superimposed hydrostatic pressure on bending fracture and formability of a low carbon steel containing globular sulfides. *Journal of Engineering Materials and Technology*, 1990. 112(1): p. 26-30.

[42]. Sauer, J.A., Mears, D.R., Pae, K.D., Effects of hydrostatic pressure on the mechanical behaviour of polytetrafluoroethylene and polycarbonate, *European Polymer Journal*, 1970. 6(7): p. 1015-1032.

[43]. Chen, X.X, Numerical simulation of effects of cladding and superimposed hydrostatic pressure on fracture in metals under tension, *MSc thesis, McMaster University*, 2009.

[44]. Dhib, Z., Guermazi, N., Katri, A., Gasperini, M., Haddar, N., Mechanical bonding properties and interfacial morphologies of austenitic stainless steel clad plates, *Materials Science and Engineering: A*, 2017. 696: p. 374-386.

[45]. Lesuer, D., Syn, C.K., Sherby, O.D., Wadsworth, J., Lewandowski, J.J., Hunt, W.H., Mechanical behaviour of laminated metal composites. *International Materials Reviews*, 1996. 41(5): p. 169-197.

[46]. Manoharan, M., Ellis, L., Lewandowski, J.J., Laminated composites with improved toughness. 1990, *Case Western Reserve Univ., Cleveland, OH (USA).*

[47]. Ritchie, R., Mechanisms of fatigue crack propagation in metals, ceramics and composites: role of crack tip shielding. *Materials Science and Engineering: A*, 1988. 103(1): p. 15-28.

[48]. Kum, D.W., Oyama, T., Wadsworth, J., Sherby, O.D., The impact properties of laminated composites containing ultrahigh carbon (UHC) steels. *Journal of the Mechanics and Physics of Solids*, 1983. 31(2): p. 173-186.

[49]. Bouaziz, O., Brechet, Y., Embury, J.D., Heterogeneous and architectured materials: a possible strategy for design of structural materials. *Advanced Engineering Materials*, 2008. 10(1-2): p. 24-36.

[50]. Reddy, J., An introduction to the finite element method. Vol. 1221. 2004: *McGraw-Hill New York.*

[51]. Hearn, E.J., Introduction to finite element method. *Mechanics of Materials* 1997. 2 (Third Edition). Elsevier Ltd 300-380.

[52]. Cook, R.D., Sons, J.W., Finite element modeling for stress analysis. 1995.

[53]. Cha, W., Kim, N., Quantification of micro-cracks on the bending surface of roll formed products using the GTN model, *Metals and Materials International*, 2014. 20(5): p. 841-850.

[54]. Liu, Z., Li, L., Jie, Y., Li, S., Wang, Z., Guan, W., Influence of heat treatment conditions on bending characteristics of 6063 aluminum alloy sheets, *Transactions of Nonferrous Metals Society of China*, 2017. 27(7): p. 1498-1506.

[55]. Soyarslan, C., Gharbi, M.M., Tekkaya, A.E., A combined experimental–numerical investigation of ductile fracture in bending of a class of ferritic–martensitic steel, *International Journal of Solids and Structures*, 2012. 49(13): p. 1608-1626.

[56]. Kim, J.H., Sung, J,H., Matlock, D.K., Kim, D., Wangoner, R.H., Finite element and analytical study of plane strain draw-bend failure of advanced high strength steels, *International Journal of Material Forming*, 2010. 3(1): p. 187-190.

[57]. Jin, L., Dong, J., Sun, J., Luo, A.A., In-situ investigation on the microstructure evolution and plasticity of two magnesium alloys during three-point bending, *International Journal of Plasticity*, 2015. 72: p. 218-232.

[58]. Tagarielli, V., Fleck, N., Deshpande, V.S., The collapse response of sandwich beams with aluminium face sheets and a metal foam core, *Advanced Engineering Materials*, 2004. 6(6): p. 440-443.

[59]. Le Maoût, N., Thuillier, S., Manach, P.Y., Aluminum alloy damage evolution for different strain paths–Application to hemming process, *Engineering Fracture Mechanics*, 2009. 76(9): p. 1202-1214.

[60]. Kami, A., Mollaei Dariani, B., Sadough Vanini, A., Cosma, D.S., Banabic, D., Numerical determination of the forming limit curves of anisotropic sheet metals using GTN damage model, *Journal of Materials Processing Technology*, 2015. 216: p. 472-483.

[61]. Chen, Z., Dong, X., The GTN damage model based on Hill'48 anisotropic yield criterion and its application in sheet metal forming, *Computational Materials Science*, 2009. 44(3): p. 1013-1021.

[62]. Aravas, N., On the numerical integration of a class of pressure-dependent plasticity models, *International Journal for Numerical Methods in Engineering*, 1987. 24(7): p. 1395-1416.

[63]. Gurson, A.L., Continuum theory of ductile rupture by void nucleation and growth: Part I—Yield criteria and flow rules for porous ductile media, *Journal of Engineering Materials and Technology*, 1977, 99(1): p. 2-15.

[64]. Marciniak, Z., Kuczyński, Z., Limit strains in the processes of stretch-forming sheet metal. *International Journal of Mechanical Sciences*, 1967. 9(9): p. 609IN1613-612IN2620.

[65]. Son, H.S., Kim, Y.S., Prediction of forming limits for anisotropic sheets containing prolate ellipsoidal voids. *International Journal of Mechanical Sciences*, 2003. 45(10): p. 1625-1643.

[66]. Tvergaard, V., On localization in ductile materials containing spherical voids, *International Journal of Fractu*re, 1982. 18(4): p. 237-252.

[67]. Tvergaard, V., Needleman, A., Analysis of the cup-cone fracture in a round tensile bar, *Acta Metallurgica*, 1984. 32(1): p. 157-169.

[68]. Chu, C., Needleman, A., Void nucleation effects in biaxially stretched sheets, *Journal of Engineering Materials and Technology*, 1980, 102(3): p. 249-256.

[69]. Needleman, A., Tvergaard, V., An analysis of ductile rupture in notched bars, *Journal of the Mechanics and Physics of Solids*, 1984. 32(6): p. 461-490.

[70]. Brunet, M., Mguil, S., Morestin, F., Analytical and experimental studies of necking in sheet metal forming processes. *Journal of Materials Processing Technology*, 1998. 80: p. 40-46.

[71]. Jin, C., Niu, J., Fu, C., Modeling thermal cycling induced micro-damage in aluminum welds: An extension of Gurson void nucleation model. *Computational Materials Science*, 2008. 43(4): p. 1165-1171.

[72]. Abbasi, M., Ketabchi, M., Izadkhah, H., Fatmehsaria, D.H., Aghbash, A.N., Identification of GTN model parameters by application of response surface methodology. *Procedia Engineering*, 2011. 10: p. 415-420.

[73]. Shen, Y., Garnier, J., Allais, L., Crepin, J., Ancelet, O., Hiver, J.M., Experimental and numerical characterization of anisotropic damage evolution of forged Al6061-T6 alloy. *Procedia Engineering*, 2011. 10: p. 3429-3434.

[74]. Achouri, M., Germain, G., Santo, P.D., Saidane, D., Implementation and validation of a Gurson damage model modified for shear loading: effect of void growth rate and mesh size on the predicted behavior. *in Key Engineering Materials*. 2012. *Trans Tech Publ*.

[75]. Ramazani, A., Abbasi, M., Prahl, U., Bleck, W., Failure analysis of DP600 steel during the cross-die test. *Computational Materials Science*, 2012. 64: p. 101-105.

[76]. Kami, A., Dariani, B.M., Sadough Vanini, S.A., Banabic, D., Application of a GTN damage model to predict the fracture of metallic sheets subjected to deep-drawing. *Proceeding of the Romanian Academy, Series A*, 2014. 15: p. 300-309.

[77]. Simha, C.H.M., Xu, S., Tyson, W.R., Computational modeling of the drop-weight tear test: A comparison of two failure modeling approaches. *Engineering Fracture Mechanics*, 2015. 148: p. 304-323.

[78]. Lim, Y., An, T., Ko, S., Kim, N., Formability of coated vinyl on sheet metal during deep drawing process. *Journal of Materials Processing Technology*, 2016. 227: p. 178-189.

[79]. Soyarslan, C., Gulcimen, B., Bargmann, S., Hahner, P., Modeling of fracture in small punch tests for small-and large-scale yielding conditions at various temperatures. *International Journal of Mechanical Sciences*, 2016. 106: p. 266-285.

[80]. Ayatollahi, M., Darabi, A.C., Chamani, H.R., Kadkhodapour, J., 3D Micromechanical Modeling of Failure and Damage Evolution in Dual Phase Steel Based on a Real 2D Microstructure. *Acta Mechanica Solida Sinica*, 2016. 29(1): p. 95-110.

[81]. Zaman, T.N., Effects of Strain Path Changes on Damage Evolution and Sheet Metal Formability, *MSc thesis, McMaster University*, 2008.

[82]. Monchiet, V., Cazacu, O., Charkaluk, E., Kondo, D., Macroscopic yield criteria for plastic anisotropic materials containing spheroidal voids. *International Journal of Plasticity*, 2008. 24(7): p. 1158-1189.

[83]. Pastor, F., J. Pastor, Kondo, D., Limit analysis of hollow spheres or spheroids with Hill orthotropic matrix. *Comptes Rendus Mécanique*, 2012. 340(3): p. 120-129.

[84]. Morin, L., Madou, K., Leblond, J.B., Kondo, D., A new technique for finite element limit-analysis of Hill materials, with an application to the assessment of criteria for anisotropic plastic porous solids. *International Journal of Engineering Science*, 2014. 74: p. 65-79.

[85]. Morin, L., Leblond, J.B., Kondo, D., A Gurson-type criterion for plastically anisotropic solids containing arbitrary ellipsoidal voids. *International Journal of Solids and Structures*, 2015. 77: p. 86-101.

[86]. Paux, J., Morin, L., Brenner, R., Kondo, D., An approximate yield criterion for porous single crystals. *European Journal of Mechanics-A/Solids*, 2015. 51: p. 1-10.

[87]. Keralavarma, S., Chockalingam, S., A criterion for void coalescence in anisotropic ductile materials. *International Journal of Plasticity*, 2016. 82: p. 159-176.

[88]. Weinrich, P., French, I., The influence of hydrostatic pressure on the fracture mechanisms of sheet tensile specimens of copper and brass. *Journal of Acta Metallurgica*, 1976. 24(4): p. 317-322.

[89]. Spitzig, W.A., Richmond, O., The effect of pressure on the flow stress of metals, *Journal of Acta Metallurgica*, 1984. 32(3): p. 457-463.

[90]. Bao, Y., Wierzbicki, T., On the cut-off value of negative triaxiality for fracture, *Engineering Fracture Mechanics*, 2005. 72(7): p. 1049-1069.

[91]. Wu, P., Embury, J.D., Lloyd, D.J., Huang, Y., Neale, K.W., Effects of superimposed hydrostatic pressure on sheet metal formability. *International Journal of Plasticity*, 2009. 25(9): p. 1711-1725.

[92]. Gotoh, M., Chung, T., Iwata, N., Effect of out-of-plane stress on the forming limit strain of sheet metals, *Mechanics and Material Engineering*, 1995. 38(1): p. 123-132.

[93]. Peng, J., Wu, P.D., Huang, Y., Chen, X.X., Lloyd, D.J., Embury, J.D., Neale, K.W., Effects of superimposed hydrostatic pressure on fracture in round bars under tension. *International Journal of Solids Structures*, 2009. 46(20): p. 3741-3749.

[94]. Wu, P.D., Chen, X.X., Lloyd, D.J., Embury, J.D., Effects of superimposed hydrostatic pressure on fracture in sheet metals under tension. *International Journal of Mechanical Sciences*, 2010. 52(2): p. 236-244.

[95]. Chen, X.X., Wu, P.D., Lloyd, D.J., Effect of Superimposed Hydrostatic Pressure on Bendability of Sheet Metals. *in AIP Conference Proceedings*. 2010. *AIP*.

[96]. Liu, J., Wang, Z., Meng, Q., Numerical investigations on the influence of superimposed double-sided pressure on the formability of biaxially stretched AA6111-T4 sheet metal. *Journal of Materials Engineering Performance*, 2012. 21(4): p. 429-436.

[97]. Hu, X., Wu, P.D., Lloyd, D.J., Embury, L.D.,, Enhanced formability in sheet metals produced by cladding a high strain-rate sensitive layer, *Journal of Applied Mechanics*, 2014. 81(2): p. 021007.

[98]. Hutchinson, J., Neale, K., Influence of strain-rate sensitivity on necking under uniaxial tension. *Acta Metallurgica*, 1977. 25(8): p. 839-846.

[99]. Hong, S.T., Weil, K.S., Niobium-clad 304L stainless steel PEMFC bipolar plate material: Tensile and bend properties, *Journal of Power Sources*, 2007. 168(2): p. 408-417.

[100]. Chen, X.X, Wu, P.D., Embury, J.D., Huang, Y., Enhanced ductility in round tensile bars produced by cladding a ductile ring, *Modelling and Simulation in Materials Science and Engineering*, 2010. 18(2): p. 025005.

[101]. Chen, X.X, Wu, P.D., Embury, J.D., Huang, Y., Enhanced ductility in sheet metals produced by cladding a ductile layer, *Journal of Applied Mechanics*, 2010. 77(4): p. 041015.